

TWO ENABLING DEVELOPMENTS FOR COMPUTATIONAL CONTACT MECHANICS

By

Gaurav Chauda

A DISSERTATION

Submitted to
Michigan State University
in partial fulfillment of the requirements
for the degree of

Mechanical Engineering – Doctor of Philosophy

2021

ABSTRACT

TWO ENABLING DEVELOPMENTS FOR COMPUTATIONAL CONTACT MECHANICS

By

Gaurav Chauda

Two approaches for computational contact mechanics are explored to provide an accurate and robust numerical simulation of frictional contact. First, a novel quasi-static contact algorithm (Method of First Violation) is developed, which provides a solution over the load history that is admissible in the sense that all equality and inequality constraints are satisfied at each load step and every point between load steps. The central idea of this algorithm is to calculate each load increment to be exactly which is necessary to cause the first nodal inequality constraint to be violated. At the end of that load increment, the status of the associated node is switched to a different status (such as from contact to non-contact) where the inequality constraint is replaced with an equality constraint, and a new inequality constraint is introduced. Importantly, the constraints of the previous and the new node status are simultaneously satisfied at that point in the loading cycle.

The Method of First Violation (MFV) algorithm is illustrated using a compliance formulation for degrees of freedom on the surface of a half-plane loaded by a rigid indenter with friction. The compliance formulation permits considering only the degrees of freedom in the vicinity of contact, therefore extremely fine surface discretization is possible using only a modest number of degrees of freedom. Because this contact problem has been well studied using analytic techniques and because of the extremely fine mesh resolution, it is possible to perform a critical comparison with analytical solutions.

An added benefit of this algorithm is its greatly improved robustness. This indenter/half-plane discretization was also used to test MFV where friction was represented by a two-parameter (static and kinematic) model. Though such problems are notoriously ill-conditioned, the MFV remained robust. It was also used to explore a problem involving the Dahl friction model.

Second, a compliance matrix formulation is derived for a two-dimensional elastic disk and for a hole in an infinite elastic plane. The circular disk/hole surface is discretized finely with a

uniform distribution of nodes and a set of basis functions for traction are defined so that each basis function has a value of 1 in the vicinity of the corresponding node and a value of zero elsewhere. The surface displacement field associated with each traction basis function is obtained through a laborious derivation involving Fourier series and terms of the Michell's Airy stress function. The compliance matrix is constructed using the calculated displacement fields evaluated at each node. Fortunately, one may restrict attention to only the tractions and displacements in the vicinity of contact because all surface tractions outside that region are zero so the resulting compliance matrix is of tractable size. This semi-analytical formulation provides a direct construction of a compliance matrix with an extremely fine surface discretization, easy implementation of friction models, and accommodation of elastic coupling.

The Method of First Violation and the compliance formulation of two-dimensional circular bodies are implemented together to numerically simulate multiple contact problems. Five different geometries are designed using cylinders, holes, and half-plane, where two contacting bodies are pressed against each other and then sheared cyclically for four cycles. Surface tractions, stick ratios, steady-state dissipation, and error in surface tractions are calculated using Goodman decoupling and full decoupling approximations. The results are compared with calculations employing full elastic coupling to assess the qualitative and quantitative ramifications of the decoupling assumptions. The surface tractions calculated using Goodman decoupling show qualitative similarity with those of full elastic coupling but showed some severe errors in predicting the dissipation. The full decoupling approximation simulations predictions are significantly different from the predictions of full coupling calculations. However, they are no worse than the Goodman decoupling approximations in predicting dissipation.

This ability to introduce extremely fine mesh resolution in a contact region with a robust contact algorithm allows us to explore many contact characteristics through numerical simulation, which were previously intractable.

Copyright by
GAURAV CHAUDA
2021

This thesis is dedicated to my parents.

ACKNOWLEDGEMENTS

Your acknowledgements here. I express my sincere gratitude to my advisor Prof. Daniel J Segalman for mentoring me throughout my doctoral studies. Your motivation kept me working even in the gloomy days of my studies. I learned a lot from your stories and experiences. My sincere thanks to my Dissertation committee Prof. Brian Feeny, Prof. Thomas Pence, Changyong Cao, and Prof. James Barber (from University of Michigan) for guiding me during my studies. I want to thank Prof. Matt Allen (from University of Wisconsin) and his research group for providing helpful suggestions during this research. I would like to thank Prof. Matthew Brake and Prof. Christoph Schwingshackl for letting me participate in the NDCSI summer programs.

I thank my parents Kailash and Anita, my sister Damini, and brother-in-law Nitin for their support in my studies. I would like thank lab colleagues Fatemeh, Ayse, Aakash, Jun, and Jamal for making these studies fun and enjoyable. I appreciate all the help and support provided by friends Pratap, Anuj, Suhas, Dhruvajit, Anshu, HP, Vivek, Jhalak, Hannah, and Prithvi specially for the meaningful discussions and suggestions for PhD life and academic studies. I would like to thank my friends Chelsea, Paige, Andya, Marisol, Thang, and my MSU salsa club family for making my stay at MSU enjoyable.

TABLE OF CONTENTS

LIST OF TABLES	x
LIST OF FIGURES	xi
KEY TO ABBREVIATIONS	xvi
CHAPTER 1 INTRODUCTION	1
1.1 Overview	1
1.2 Motivation	1
1.3 Literature Review	4
1.3.1 Friction-Free Contact Algorithms	5
1.3.2 Contact Algorithms with Friction	7
1.3.3 Path Dependence in Contact Algorithms	8
1.4 Thesis Synopsis	9
I The Method of First Violation (Contact Algorithm)	11
CHAPTER 2 CONTACT ALGORITHMS	12
2.1 Compliance Formulation	12
2.1.1 Taxonomy of Contact Status	13
2.1.2 Compliance Matrix with Contact Constraints	14
2.2 Algorithm I	16
2.3 Algorithm II: Method of First Violation	18
2.3.1 Admissible Contact Histories	21
2.3.2 Contact Status Violations	23
2.3.2.1 Geometric Violation	23
2.3.2.2 Normal Pressure Violation	23
2.3.2.3 Violation in Stick Constraints	24
2.3.2.4 Violation in Slip Constraints	24
2.3.3 Single-Node Illustrations of Computing δL	24
CHAPTER 3 VERIFICATION OF CONTACT ALGORITHMS	28
3.1 Frictionless Normal Contact	28
3.1.1 Rigid Cylinder Pressed against an Elastic Half-plane	28
3.1.2 Rigid Flat Indenter Pressed against an Elastic Half-plane	29
3.2 Normal Contact with the Coulomb Friction	31
3.2.1 Comparison with Spence (1973) Stick Ratio Results	32
3.2.2 Verification of Numerical Lateral Traction with an Analytical Expression	35
3.2.3 Verification of Stick-Ratio in the Mindlin Problem.	35
3.3 Coulomb Friction Model in Mindlin Problem	37
3.4 Two-parameter Coulomb Friction Model in Mindlin Problem	38

3.5	High-Coefficient of Friction with Full Elastic Coupling	40
3.6	Implementation of Dahl Friction Model	41
3.7	Two-parameter Coulomb Friction for a Cylinder Pressed against an Elastic Half-plane	44
3.7.1	Cyclic Shear Loading with Two-Parameter Coulomb Friction	46
3.8	Algorithm Computational Efficiency	48
3.9	Summary of the Algorithm Verification and Comparison	49

II An Extremely Fine Mesh Strategy Using Compliance Matrices 52

CHAPTER 4	COMPLIANCE FORMULATION FOR AN ELASTIC DISK AND FOR A HOLE IN AN INFINITE ELASTIC PLANE	53
4.1	Computational Issues	53
4.2	2D-Cylinder Airy Stress Function (Michell Solution)	57
4.2.1	General Discretization Strategy	58
4.2.2	A Solid Elastic Disk	59
4.2.2.1	Creating the Surface Displacement Field in an Elastic Disk	61
4.2.3	A Hole in an Infinite Elastic Plane	64
4.2.3.1	Creating Surface Displacement Field for a Hole in an Infinite Plane	64
4.3	Creating a Compliance Matrix	66
4.4	Summary of Compliance Matrix Formulation	71
CHAPTER 5	VERIFICATION OF COMPLIANCE FORMULATION AND OTHER CONTACT PROBLEMS	72
5.1	Verification Problems	73
5.1.1	An Elastic Cylinder Pressed against a Rigid Half-plane	73
5.1.2	Rigid Cylinder Pressed inside of a Hole in an Infinite Elastic Plane	76
5.1.3	Normal Contact with Friction for an Elastic Cylinder Pressed against a Rigid Half-plane	77
5.1.4	von-Mises Stress Distribution in an Elastic Cylinder in Contact	78
5.2	Two Identical Elastic Cylinders Pressed and Sheared	80
5.2.1	Comparing Surface Traction and Displacement	81
5.2.2	Comparing Stress Distributions inside the Cylinders	83
5.3	Summary of the 2D Compliance Verification	85

III Comparison of Decoupling Approximations and their Ramifications 86

CHAPTER 6	ELASTIC DECOUPLING APPROXIMATIONS	87
6.1	Decoupling Approximations in Elastic Contact	87
6.2	Analytical Expressions	89
6.2.1	Contact Problems	90
6.3	Surface Traction for a Cyclic Lateral Force	91
6.4	Variation with Lateral Force	95
6.5	Variation with Coefficients of Friction	99

6.6	Discussion	102
6.7	Summary of Effects of Elastic Decoupling Approximations	103
CHAPTER 7 CONCLUSION AND FUTURE RESEARCH		105
7.1	Summary	105
7.2	Concluding Remarks	106
7.3	Future Research	107
APPENDICES		108
APPENDIX A	COMPLIANCE MATRIX FORMULATION FOR ELASTIC HALF-PLANE	109
APPENDIX B	IMPLEMENTAION OF DAHL FRICTION MODEL WITH ALGORITHM-II (METHOD OF FIRST VIOLATION)	114
APPENDIX C	MICHELL COEFFICIENTS FOR A SOLID ELASTIC DISK WITH NO HOLES	116
APPENDIX D	MICHELL COEFFICIENTS FOR AN INFINITE ELASTIC PLANE WITH A CIRCULAR HOLE	123
APPENDIX E	THE MICHELL SOLUTION- STRESS AND DISPLACEMENT COMPONENTS	130
BIBLIOGRAPHY		133

LIST OF TABLES

Table 2.1: Equality and inequality constraints for each node status type.	14
Table 4.1: Maximum contact arc for compressing an elastic disk onto a flat rigid surface above which the disk material exceeds its elastic limit.	55
Table 4.2: Michell coefficients for applied radial and tangential unit tractions over $\Delta\theta$ centered at $\theta = 0$ and $r = R$ on the elastic solid disk	63
Table 4.3: Michell coefficients for applied radial and tangential tractions over $\Delta\theta$ centered at $\theta = 0$ and $r = R$ for the hole in the elastic plane.	65
Table B.1: Equality and inequality constraints for Dahl friction model.	115
Table E.1: The terms of Michell Solution (Airy Stress Function) and their corresponding stresses and displacements. Terms shown in the cyan are the self-equilibrating part of the solid disk stress function, terms shown in white are the self-equilibrating part of the Hole in a elastic plane, and terms shown in gray are modified secular terms removing their multi-value through linear combinations.	131
Table E.2: The terms of Michell Solution (Airy Stress Function) and their corresponding stresses and displacements. Terms shown in the cyan are the self-equilibrating part of the solid disk stress function and terms shown in white are the self-equilibrating part of the Hole in a elastic plane.	132

LIST OF FIGURES

Figure 2.1: Taxonomy of nodal status. The node status types encountered in contact analysis are indicated by thick borders.	14
Figure 2.2: Algorithm I: A contact algorithm similar to Ahn & Barber flow chart	17
Figure 2.3: Algorithm II: The Method of First Violation contact algorithm with adaptive load step flow chart	19
Figure 2.4: Comparison between a conventional contact algorithm and the Method of First Violation contact algorithm. With conventional contact algorithms, a load step is selected and an iterative procedure is used to find an admissible set of loads and displacements consistent with that load step. With the Method of First Violation, the load step is computed to be exactly that necessary to bring the first node to change status (contact, non-contact, stick, and slip)	22
Figure 2.5: Single node illustration for contact and non-contact violations. The thick (blue) solid dashed lines represent admissible configurations and the thin (orange) solid and dashed lines represent inadmissible configurations. For instance if a node begins not-in-contact (thick dashed line on the left), as the load step δL increases, the gap closes linearly until contact occurs at δL_w , as the load further increases the gap stays at zero and the contact pressure increases linearly (thick solid line on the right.)	25
Figure 2.6: Single node illustration for stick and slip violations. The dark (blue) solid and thick lines represent admissible configurations and the lighter (orange) solid and dashed lines represent inadmissible configurations. For an initially stuck node (dashed thick (blue) line), calculation of shear traction exploits linearity of that traction to obtain the new δL_τ of stick violation. For an initially slipping node (solid thick (blue) line), calculation of change in $sgn(\dot{u})$ will require the method of bisection to obtain δL_{ii} of slip violation.	25
Figure 3.1: Verifying the half-plane compliance matrix formulation with the analytical solution. The two numerical algorithms yielded identical solutions. The * and \square represent numerically calculated traction at the centers of intervals. The continuous curves are analytic	29
Figure 3.2: Verifying the half-plane compliance matrix formulation with the analytical solution. The two numerical algorithms yielded identical solutions. The * and \square represent numerically calculated traction at the centers of intervals. The continuous curves are analytic	30

Figure 3.3: Verifying numerical normal and lateral traction distribution with analytical expression for rigid cylinder pressing against an elastic half-plane with coefficient of friction ($\mu_s = 0.3$).	31
Figure 3.4: Verifying numerical normal and lateral traction distribution with analytical expression for rigid flat indenter pressing against an elastic half-plane with coefficient of friction ($\mu_s = 0.3$).	32
Figure 3.5: Stick ratio for cylindrical indenter with and without decoupling assumption	33
Figure 3.6: Stick ratio for flat indenter with and without decoupling assumption	33
Figure 3.7: Stick ratio vs friction with full elastic coupling for cylindrical indenter	34
Figure 3.8: Stick ratio vs friction with full elastic coupling for flat indenter	34
Figure 3.9: Mapping of two elastic cylinder contact to the rigid cylinder over the half-plane	36
Figure 3.10: Verifying numerical stick ratio with analytical expression for Mindlin solution.	37
Figure 3.11: Comparing numerical tractions from Algorithm-I, Algorithm-II, and analytical expression for one-parameter friction model ($\mu = 0.7$) after application of lateral force: normal pressure distribution (left) and lateral traction distribution (right).	38
Figure 3.12: Comparing numerical tractions from Algorithm-I and Algorithm-II for two-parameter friction model ($\mu_s = 0.7, \mu_k = 0.42$) after application of lateral force: normal pressure distribution (left) and lateral traction distribution (right). For Algorithm-I, the region of stick is indicated by a solid black line, and the region of slip is indicated by a black line connecting solid green circles (●). For Algorithm-II, the region of stick is indicated by a dashed blue line, and the region of slip is indicated by a dashed blue line connecting red dots(●).	39
Figure 3.13: Normal and lateral traction distribution after a normal and lateral pressing of the cylinder against an elastic half-plane with coefficient of friction $\mu_s = 3$. Comparing the Algorithm-I and Algorithm-II with 85 contact nodes in both cases.	41
Figure 3.14: Normal and lateral traction distribution after a normal and lateral pressing of the cylinder against an elastic half-plane with $\mu_s = 3$. Comparing the tractions predicted by Algorithm-II using a fine mesh (FM) having 85 nodes in the contact patch and those predicted by Algorithm-II using a coarse mesh (CM) having only 42 nodes in the contact patch.	42

Figure 3.15: Implementing of the Method of First Violation algorithm with the Dahl friction model: ($\sigma = 1000, \gamma = 1, \mu_s = 0.3$). Algorithm-I would not converge to a solution for Dahl friction model.	43
Figure 3.16: Normal and lateral traction distribution calculated for two-parameter friction ($\mu_s = 0.7, \mu_k = 0.49$) through Algorithm-I and Algorithm-II after a rigid cylinder is pressed against an elastic half-plane with a normal force ($P = 0.001$).	44
Figure 3.17: Normal and lateral traction distribution calculated for two-parameter friction ($\mu_s = 0.7, \mu_k = 0.49$) through Algorithm-I and Algorithm-II after a rigid cylinder is pressed against an elastic half-plane with a normal and lateral forces ($P = 0.001, Q = 0.000185$). Slipping nodes are represented through 'red o' and 'Green *' for A-I and A-II respectively.	45
Figure 3.18: Evolution of lateral traction with lateral cyclic loading (Arrow shows the direction of lateral loading.) All tractions shown are physical traction normalized by G . [16]	47
Figure 3.19: Number of iterations (N_{ite}) vs load-step (δL_0) using Algorithm-I for coarse to fine contact mesh (red marks shows the bad converged solution). Optimal load increments for this method on this problem are suggested by the dashed blue curve.	49
Figure 3.20: Number of iterations (N_{ite}) vs load-step (δL_0) using Algorithm-II(MFV) for coarse to fine contact mesh (Black marks shows the optimal load-step for faster and accurate solution). The blue dashed line is copied from Figure 3.19.	50
Figure 4.1: A contact problem with normal (P) and lateral (Q) forces are applied pressing an elastic disk against a rigid surface with 33 boundary nodes in contact (11 nodes in each 4° contact region).	53
Figure 4.2: Flow chart using Michell expansion to create a compliance matrix.	58
Figure 4.3: A solid disk with discretization from $-\pi$ to π	61
Figure 4.4: The displacement field resulting from the unit pressure over $\Delta\theta$ centered at $\theta = 0$ is obtained by summing a Fourier series. Though there would be Gibbs phenomena if the pressure field were recovered from Fourier series, there is no Gibbs phenomena associated with the displacement field.	62
Figure 4.5: An infinite plane with a hole discretized from $-\pi$ to π	65
Figure 4.6: On moving the unit normal pressure the corresponding displacement field (dashed) is also moving that is one of the columns of compliance matrix	68

Figure 4.7: Shifting of the displacement basis to create compliance matrix	70
Figure 5.1: Two concentric elastic cylinders pressed against each other	73
Figure 5.2: A rigid cylinder pressed inside a hole in an elastic half-plane	74
Figure 5.3: Comparison of analytical and numerical normal pressure distribution for a elastic cylinder pressed against a rigid half-plane with a coarse mesh (on top) and with a fine mesh (on bottom).	75
Figure 5.4: Rigid cylinder indenter pressed against a hole inside an infinite elastic plane. . .	76
Figure 5.5: Elastic cylinder pressed against a rigid half-plane with friction. The stick ratios for multiple friction coefficients are compared with the analytical ex- pression provided by Spence.	77
Figure 5.6: Mindlin contact mapping is created using elastic cylinder pressing on a rigid half-plane with friction. Stick ratio for multiple friction coefficients are compared with analytical expression provided by Mindlin.	78
Figure 5.7: The Mindlin two-cylinder contact problem is mapped into that of an elastic cylinder pressed against a rigid half-plane with friction. The numerically calculated lateral traction distribution (connected lines) for multiple friction coefficients are compared with analytical values (dashed lines).	79
Figure 5.8: Contour plot for normalized von-Misses stress inside the elastic disk on pressing against rigid plane on friction free surface with contact angle 0.64° . The positions are non-dimensionalize with the contact length parameter (a). . .	80
Figure 5.9: Surface traction and displacement distributions for three cases: normal force P , only (left); Shear force, Q applied after normal force P and employing a Coulomb friction model (center); Shear force Q applied after normal force P and employing a two-parameter friction model (right).[17]	82
Figure 5.10: Stress distributions for three cases: normal force, P , only (left); Shear force, Q applied after normal force and employing a Coulomb friction model (center); shear force, Q applied after normal force and employing a two-parameter friction model (right). Horizontal and vertical coordinates are normalized by a . [17]	84
Figure 6.1: Surface traction distributions for three cases: fully coupled (FC) (in left); Goodman decoupled approximation (GD) (in center); fully decoupled ap- proximation (FD) (in right).	92

Figure 6.2: Normalized dissipation hysteresis and non-linear part of hysteresis: fully coupled (in left); Goodman decoupled (in center); fully decoupled (in right). Non-linear part is generated by removing the linear	94
Figure 6.3: For the five contact geometries, contact parameters such as Dissipation, Stick ratio, and errors in surface tractions are plotted against over a range of lateral force (\tilde{Q}). All calculation involved $\mu = 0.7$ friction coefficient.	96
Figure 6.4: For the five contact geometries, contact parameters such as Dissipation, Stick ratio, and errors in surface tractions are plotted against over a range of friction coefficients (μ). All calculation involved $\tilde{Q} = Q/(\mu P) = 0.99$ lateral force.	100
Figure 6.5: For a rigid cylinder pressed inside a circular hole of twice radius, contact parameters such as Dissipation, Stick ratio, and errors in surface tractions are plotted against over a range of friction coefficients (μ) and five different lateral ratio \tilde{Q}	101
Figure A.1: Coordinates x, y ; tractions p, τ ; and displacements u, w on the surface of an elastic half-plane	109
Figure A.2: Unit normal pressure and corresponding displacement on shifting by $-\Delta x$ and Δx	111
Figure B.1: Comparing Dahl friction model with Coulomb friction model.	114
Figure C.1: Stress distribution on the solid disk is equilibrated with forces and moment near the center.	117
Figure D.1: Stress distribution on the hole should be equilibrated with forces and moment applied on the indenter.	124

KEY TO ABBREVIATIONS

β Material Mismatch parameters (Dundur's Parameter)

θ angle at the contacting node form center

μ coefficient of friction for one parameter friction

μ_s Static coefficient of friction for two parameter friction

μ_k Dynamic coefficient of friction for two parameter friction

ν Poisson's ratio

σ_{rr} Radial Stress field

$\sigma_{r\theta}$ Tangential Stress field

$\sigma_{\theta\theta}$ Circumferential Stress field

σ_{vM} von-Mises Stress field

δL_o Load-step

$\Delta\theta$ angle of discretized interval in the contact region

Δx length of discretized interval in the contact region

Φ_o Michell's Airy stress function

a Half of the contact length

b Half of the stick length

c Stick ratio ($c = b/a$)

p Normal surface traction $p = \tau^y$

p^r Radial surface traction

p^θ Tangential surface traction

p_0 Normalizing pressure = $2P/\pi a$

τ Horizontal surface traction $\tau = \tau^x$

u Horizontal displacement

u^θ Tangential displacement

w Normal displacement field

w^r Radial displacement
 C_{Cart} Compliance matrix in Cartesian coordinate
 C_{Polar} Compliance matrix in polar coordinate
 C_{wp} Compliance sub-matrix correlates normal displacements to normal pressure
 $C_{w\tau}$ Compliance sub-matrix correlates normal displacements to lateral traction
 C_{up} Compliance sub-matrix correlates lateral displacements to normal pressure
 $C_{u\tau}$ Compliance sub-matrix correlates lateral displacements to lateral traction
 G Elasticity shear modulus
 K Twice the mean curvature of contacting bodies
 P Normal force
 Q Lateral force
 \tilde{Q} Non-dimensional lateral force ratio $\tilde{Q} = Q/(\mu P)$
 N_{ite} Number of iterations
A-I Algorithm-I, Conventional algorithm
A-II Algorithm-II, Method of First Violation
 A_{mn} Coefficient of Airy stress function
 B_{mn} Coefficient of Airy stress function
FD Full decoupling approximation
FC Full elastic coupling
GD Goodman decoupling approximation
MFV Method of First Violation Contact Algorithm

CHAPTER 1

INTRODUCTION

1.1 Overview

Two approaches for computational contact mechanics are explored to provide an accurate and robust numerical simulation of frictional contact. First, a novel contact algorithm - the Method of First Violation (MFV) - is developed and verified with available analytical solutions. The algorithm is compared with a more conventional algorithm on standard Coulomb friction indenter problems and then tested on problems involving two other friction models. Second, because of the computational advantages of compliance matrices in contact analysis, a compliance matrix formulation is derived for two-dimensional elastic disks and for circular holes in an infinite elastic plane.

1.2 Motivation

Structures involving bolted, riveted, and other types of joints for which frictional interfaces are fundamental, are ubiquitous in our industrial environment and the dynamics of such structures are greatly complicated by their interfaces, where these contacting surfaces suffer wear and tear and dissipate energy [2, 14, 61, 33, 73]. These contacting effects are good or bad depending on the structure's requirements, such as linearity, energy conservation, or higher damping near resonance. It is not easy to understand the actual dynamics due to the inaccessibility of the interfaces during the dynamic loading. Researchers have worked on the contact problems analytically and numerically in several ways, such as considering or ignoring friction, 2D or 3D elastic contact, and with full elastic coupling or with various decoupling approximations. To be tractable, these problem formulations still require substantial idealization.

The simplest problem that contains the interface mechanics associated with joint structures is the 2D contact between two co-axial elastic cylinders pressed together or a rigid cylinder pressing on an elastic half-plane. The frictionless case of such problems is commonly known as a 2D

Hertzian problem. Introducing Coulomb friction to the problem brings complications because of the inequality conditions for stick or slip constraints and an elastic coupling between normal and shear tractions due to Poisson's effects. Though coupling is not necessarily an issue with numerical solutions, it makes analytical analysis difficult and is usually mitigated using various decoupling approximations. The most common decoupling approximation is attributed to Goodman [31] asserting that "normal displacements resulting from lateral traction that are negligible in comparison to normal displacements resulting from normal traction." This decoupling approximation has been exploited regularly by researchers such as Mindlin [52], and Spence [63, 64] to provide analytical expressions for the width of the contact patch, stick-slip regions in the contact patch, lateral traction, displacement distributions, and relations between the lateral force and stick-slip ratio in terms of applied loads or displacements. Another, more severe, decoupling approximation ignores any elastic coupling between normal and lateral loads so that "normal and lateral displacements result only from normal force and lateral force respectively" [30, 69]. This decoupling approximation (complete decoupling) reduces the complexity of the problem significantly and results in faster though not-so-accurate predictions for contact parameters. It is mostly implemented to understand cyclic loading and uneven contact.

A serious limitation of most contact analyses is that only Coulomb friction is considered. However, Coulomb friction is the *zeroth* order approximation of frictional contact, and it performs poorly in cases involving the calculation of partial slip, such as is the case in structures with joint [67]. In order to develop better predictive joints models, it is necessary to explore other friction models, particularly with respect to their performance in partial slip. The underlying goal of this research effort is to develop a test-bed for the exploration of various friction models (such as identified by [11]) that, when used in contact models, will yield predictions that can be compared to experiments reported for mechanical joints [67]. These friction models bring their own complexity due to the introduction of multiple friction parameters and possibly more inequality constraints that must be incorporated in the implementation.

There is a very long history of calculating interface mechanics in the context of classical elasticity, but the intrinsic difficulty of the problem has restricted the number and nature of analytic solutions available, as well as the robustness and fidelity of numerical simulations. The numerical contact algorithms that have been developed over the decades appear to address most of the problems of practical importance, but they still suffer from issues of robustness and fidelity to the underlying equations. These limitations must be overcome to provide a test-bed for the study of the interface mechanics of joints.

A traditional complaint about numerical contact algorithms is that they often do not adequately take into account or correctly reproduce the path dependence found in analytic solutions [12, 47, 45]. The core notion motivating the new approach is that a valid numerical contact algorithm must satisfy all elasticity equations and all equality and inequality constraints of contact not only at the beginning and end of each load or displacement increment, but at all points in between. In this study, contact histories that conform to the above conditions are referred to as *admissible*. An algorithm, referred to as the Method of First Violation, developed to achieve admissible contact histories, appears to provide more physically reasonable predictions – particularly with respect to path dependence – than standard contact algorithms as well as greater robustness.

In order to get insight into interface mechanics through computation, an extraordinary fine mesh on the interface is required. The more prominent methods of surface discretization are: assembly of stiffness matrices obtained from finite elements, obtaining mixed system matrices from the boundary integral method, and, where possible, the development of a compliance matrix via semi-analytic methods. The stiffness matrix of the finite element formulation for contact problems tends to be very large because accuracy requires not only many nodes on the surface, but at least a gradual transition of element sizes away from the surface. A process of static reduction [23] is then used to replace the (often huge) stiffness matrix with one that involves only surface degrees of freedom. This process of resolving out internal degrees of freedom is routinely done, but is computationally challenging [25, 69].

The boundary integral method involves only nodes on the surface and requires a gradual

transition of element size away from the contact patch. The results is two system matrices much smaller than those obtained via finite element method: one acting on a column of surface tractions and the other acting on a column of displacements [48]. These two matrices are resolved to yield a stiffness or compliance matrix, but a compliance matrix is preferable for the reasons discussed next. There are a few geometries (such as the surface of a half plane) where it is possible to construct a compliance matrix using semi-analytic methods. The only rows and columns of such a compliance matrix that need to be considered are those associated with nodes in the vicinity of the contact patch, all surfaces outside that contact region are traction-free. This facilitates the creation of an extremely fine mesh without necessarily requiring the solution of an unreasonably large system of equations.

For numerical experiments on contact algorithms, compliance matrix for the half-plane is constructed using analytic expressions for the displacement field resulting from uniform tractions over finite intervals on the surface [35, 53]. The advantage of constructing a compliance matrix is that it avoids having to resolve down the system of equations resulting from finite element or boundary integral method. Additionally, the compliance formulation accommodates the complexity of frictional contact with various levels of elastic coupling, which can be turned on and off on demand. In order to have these same advantages in contact calculations of curved 2D elastic bodies, a method for direct calculation of compliance matrices for planar elastic disks and holes in an infinite elastic plane was developed.

1.3 Literature Review

Solving a contact problem depends on a robust and efficient algorithm (static, dynamic, friction, or no-friction). There are multiple kinds of algorithms in literature such as contact detection algorithms, mortar-based algorithms, Lagrangian-based contact algorithms with or without Coulomb friction, contact optimization algorithms, mesh-based and meshless contact algorithms, and Quasi-static contact algorithms [13]. In this paper, we focus on the Quasi-static contact algorithms for elastic contact and discuss the various algorithms to capture the quasi-static contact process with

and without friction.

1.3.1 Friction-Free Contact Algorithms

Conry and Seireg[22], and Kalker and van Randen[43] are among the earlier examples of algorithms for friction-free contact analysis. Conry and Seiberg [22] used a simplex algorithm for solving the contact problem through linear complementarity conditions. On the other hand, Kalker and van Randen [43] solved the normal contact between two dissimilar elastic materials by employing two energy functions (contact elastic energy and contact enthalpy). Minimization of these energy functions was used to estimate the pressure distribution between two contacting surfaces through a quadratic programming approach because of their convex behavior. This approach became the baseline for developing new contact methods and approaches with advancement in computational capability. Polonski and Keer [54] used the conjugate gradient method (CGM) to minimize the contact energy functions to find the pressure distributions on a coarser mesh and then used the multi-level multi-summation (MLMS) technique to get the results for a finer mesh in a normal contact analysis. This approach resulted in a faster estimation of results in a very finely discretized domain.

Johnson [38] used the Fourier representation of pressure and displacement to develop a relationship for estimating normal pressure distribution through surface displacements and vice-versa. Ju and Farris [39] further investigated this convolution and developed an error estimation method. They observed that the loss/error of high-frequency content in pressure FFT does not cause large errors in displacement and load, while the loss/error in the low frequency does lead to large errors in displacement and load. Therefore the contact length needs to be significantly small compared to the length of the FFT window. They also suggested various other ways to reduce errors for generalized two surface contact. Liu and Wang [50] further explained this convolution domain for an elastic punch on a rigid half-plane. Because of the implicit periodicity associated with the use of Fourier methods, there can be artifacts of interference between tractions fields in adjacent periods and Liu and Wang showed how this is mitigated if the spatial periods are chosen to be large relative

to the contact patch. They further introduced a Discrete Convolution Fast Fourier Transformation (DC-FFT) technique, where influence coefficients from finite element analysis were mapped onto the spatial frequency domain. They explored five different approaches to reduce the numerical errors when solving the discretized normal contact problem. They identified DC-FFT as the fastest method to solve the line contact problem. Stanely and Kato [66] used the FFT relations provided by Johnson [38] with minimization of total complementary energy to solve for the contact between two surfaces, demonstrating fast convergence for two-dimensional normal contact.

Allwood [3] provided a brief survey on contemporary (2005) methods of tackling the contact problem. He employed Kalker's approach of obtaining a stiffness matrix through FEM analysis and then used that stiffness matrix to compare three different contact algorithms. In the first technique he examined, a reduced stiffness matrix is developed using Duncan/Gunyan [25] reduction, and that reduced matrix is solved subject to the constraints associated with the currently assumed status of the nodes. An iterative process is established where one node status is changed at a time, and the elasticity problem is resolved. The second method was based on Kalker's [43] approach of first formulating the energy function and later minimizing it with the conjugate gradient method. After minimization, if any contact nodes do not satisfy their inequality constraints, then their status is updated, and the minimization is done again. This iterative procedure is continued until all nodes satisfy all contact constraints and inequalities. This method is slower than the other two because the energy function must be minimized in each iteration. Polonsky and Keer's [54] approach of FFT-based MLMS to calculate the contact was the third method explored by Allwood. This last method is the fastest but least accurate of the three methods.

Allwood and Ciftci [4] provided a new algorithm based on incremental load again using a reduced stiffness matrix. The normal load is increased slowly to solve for the contact area and pressure iteratively until the required load is reached. In the case of any inequality condition that is not satisfied, a new load increment gets selected through a linear correlation such that the gap or penetration reduces to zero. This incremental approach resulted in a faster solution with a low number of iterations. This method by Allwood and Ciftci can be seen as an antecedent to the

Method of First Violation algorithm.

1.3.2 Contact Algorithms with Friction

Friction brings complexity to the contact problem due to nonlinear interaction between shear loads and normal loads at each contacting point, requiring a solution for lateral traction fields and satisfaction of stick or slip inequalities. Kalker [40, 41] performed analysis on elastic cylinders in rolling using dry Coulomb friction. He used known Hertzian analytic expressions for the normal pressure and then calculated the lateral traction. He posed the traction problem as one of minimization subject to linear inequality constraints that could be solved using a simplex algorithm. He later derived a more general approach [42] by separately solving normal and lateral contact as a convex minimization problem. He devised algorithms NORM, TANG, and PANA to solve only normal contact, lateral contact, and coupled normal and lateral contact, respectively. In PANA, TANG and NORM were solved in turn one by one, where the result of one was input of the next. This process of sequential solving was repeated until the solution converged. Klarbring et al. [46] provided another approach for the quasi-static contact problem with dry friction and linear elasticity using variational inequalities. They observed that small increments in the loads could result in faster convergence. In other work, Klarbring et al. [45] discussed the non-uniqueness and non-existence of contact solutions for single node contact in several cases, when the friction coefficient is larger than the ratio of stiffness for normal contact (S_N) to stiffness coupling between normal displacement and tangential load (S_{NT}), i.e. $\mu > S_N/S_{NT}$. Cho and Barber [20] extended this by incorporating inertia of contacting interfaces to consider the dynamic effects of the problem. This non-uniqueness is also shown for a two node system by Andersson et al. [5] which can extend to multi-node systems. Cho and Barber [21] also addressed the issue of stability in three-dimensional contact as defining the direction of slip and friction force is difficult and can result in an inconsistent solution.

Ahn and Barber [1] devised a contact algorithm for two-dimensional cyclic frictional contact that can distinguish the stick-slip boundary and capture the contact history. They solved normal

and lateral contact simultaneously, and used a reduced-order stiffness matrix with a Gauss-Seidel procedure while updating each node to satisfy all the contact inequalities within some tolerance. Note that, this is a relaxation scheme requiring iteration at each load increment. All the contact equality and inequality constraints are satisfied at the end of each load step, but multiple node statuses are permitted to change in a single iteration. Chen and Wang [19] extended the FFT-based normal contact analysis of Liu and wang [50] to lateral contact analysis with Coulomb friction. They created discrete influence coefficients to obtain explicit relations between pressures and displacement distributions. They also solved normal and lateral contact separately using CGM and later combined those to satisfy the contact inequalities. Moreover, they changed constraints status in each iteration and verified the results with an analytical expression provided by Hills et al. [35].

Spinu [65] presented an approach based on Allwood's method [4], first solving the normal contact and lateral contact separately and later coupling them to approximate a better contact solution. The method appears to provide fast convergence to solutions in three-dimensional elastic contact.

1.3.3 Path Dependence in Contact Algorithms

Several authors [12, 45, 46, 49, 59] discuss the path dependence of contact problems with friction. Klarbring [46] demonstrated that the dissipative nature of friction leads to path dependence, so "the final configuration depends on the way loads reach their final state, not only on the state. For an incremental problem to capture exactly this phenomenon, the increments must be infinitesimal, which is impossible from the point of view of practical numerical calculations. Within one increment the path dependence is neglected, although when more increments are considered the path dependence is preserved". It is generally presumed – that for the discretized problem – the time steps may be finite, but they must be sufficiently small in a manner determined by the discretization. Bertocchi [12] showed that for a problem involving a single node, convergence is achieved, and path dependence is respected when the load increments are chosen precisely to bring the node to its

next status change. In this way, he addressed the change in node status resulting from increments in normal or lateral load or increments in both. He described the geometric nature of admissible status for various loading conditions, which can be used for multiple nodes wherein only one node changes its status at a time.

As mentioned above, Klarbring et al. [45, 46] discussed the issue of existence and uniqueness of solutions of frictional contact problems and the role of load history with respect to the current traction/displacement state. Another view of the observation of Klarbring et al. [45, 46] is that two different load histories resulting in the same net force can have different interface traction distributions, differing by some self-equilibrating shear traction distribution. Or equivalently, the load history is captured in the traction distribution at the interface. A concern with methods that involve iterating through solutions without consistent states and status (non-physical configurations) is that they scramble the histories stored as interface traction. The above is not an issue with friction-free problems, where the solution is independent of history and can be solved by minimization of energy functions.

1.4 Thesis Synopsis

This thesis presented here is divided into three parts. Each part is detailed and provides a proper explanation on its own. The reader may skip a part without losing the thread of the discussion.

In the first part, the development of a new contact algorithm (Method of First Violation) is described. To understand the need and motivation, a conventional contact algorithm is also discussed before delving into the Method of First Violation. Both contact algorithms are employed in a contact problem – a rigid cylinder pressing against an elastic half-plane – using a compliance matrix formulation. Both algorithms are initially verified with analytical expressions available in the literature and later compared with each other. Multiple friction models are employed to ensure the robustness of the Method of First Violation (MFV). The MFV contact algorithm also appears to capture path dependence associated with contact mechanics with good fidelity.

In the second part, an extremely fine discretization method is engineered to create a compliance

matrix for the two-dimensional circular elastic cylinders, disks, and holes in an infinite elastic plane. The Michell's Airy stress function is used with the Fourier series expansion to derive a displacement basis. These displacement bases are assembled together to form a compliance matrix. The compliance matrices for elastic cylinders and holes are verified with analytical expressions where available. The test-bed of compliance matrix and Method of First Violation is tested for a contact problem of two identical elastic cylinders pressed together and sheared. This compliance formulation can analyze the contacting interface using a very fine mesh in the surface requiring the minimum number of degrees of freedom.

In the third part, Goodman decoupling and full decoupling approximations are compared with full elastic coupling using five contact problem geometries. Contact problems, where contacting bodies are pressed against each other under a cyclic shear loading, are numerically simulated using the compliance matrix formulation and the MFV contact algorithm. Contact parameters such as surface tractions, stick ratios, dissipation, and L1 error in surface tractions are measured over a range of friction coefficients and lateral force ratios. Both qualitative and quantitative differences are identified and discussed.

Lastly, a summary of the work undertaken in this dissertation is reported, highlighting the final conclusions and remarks. A few recommendations are provided for the continuation of this research.

PART I

The Method of First Violation (Contact Algorithm)

CHAPTER 2

CONTACT ALGORITHMS

Though the algorithm - Method of First Violation - can be employed for the contact of surfaces of two curved (and not necessarily convex) elastic bodies, for simplicity this method is illustrated here for the case of contact of a rigid indenter on an elastic half-plane. Further, though there is no barrier to employing this new algorithm on problems where discretization is developed in a stiffness formulation (as is most common in finite element method) or in a mixed formulation (such as usually results from boundary integral method), or as illustrated below where the discretization results in a compliance formulation.

2.1 Compliance Formulation

In contact calculations discussed below, discretization is achieved using the equations for displacement resulting from a uniform normal or shear traction on a finite interval of a half-plane ([35, 72]). Each column of the compliance matrix is the collection of displacements due to the traction on a corresponding interval evaluated at the centers of the array of intervals.

Because there are arbitrary horizontal and vertical displacements in the elasticity equations for an elastic half-plane, these arbitrary displacements are absorbed in rigid body displacements W_{tot} and U_{tot} in the compliance formulation of Eq. 2.1.

$$\left\{ \begin{array}{c} \vdots \\ w_n \\ \vdots \\ u_n \\ \vdots \\ \hline P \\ Q \end{array} \right\} = \left[\begin{array}{cc|cc} C_{wp} & C_{w\tau} & 1 & 0 \\ & & \vdots & \vdots \\ C_{up} & C_{u\tau} & 0 & 1 \\ & & \vdots & \vdots \\ \hline \Delta x & \dots & 0 & 0 \\ 0 & \dots & \Delta x & 0 \end{array} \right] \left\{ \begin{array}{c} \vdots \\ p_n \\ \vdots \\ \tau_n \\ \vdots \\ \hline W_{tot} \\ U_{tot} \end{array} \right\} \quad (2.1)$$

where p_n is the uniform pressure applied in interval n ; τ_n is the uniform shear traction applied in interval n ; w_n is the downward motion at the center of the interval n ; u_n is the horizontal displacement at the center of the interval n ; P is the net downward force applied by the indenter; and Q is the net horizontal force applied by the indenter. The full mathematical formulation details are presented in appendix A.

In this equation, the compliance matrix itself is divided into four parts (C_{wp} , $C_{w\tau}$, C_{up} , and $C_{u\tau}$), where C_{wp} correlates normal displacements to normal pressure, $C_{u\tau}$ correlates lateral displacement to lateral traction, C_{up} correlates lateral displacement to normal pressure, and $C_{w\tau}$ correlates normal displacement to lateral traction. Also matrices C_{wp} and $C_{u\tau}$ are identical, i.e. $C_{wp} = C_{u\tau}$, and matrices $C_{up} = -C_{w\tau}$. The Goodman decoupling approximation is achieved by setting $C_{w\tau} = 0$.

The numerical efficiency of the surface compliance discretization approach shown here is worth discussing. Not only are there no nodes internal to the half-plane, but one needs to discretize only the interval of interest $(-R, R)$ containing the anticipated contact. Admittedly, this particular compliance formulation applies only to the half-plane, but this provides an excellent test-bed for preliminary investigation of the contact algorithm discussed in this chapter.

The sort of discretization shown here, is discussed in [35] and more recently in [72], where the compliance matrix is presented as a step to obtaining a stiffness matrix used in deducing tractions associated with an imposed indentation. Sayles discusses this approach to discretization broadly in [60]. Webster and Sayles [71] employed this approach to address rough surface contact. The first to have used this approach (using chapeau functions) appears to have been Bental and Johnson [10].

2.1.1 Taxonomy of Contact Status

With reference to figure 2.1, we observe that when one considers all possible node statuses in the context of Coulomb friction (and several other models for friction), nodes may be 1) Not in Contact, 2) In Contact and Stuck, 3) In Contact and Slipping Left, or 4) In Contact and Slipping Right.

These four node statuses and the corresponding equality constraints and inequality constraints for Coulomb friction are shown in Table 2.1. (In this table, for Coulomb friction $f(p) = \mu p$.)

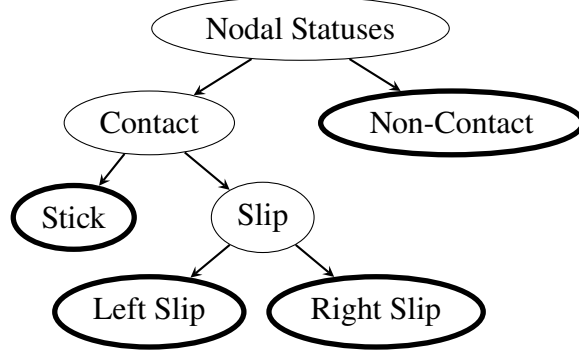


Figure 2.1: Taxonomy of nodal status. The node status types encountered in contact analysis are indicated by thick borders.

Nodal Statuses	Equality Constr.	Inequality Constr.
Contact and Stick	$\dot{u} = 0, w = g$	$ \tau \leq f, p \geq 0$
Contact and Slip Right	$\tau = -f(p), w = g$	$\dot{u} \geq 0, p \geq 0$
Contact and Slip Left	$\tau = f(p), w = g$	$\dot{u} \leq 0, p \geq 0$
Not-in-Contact	$p = 0, \tau = 0$	$w \leq g$

Table 2.1: Equality and inequality constraints for each node status type.

$$\left[\begin{array}{cc|cc} C_{wp} & C_{w\tau} & 1 & 0 \\ & & 1 & 0 \\ & & \vdots & \vdots \\ C_{up} & C_{u\tau} & 0 & 1 \\ & & 0 & 1 \\ \hline \Delta x & \dots & 0 & 0 \\ 0 & \dots & \Delta x & 0 \end{array} \right] \left[\begin{array}{c|c} -1 & \\ & -1 \\ & \vdots \\ & -1 \\ \hline \dots & -1 & 0 \\ \dots & 0 & -1 \end{array} \right] \left\{ \begin{array}{c} p_n \\ \vdots \\ \tau_n \\ \vdots \\ \hline W_{tot} \\ U_{tot} \\ \vdots \\ w_n \\ \vdots \\ u_n \\ \vdots \\ \hline P \\ Q \end{array} \right\} = \left\{ \begin{array}{c} 0 \\ \vdots \\ 0 \\ \vdots \\ \hline 0 \\ 0 \\ \hline p_c \\ w_c \\ \vdots \\ \tau_c \\ u_c \\ \vdots \\ \hline P \\ Q \end{array} \right\} \quad (2.2)$$

2.1.2 Compliance Matrix with Contact Constraints

Say at an instant, we know the correct status of each node. Then our inequality constraints are all satisfied and equality constraints are incorporated as additional linear equations. The larger matrix

is shown in Eq. (2.2), where the upper part of the matrix captures elasticity equations and the lower part captures the contact equality constraints through L_p , L_u , $L_{\tau p}$, L_{τ} and L_w . Normal pressure constraint matrix L_p fixes the pressure of non-contact nodes to be zero by setting constraint pressure $p_c = 0$ and its corresponding value in matrix $L_{p_c} = 1$. Geometric constraint matrix L_w fixes normal displacements of nodes in-contact by setting normal displacement $w_c = g_n$ and its corresponding value in matrix $L_{w_c} = 1$. Similarly, stick constraint matrix L_u sets the lateral displacements of the stick status node through $u_c = u_n$ and $L_{u_c} = 1$. For the case of slip constraints, we use a relation between lateral and normal pressure $|\tau_n| = \mu p_n$ for the Coulomb friction model through matrices $L_{\tau p}$ and L_{τ} . (The sign of τ_n depends on the direction of travel and is reflected in $L_{\tau p}$.) We set $L_{\tau_c} = 1$ and $L_{\tau p_c} = -\mu$ to the corresponding slip status node. The other four rows in the matrix allow us to fix the imposed load conditions through normal P and lateral Q force or normal W_{tot} and lateral U_{tot} displacement constants. With contact status and imposed boundary conditions, the matrix (2.2) is used to solve for new displacements and pressure resulting from increments in load, which are then compared with the inequality contact constraints to identify any violations. Changing the contact status of nodes requires a robust contact algorithm to perform all these comparisons and provide solutions. We will discuss this in the next sections. This approach – implementing equality constraint equations in the elasticity matrix to solve and later verifying the inequality constraints – is similar to the linear complementarity problem (LCP) formulation.

The size of the matrix (2.2) would appear to be large, but its dimension grows roughly as four times the number of nodes in the contact patch, so the computational requirements are still modest. One may either employ a fixed number of nodes and their degrees of freedom which are sufficient to capture the contact mechanics for the calculation of interest, or one may continuously change the set of nodes under consideration to include all those currently in the contact plus one more node on the either side. The resulting overall matrix size becomes $(4n + 12) \times (4n + 12)$ for n nodes in contact. Almost 70% of the matrix elements are zero, facilitating the use of sparse matrix solvers. When the number of nodes in contact is $O(n)$, the time to solve the elasticity matrix will be $O(n^2)$.

The purpose of introducing the surface compliance formulation above is solely to define the

discretization on which the Method of First Violation is illustrated below. This contact algorithm is not restricted to such discretizations.

2.2 Algorithm I

The new algorithm - Method of First Violation - is a major improvement on conventional algorithms. First, a conventional algorithm is presented for comparison. Contact algorithms are complex and have multiple parameters, so before delving into specific algorithms, let us assign a term “nodal parameters (H)”, which contains these four contact surface parameters normal pressure, lateral traction, normal displacement, and lateral displacement (p, τ, w, u). We also refer to the four kinds of contact status associated with nodes provided in the Tab. 2.1. Each node will have only one contact status and corresponding equality and inequality constraints (S). The collection of node statuses and nodal parameters (S, H) defines the contact configuration. An equilibrium configuration is one for which the parameters for each node satisfy the equality and inequality constraints of each node’s assigned status, and the collection of displacements and tractions on each side of the interface are consistent with the elasticity equations for the corresponding body.

The first contact algorithm presented here is very similar to that of Ahn and Barber [1]. It differs from [1] in that to make the process more robust, at the beginning of each new load step all the nodes that were in contact at the end of the previous load step are assumed to be stuck. On each iteration, the contact inequality constraints are checked and just one node status change is allowed at each iteration until a converged solution is found for the given load increment.

This contact algorithm is briefly explained with a flow chart shown in Fig 2.2. The algorithm starts with an initial equilibrium contact configuration (H_0 & S_0) and total final imposed load (L_{tot}), such as total normal force or displacement. To reach the final imposed load (L_{tot}), a load step (δL_0) is selected according to the number of steps anticipated to be needed to cover the contact history. Even a single load ($\delta L_0 = L_{tot} - L_0$) step may be enough to reach the final state, but a small load step enhances the chances of convergence. After choosing a load step, matrix (Eq. 2.2) is solved with all contact nodes status to stick. The resulting new contact parameters (p_n, τ_n, w_n, u_n) are

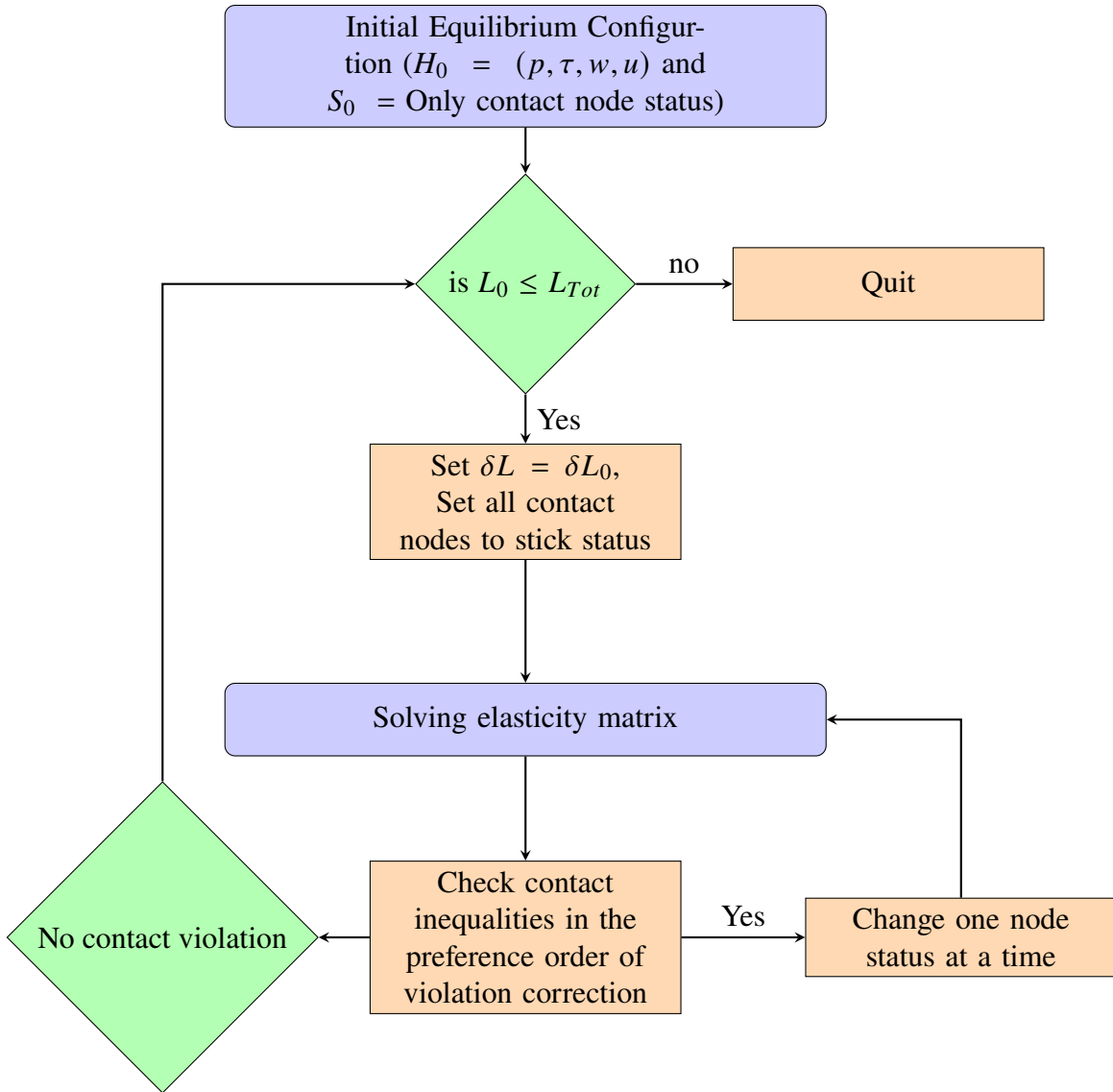


Figure 2.2: Algorithm I: A contact algorithm similar to Ahn & Barber flow chart

compared to their respective inequality constraints to check for the contact violation. Only one violation gets fixed at a time in the preference order of “geometric inter-penetration”, “negative normal pressure”, and “slipping”. An elasticity matrix (Eq. 2.2) is solved again using the new contact status. Multiple iterations may be needed to get a converged contact solution without any contact violation. This converged solution is used for finding a new solution with a new load step, where it again starts with all contact nodes to stick status.

This algorithm usually works well with the Coulomb friction, showing a few issues, especially

in an elastically fully coupled case. For instance, there are situations where the algorithm identifies a violation at the end of a time step, changes node status to avoid that violation, but then finds a different violation at the end of the time step. This can be an unending cycle. This issue can be resolved by changing the multiple statuses manually or with a small load step, or implementing both simultaneously.

This algorithm can also have issues with other friction models such as the two-parameter friction model (μ_s and μ_k) and the Dahl friction model where the constraint inequality ($\tau \leq \mu_s p$) is different from the slipping traction ($\tau = \mu_k p$). This problem can arise even with extremely small time steps. To resolve these issues, we developed a new algorithm with an adaptive load step that shows substantially more robustness.

2.3 Algorithm II: Method of First Violation

As discussed at the end of section 1.3.3, a concern with methods that involve iterating through solutions without consistent nodal parameters and nodal statuses (non-physical states) is that they scramble the contact histories stored as interface traction. The contact algorithm method that follows is designed to avoid iterating through non-physical configurations, so as to preserve consistent evolution of traction distribution with load history, and to provide unique and consistent solutions.

The second algorithm is a modification of the more standard algorithms, such as Algorithm I, and follows the linear complementarity problem (LCP) approach. It is best understood through the following observations:

1. the contact problem is piece-wise linear. Consider the following thought experiment.
 - Say at some instant the status of every node is known and reflected in Eq. 2.2. The horizontal load at that time is Q .
 - Say that the horizontal load is incremented by δL and that all of the inequality conditions consistent with the initial node statuses remain satisfied.
 - Say that instead of using load increment δL , we used $\alpha \delta L$ where $0 \leq \alpha \leq 1$. Because

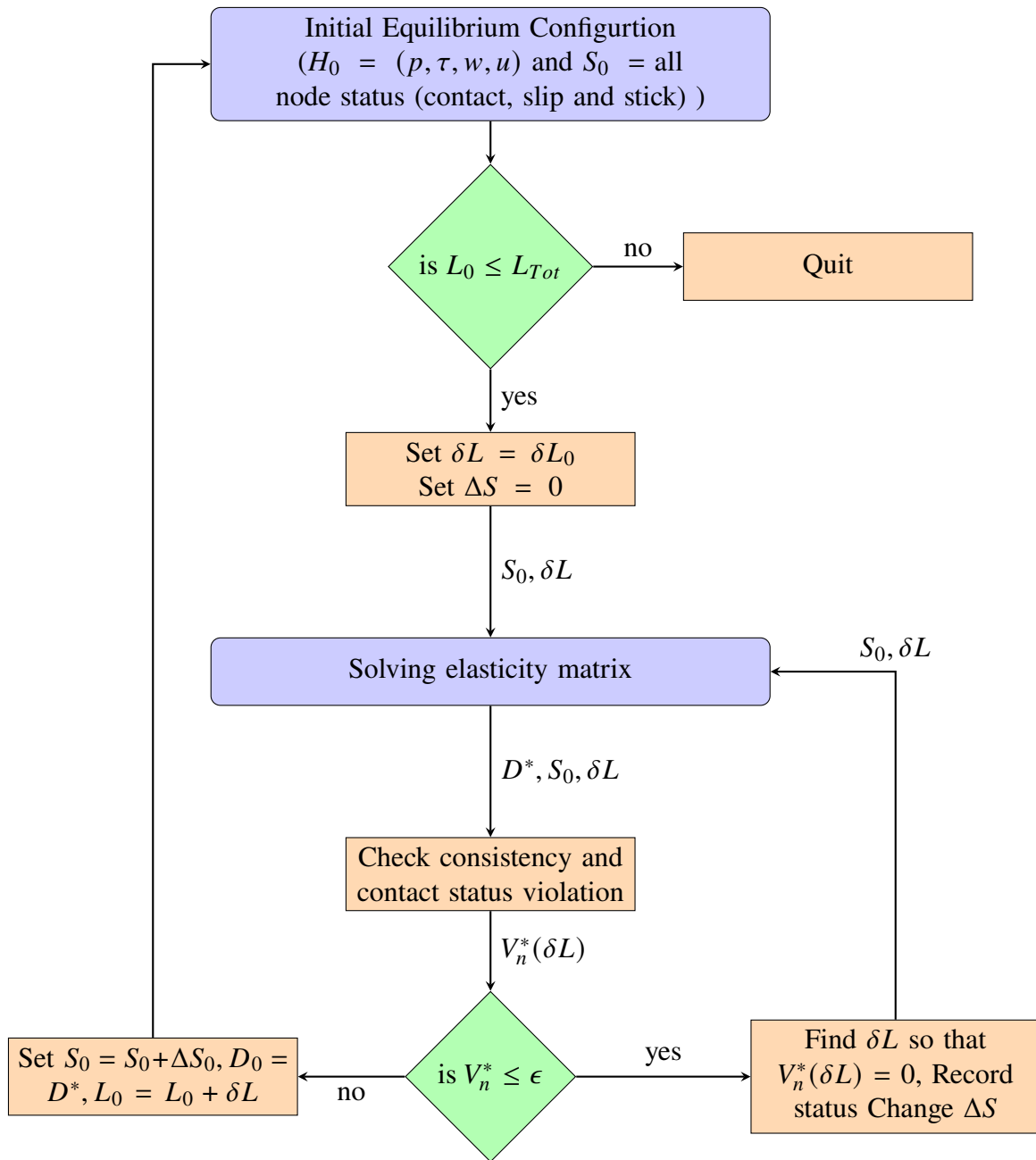


Figure 2.3: Algorithm II: The Method of First Violation contact algorithm with adaptive load step flow chart

matrix of Eq. 2.2 remains unchanged and the right hand side of Eq. 2.2 changes only through the value of $Q + \alpha \delta L$, then all the changes in the contact parameters p_n , τ_n , w_n , and u_n will be linear in α .

- Examination of the inequalities of Table 2.1, shows that they all remain satisfied for all $0 \leq \alpha \leq 1$.

We conclude that if all the node statuses at the beginning of the load step also prevail at the end of the load step, then the nodes will not change status at the loads in between. The version of the compliance matrix (Eq. 2.2) that reflects the node status at the beginning of the load step will consistently reflect the contact values and status throughout the load step, and consequently *the discretized contact problem is piece-wise linear*.

2. Except for the case of macro-slip, there exists a minimum load increment that will cause any violation of inequality constraints associated with the current node status. This greatest lower bound is a consequence of the completeness of the real number line [55](p.7). We can define $\overline{\delta L}$ such that $L + \overline{\delta L}$ is that greatest lower bound.
3. The value of $\overline{\delta L}$ can be calculated through a finite number of steps as follows:
 - a) Choose a load increment δL_0 sufficient to cause one or more violations. Let us call this set of violations V_0 .
 - b) Select one of those violated inequalities of V_0 and calculate the load increment δL_1 that exactly turns that inequality constraint into an equality constraint.
 - c) Substitute $L + \delta L_1$ for Q in Eq. 2.2 to solve for all tractions and displacements. Test those states against the inequality conditions to see if any violations remain. If there are no other violations, then define $\overline{\delta L} = \delta L_1$.
 - d) If there are remaining violations, note that because of the linearity of Eq. 2.2, they are a subset of V_0 . Choose one and find the corresponding δL_2 . By construction, $\delta L_2 \leq \delta L_1$.

Also, note that each recalculation of δL_n reduces the number of remaining inequality violations by at least one.

e) Continue this process until inequalities of V_0 are resolved, and $\overline{\delta L}$ is obtained.

Note that the above process involves a maximum number of steps if one were at every opportunity to make an incorrect choice of which violation to fix. In fact, there are strategies to make good choices, such as identifying all violations within each class – say interpenetrations – and starting with the worst of these violations.

4. At the end of that load step $\overline{\delta L}$, the inequalities of the beginning of the load step are still satisfied. Immediately beyond that load increment, some node status will change, and by definition, the new inequality and equality constraints will also be satisfied at the special $\overline{\delta L}$.

The distinction between the conventional approach and the Method of First Violation is illustrated in figure 2.4. The conventional algorithm (Algorithm-I) solves the contact violation by iterating on the same load step δL_0 . In the case of a large load-step δL_0 , solving multiple contact violations through an iterative approach may lead to a non-converging or a wrong solution. Conversely, the Method of First Violation (Algorithm-II) finds the new δL_1 (independent of initial load-step δL_0) satisfying all contact equality and inequality constraints.

2.3.1 Admissible Contact Histories

The issue of convergence of conventional numerical contact algorithms has been a continuing issue. A reasonable hypothesis is that iterative processes to find consistent tractions and displacements at the end of each load step may wipe out the information on the interface contact/slip history - as recorded in self-equilibrating traction fields. This loss of information is suggested by occasional node-to-node discontinuities in traction or jumps in nodal traction from one load step to the next, even during monotonic loading, when conventional contact algorithms are employed.

The algorithm outlined in Steps 3a through 3e above is presented as flow chart in figure 2.3. By construction, all equality and inequality constraints associated with the node statuses of each

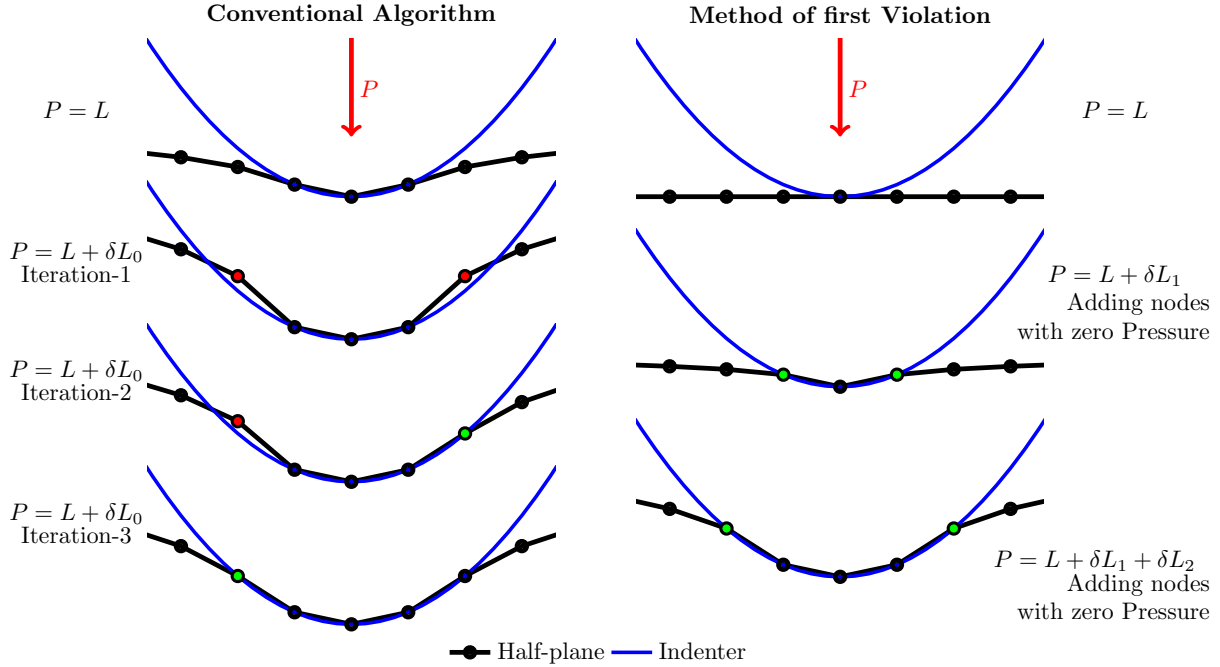


Figure 2.4: Comparison between a conventional contact algorithm and the Method of First Violation contact algorithm. With conventional contact algorithms, a load step is selected and an iterative procedure is used to find an admissible set of loads and displacements consistent with that load step. With the Method of First Violation, the load step is computed to be exactly that necessary to bring the first node to change status (contact, non-contact, stick, and slip)

load step are satisfied at the beginning of the load step, and the end of the load step, and at all loads in between. When one considers one load step after another, one sees that these calculations result in a consistent set of loads and interface tractions and displacements that satisfy all elasticity equations, all equality constraints, and all inequality constraints thorough-out the loading history. In this way, at any point in the loading history, all node statuses, all tractions, and all displacements are consistent with all that has happened prior to that point. One would hope that this fidelity of contact history would eliminate – or at least mitigate – the issues of tractions oscillating from one node to the next, as well as the problems with mesh convergence.

Finally, though the above explication used increments in shear load Q for the purpose of discussion, one could easily employ increments in normal load P , increments in lateral displacement U_{tot} , or increments in normal displacement W_{tot} . Of course, any desired history of imposed loading or imposed displacements could be constructed from the sequential incremental imposition of these

four quantities.

2.3.2 Contact Status Violations

Finding a Contact Status Violation (CSV) and resolving it is key to solving contact problems through this new algorithm (2.3). We define four kinds of CSV: 1) Geometric Violation, 2) Normal Pressure Violation, 3) Slip Violation, and 4) Stick Violation. As indicated above, in the case of multiple CSVs, we can choose any of them to start with to calculate the new δL . If there remain other CSVs at this load increment, they will be used to calculate new and smaller δL s. We continue to shrink δL in this process until we have the load increment that is just enough to trigger just one CSV. The calculation of the new δL associated with a violation depends on the type of violation, as discussed below.

2.3.2.1 Geometric Violation

A geometric violation occurs when the contact configuration suggests an interpenetration between two contacting surfaces. Say a node is assumed to be non-contacting, the corresponding geometric condition is $w_n \leq g_n$ [39] (where g_n is the indenter node displacement), and if it transpires that a load increment δL_0 results in nodal displacement $w_n > g_n$, then inter-penetration has taken place. In this case, a new δL is calculated to bring the interpenetrated node exactly to the contacting surface ($w_n = g_n$) through Eq. (2.3), where w^* , w_0 , and g are the current violating/penetrating displacement, previous equilibrium displacement, and indenter displacement.

$$\frac{\delta L_w}{\delta L_0} = \frac{g - w_0}{w^* - w_0} \quad (2.3)$$

2.3.2.2 Normal Pressure Violation

A normal pressure violation occurs when load increment δL_0 causes a node that is nominally in contact to have negative normal pressure. The new load step δL is calculated to make the normal pressure exactly zero:

$$\frac{\delta L_p}{\delta L_0} = \frac{p_0}{p_0 - p^*} \quad (2.4)$$

where p^* and p_0 are the normal pressure associated with δL_0 and the normal pressure of previous equilibrium state, respectively.

2.3.2.3 Violation in Stick Constraints

Violation in a stick constraint occurs when the load step δL_0 causes a node with that contact status to have a new lateral traction sufficient to overcome the friction force ($|\tau| \geq f$). The load step that resolves this violation is the one which is just enough to bring the shear traction just to the limit of slip ($|\tau| = f$), i.e.

$$\frac{\delta L_\tau}{\delta L_0} = \frac{(|\tau_0| - \mu p_0)}{(|\tau_0| - \mu p_0) - (|\tau^*| - \mu p^*)} \quad (2.5)$$

2.3.2.4 Violation in Slip Constraints

Violation in a slip constraint occurs when a node that nominally slips in one direction, is slipping in the opposite direction, or has stopped slipping. If it were known, the rate of change in the lateral displacement speed would be used to find the δL which was just enough to change the node state, but because of the quasi-static nature of the constitutive model and the algorithm, this information is unavailable. Instead, if a violation of the slipping state occurs in the load step δL_0 , that load step is repeatedly bisected to find a smaller interval in which resides the δL that is just enough to cause that violation. It occasionally happens – such on a load reversal – that more than one sliding node becomes stuck at the same time. On such occasions, all of those sliding nodes that have a direction reversal are set to stick.

2.3.3 Single-Node Illustrations of Computing δL

At this stage it is helpful to walk through the calculation of δL for an individual node for a couple of types of node status:

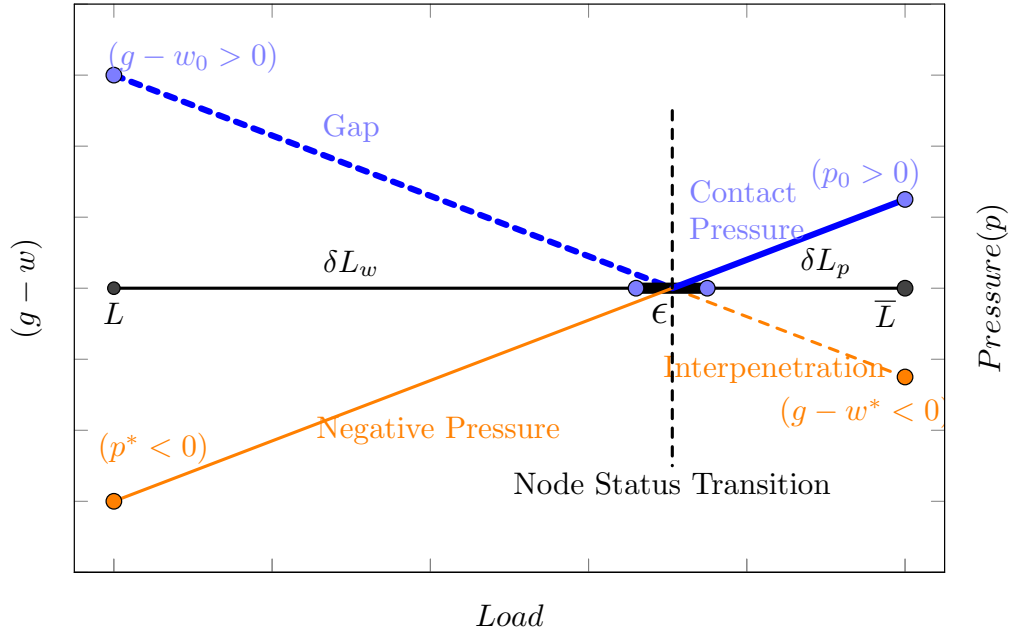


Figure 2.5: Single node illustration for contact and non-contact violations. The thick (blue) solid dashed lines represent admissible configurations and the thin (orange) solid and dashed lines represent inadmissible configurations. For instance if a node begins not-in-contact (thick dashed line on the left), as the load step δL increases, the gap closes linearly until contact occurs at δL_w , as the load further increases the gap stays at zero and the contact pressure increases linearly (thick solid line on the right.)

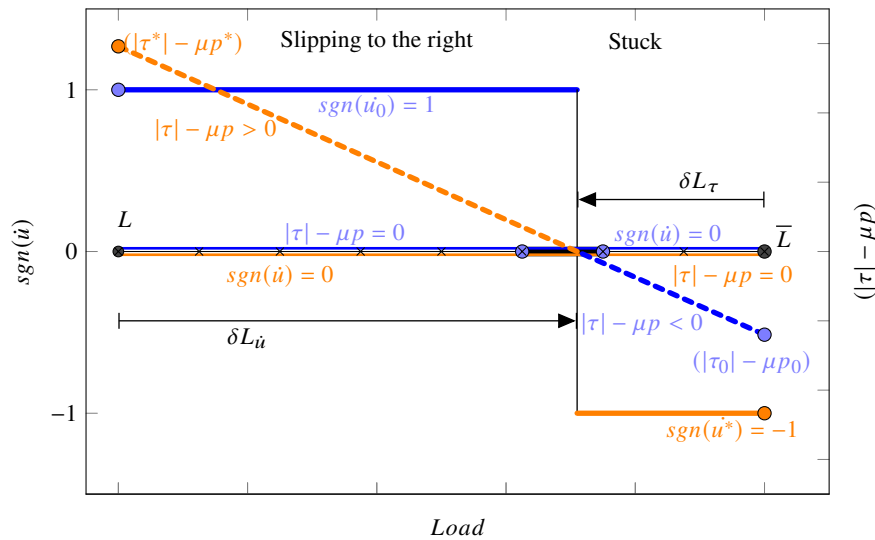


Figure 2.6: Single node illustration for stick and slip violations. The dark (blue) solid and thick lines represent admissible configurations and the lighter (orange) solid and dashed lines represent inadmissible configurations. For an initially stuck node (dashed thick (blue) line), calculation of shear traction exploits linearity of that traction to obtain the new δL_τ of stick violation. For an initially slipping node (solid thick (blue) line), calculation of change in $sgn(\dot{u})$ will require the method of bisection to obtain $\delta L_{\dot{u}}$ of slip violation.

1. Non-contact and Contact Problems:

In Fig 2.5, at load L a node has not-in-contact status but at load $\bar{L} = L + \delta L_0$, there would be interpenetration. Because of the linearity of the problem, we can calculate a load increment δL_w such that at load $L + \delta L_w$ the node just touches the surface ($w - g \approx 0$) with zero nodal traction ($p \approx 0$). At this point, the node status is switched from non-contact to being in contact. Note that at load $L + \delta L_w$, the nodal constraints associated with non-contact ($g - w \geq 0$) and with in-contact ($p \geq 0$) are satisfied simultaneously. On adding a node in contact, it can have three possible contact status stick, left slip, or right slip. There are two possible approaches to identify the contact status.

- First stick status is assigned to the new contact node. Then, the elasticity matrix is solved with a tiny load step. Then, calculated shear traction is used to decide the direction of the slip. After deciding the contact status, the elasticity matrix is solved again with a nominal load step.
- A slip status is assigned to the new contact node, where slip direction is assigned based on the previous motion of the node. For example, if a non-contacting node moves toward the left, then on coming into the contact, its contact status would be contact left slip.

Both approaches provide the same solution. We have used the second approach which is a little quicker than the first one.

Conversely, if the load is initially \bar{L} , where there is contact and the value of load is reduced to L , there would be a pressure violation ($p < 0$) at L , so an incremental load of δL_p (negative) is found so that at $\bar{L} + \delta L_p$, $p = 0$ and $w - g = 0$. Again, this is a state where the constraints of both the status at the beginning of the load step and the status that holds just after that load step are satisfied. Also, note that even though these are linear calculations, the values of load at which node status transition takes will not be exactly identical in the two calculations

discussed above, there will be some numerical error, and computational tests against zero must accommodate that numerical uncertainty.

2. Sticking and Slipping Problems:

If initially the load L corresponds to a node sliding in one direction (which we choose as positive for the sake of discussion), constraints being

$$\tau = -\mu p \quad \text{and} \quad \text{sgn}(\dot{u}) = 1$$

and then the load is changed to \bar{L} corresponding to

$$\tau = \mu p \quad \text{and} \quad \text{sgn}(\dot{u}) = -1$$

then \dot{u} must go through zero for some $L^* = L + \delta L_{\dot{u}}$ for some $\delta L_{\dot{u}}$. At that load, causing the velocity to be approximately zero, the node becomes stuck and the node status must be changed appropriately (See Fig. 2.6.) Since the constraint on $\text{sgn}(\dot{u})$ is nonlinear, there is no linear equation to solve for $\delta L_{\dot{u}}$; instead $\delta L_{\dot{u}}$ must be found through a method of bisections. When that load is found, the constraints holding at the previous step ($\dot{u} \geq 0$ and $|\tau| = \mu p$) as well as the constraints for the new state ($\dot{u} = 0$ and $|\tau| \leq \mu p$) are satisfied simultaneously.

If initially under load \bar{L} on the body, a node is stuck, with that node status the nodal constraints are $\dot{u} = 0$ and $|\tau| \leq \mu p$. Say that the load is changed to L and at that load, Eq. 2.2 yields $|\tau| > \mu p$, violating a constraint of the previous node status (for the sake of discussion, let us assume that $\tau > 0$). There exists a load $\bar{L} - \delta L_{\tau}$ between L and \bar{L} at which $|\tau| = \mu p$ (see Fig. 2.6). From Equation 2.2 where the constraints are those of the initial node status, the change in node traction changes linearly with change in applied load. We obtain a linear equation for δL_{τ} (Eq. 2.5) satisfying $|\tau| = \mu p$. Note that at load $\bar{L} - \delta L_{\tau}$, the stick conditions ($\dot{u} = 0$ and $|\tau| \leq \mu p$) are satisfied as are the slip conditions at inception of slip ($\dot{u} \geq 0$ and $|\tau| = \mu p$).

The algorithms discussed here are not fixed to particular mesh construction techniques such as finite element method, boundary integral method, or compliance matrix method. They work with almost all discretization techniques if contact surface nodes should follow the proper equality and inequality constraints from Eq. 2.1.

CHAPTER 3

VERIFICATION OF CONTACT ALGORITHMS

The coupled and complex nature of contact problems makes them difficult to solve analytically and usually requires simplifying assumptions – most often the Goodman decoupling approximation [31] – to reduce the complexity of the problem. In this chapter, we implemented and compared algorithms of the previous chapter with available analytical results; imposing the Goodman approximation in those problems where it is invoked in the corresponding analytic solution. The contact length, stick ratio, normal pressure, and lateral traction distributions are the most natural choices for comparing numerical and analytical solutions for a rigid cylindrical indenter pressing against an elastic half-plane. The closed-form expressions invoked here can be found in [6, 35]. We also compared the numerical solutions using both algorithms and explained the significant improvements through multiple examples.

3.1 Frictionless Normal Contact

3.1.1 Rigid Cylinder Pressed against an Elastic Half-plane

For the case of two identical elastic cylinders pressing against each other, we have analytic expressions for the length of the contact patch and pressure distribution [6] which can be mapped onto the problem of a rigid cylinder pressing against a frictionless elastic half-plane:

$$a = \sqrt{\frac{P(\kappa + 1)R}{2\pi G}}, \quad (3.1)$$

$$p(x) = \frac{2P\sqrt{a^2 - x^2}}{\pi a^2} \quad (3.2)$$

where $2a$ is the contact length, P is the total normal force, R is the radius of the rigid cylinder, G is the shear modulus of the half-plane, $\kappa = 3 - 4\nu$ (for plane strain), and ν is the Poisson's ratio. In the calculations that follow, $G = 1$ and $\nu = 0.3$, $R = 0.25$, and $P = 0.015$ are used. The contact length

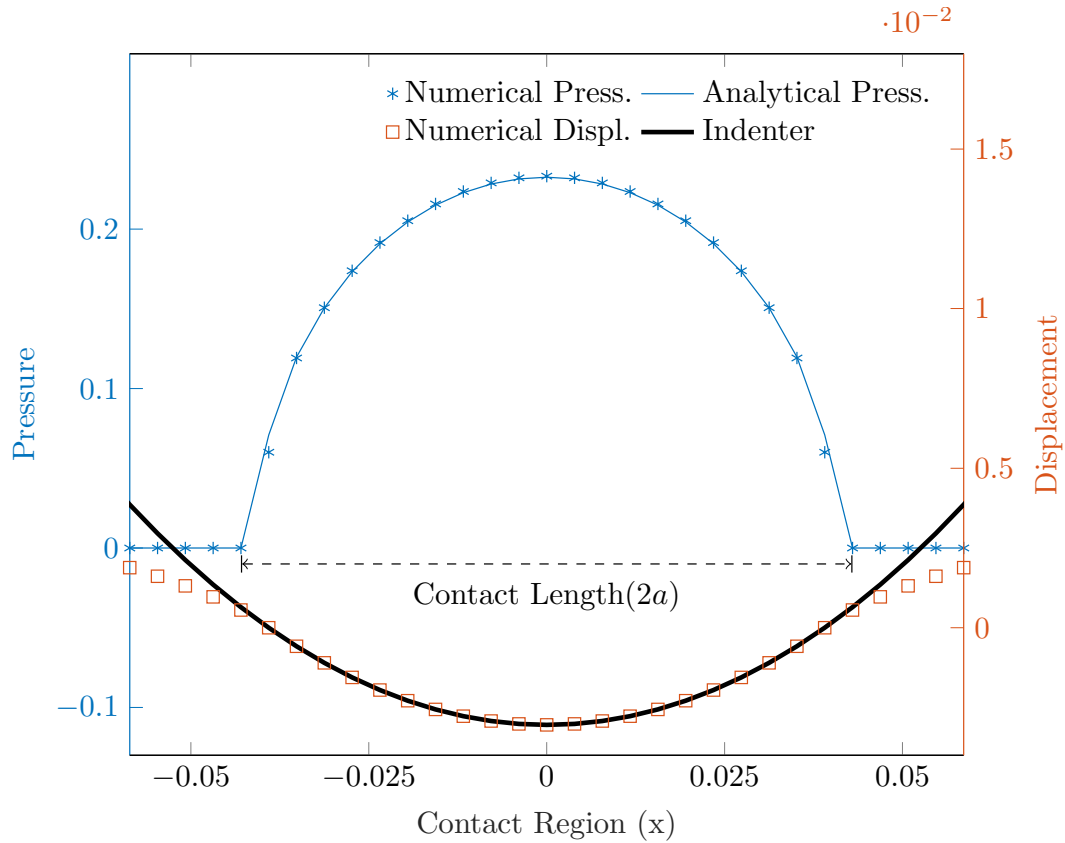


Figure 3.1: Verifying the half-plane compliance matrix formulation with the analytical solution. The two numerical algorithms yielded identical solutions. The * and \square represent numerically calculated traction at the centers of intervals. The continuous curves are analytic

(with 21 nodes in-contact) calculated using Eq. 3.1 is used for calculating the pressure distribution using Eq. 3.2. Figure 3.1 shows the numerical pressure distribution calculated from the compliance formulation, which matches almost identically with analytical results for a given total normal force (P).

3.1.2 Rigid Flat Indenter Pressed against an Elastic Half-plane

Furthermore, another analytical solution is available for a rigid flat indenter pressing against the elastic half-plane. In this case, the contact length between the indenter and half-plane remains unchanged and is equal to the rigid indenter's length. The pressure distribution for a normal force

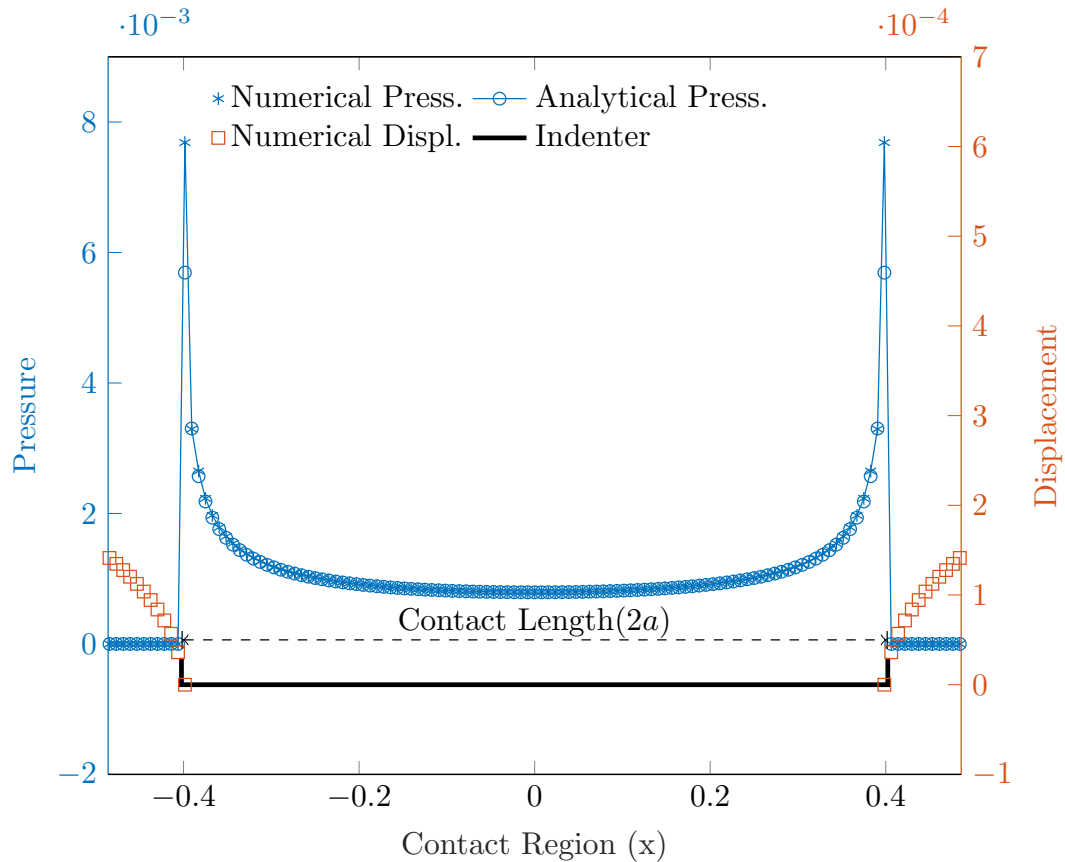


Figure 3.2: Verifying the half-plane compliance matrix formulation with the analytical solution. The two numerical algorithms yielded identical solutions. The * and □ represent numerically calculated traction at the centers of intervals. The continuous curves are analytic

P is shown in the Eq. 3.3.

$$p(x) = \frac{P}{\pi\sqrt{a^2 - x^2}}. \quad (3.3)$$

The numerical expression for pressure distribution is calculated using the same material properties of elastic half-plane with normal force $P = 0.001$. The contact region has 103 nodes in-contact for the contact length of 0.8, equivalent to the length of the flat rigid punch. Figure 3.2 compares the analytical and numerical pressure distributions for the rigid flat indenter, which are the same in most of the contact region. There are minor discrepancies at both endpoints due to the singular nature of the pressure distribution at the ends for the flat rigid indenter.

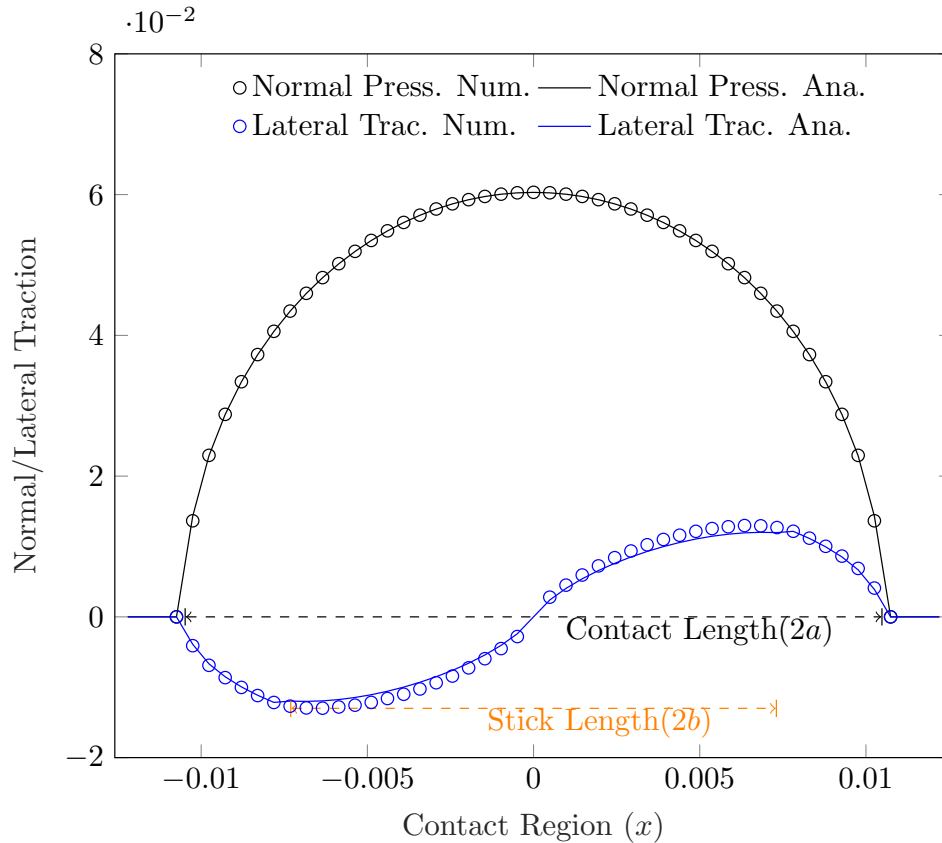


Figure 3.3: Verifying numerical normal and lateral traction distribution with analytical expression for rigid cylinder pressing against an elastic half-plane with coefficient of friction ($\mu_s = 0.3$).

3.2 Normal Contact with the Coulomb Friction

Next, the simplest friction model, Coulomb friction, is employed with contact algorithm-II. The rigid cylinder is pressed against an elastic half-plane with normal force ($P = 0.001$), friction coefficient ($\mu_s = 0.3$), and contact problem has same material and geometric properties from previous section 3.1. Figure 3.3 shows the normal and lateral traction distribution due to the normal pressing of the cylinder. Lateral traction is anti-symmetric with respect to the center of the contact and divides the contact length($2a$) into following three regions;

1. slipping to the left at the left end of the contact.
2. stick region with length ($2b$) in the center.
3. slipping to the right at the right end of the contact.

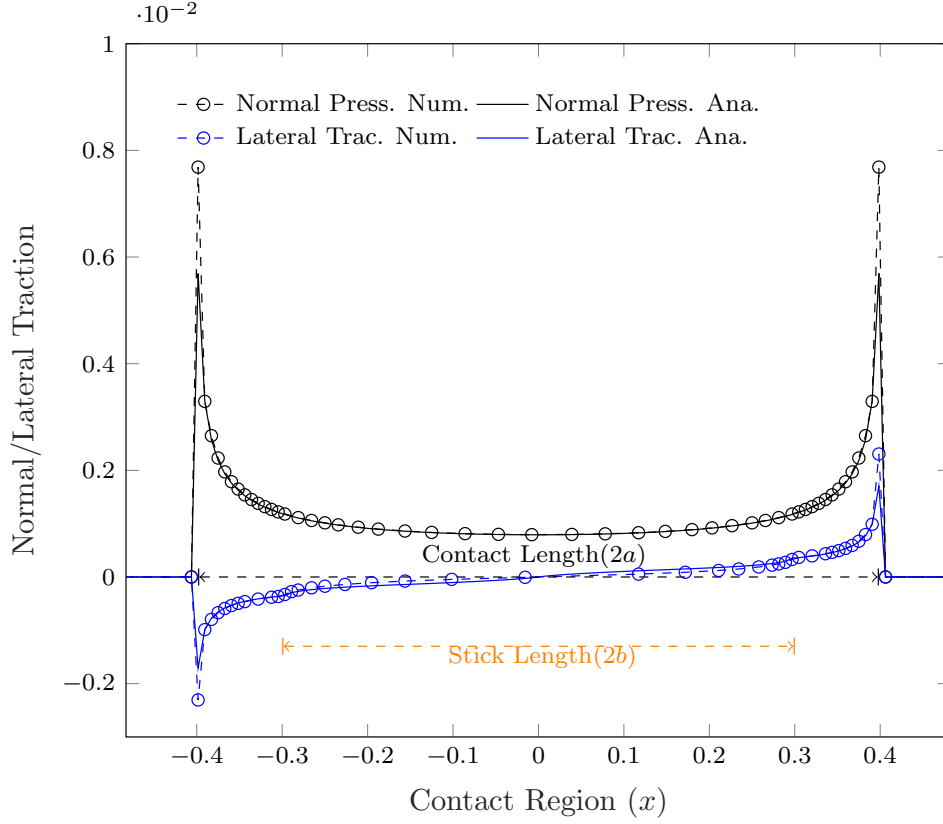


Figure 3.4: Verifying numerical normal and lateral traction distribution with analytical expression for rigid flat indenter pressing against an elastic half-plane with coefficient of friction ($\mu_s = 0.3$).

Figure 3.4 shows similar characteristics such as anti-symmetric lateral traction and stick-slip region for the rigid flat indenter.

3.2.1 Comparison with Spence (1973) Stick Ratio Results

The stick ratio is one of the relevant contact parameters for the comparison and verification during the frictional contact. Spence [63] derived analytical solutions for a rigid indenters normally pressed against a rough elastic half-planes. Relying on the Goodman approximation, he developed the expression for the stick ratio as shown in Eq. (3.4).

$$\beta K(c) = \mu K'(c) \quad (3.4)$$

where β is the Dundur's parameter ($\beta = (1 - 2\nu)/(2 - 2\nu)$)[26], ν is the Possion's ratio, $c = b/a$ is the stick ratio, $K(c)$ is the complete elliptic integral of the first kind and $K'(c) = K(\sqrt{1 - c^2})$.

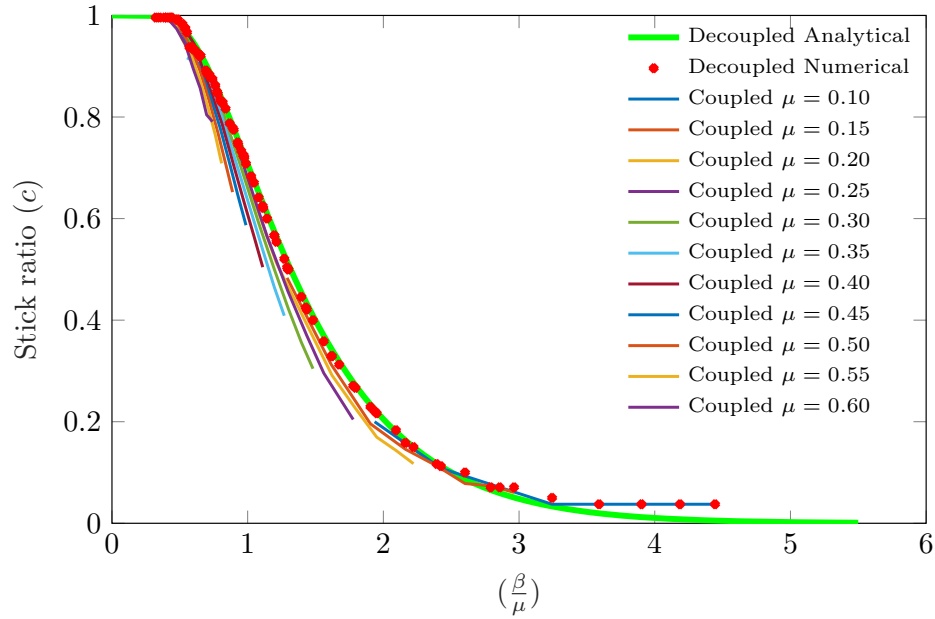


Figure 3.5: Stick ratio for cylindrical indenter with and without decoupling assumption

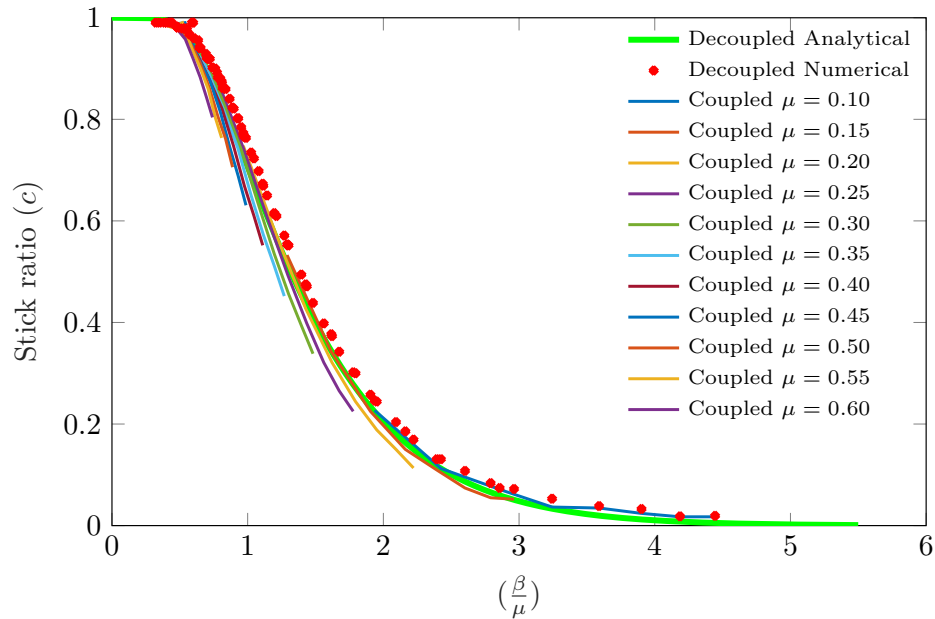


Figure 3.6: Stick ratio for flat indenter with and without decoupling assumption

Remarkably, this relationship holds for both flat and round indenters.

Figures. 3.5 and 3.6 show that numerical results obtained by setting $C_{w\tau} = 0$ are in good agreement with the analytical results for both cylindrical and flat indenters. At a higher value of β/μ , there is a little discrepancy between analytical and numerical results due to discretization in

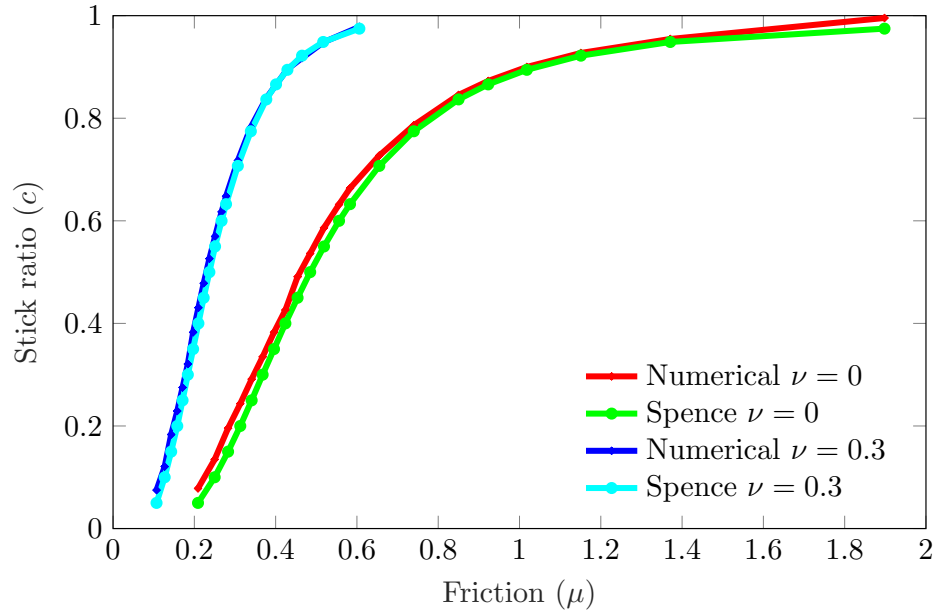


Figure 3.7: Stick ratio vs friction with full elastic coupling for cylindrical indenter

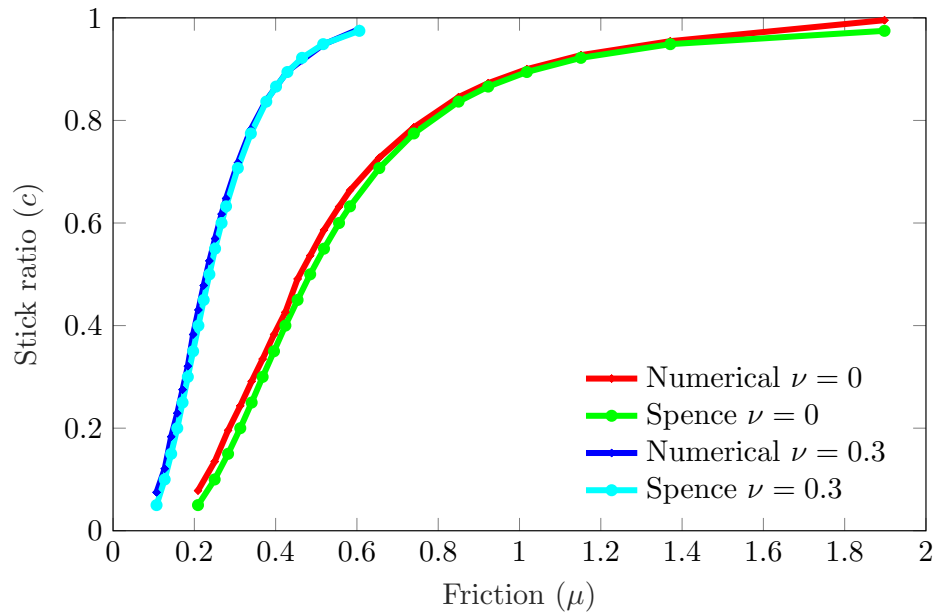


Figure 3.8: Stick ratio vs friction with full elastic coupling for flat indenter

the contact region. If stick length is less than the discretization length, then the discretization length is taken as the stick length resulting in a higher value of slip ratio. Also shown in these figures are contact algorithm results where the Goodman approximation was not performed. The predictions of the coupled calculations lie slightly below those associated with the uncoupled system.

Spence [63] further solved cases of coupled systems for rigid indenters pressing against rough elastic half-planes. He solved the system of coupled integral equations numerically. Figures 3.7 and 3.8 show stick-slip ratios for both Spence's numerical results and those of the contact algorithm. For the case of the cylindrical indenter, the agreement between the predictions of the contact algorithm and the analytic results are again extremely good. In the case of a flat punch, the contact solutions predict slightly higher stick ratios, but the discrepancy is likely due to the singularity of the tractions at the edges of the indenter, and it is difficult to get accurate solutions.

3.2.2 Verification of Numerical Lateral Traction with an Analytical Expression

Using Spence's [63] results for stick ratio, an analytical expression (Eq. 3.5) was developed [35] for the lateral traction distribution for frictional cylindrical contact. Using a similar approach, an analytical expression (Eq. 3.6) for the lateral traction distribution for the frictional contact of the rigid flat indenter was developed.

$$q_{cyl}(x) = \begin{cases} \frac{2\mu P}{(\pi a)K(c)} \left[\sqrt{1 - (x/a)^2} \Psi(\phi, c) - \frac{x}{2b} \ln \left\{ \frac{b - \sqrt{b^2 - x^2}}{b + \sqrt{b^2 - x^2}} \right\} \right] \operatorname{sgn}(\beta x) & |x| \leq b \\ \frac{2\mu P}{(\pi a)} \left(\sqrt{1 - (x/a)^2} \right) \operatorname{sgn}(\beta x) & b \leq |x| \leq a \end{cases} \quad (3.5)$$

$$q_{flat}(x) = \begin{cases} \frac{\mu P}{(\pi a)K(c)} \left[\frac{1}{\sqrt{1 - (x/a)^2}} \Psi(\phi, c) - \frac{x}{2b} \ln \left\{ \frac{b - \sqrt{b^2 - x^2}}{b + \sqrt{b^2 - x^2}} \right\} \right] \operatorname{sgn}(\beta x) & |x| \leq b \\ \frac{\mu P}{(\pi a)} \left(\frac{1}{\sqrt{1 - (x/a)^2}} \right) \operatorname{sgn}(\beta x) & b \leq |x| \leq a \end{cases} \quad (3.6)$$

where $\sin(\phi) = x/b$ and $\Psi(\phi, c)$ is an incomplete integral of the first kind, and $K(c)$ is the complete integral of first kind.

Figures 3.3 and 3.4 show that the lateral traction distribution calculated numerically are in line with analytical expression for both cylinder indenter and flat indenter contact.

3.2.3 Verification of Stick-Ratio in the Mindlin Problem.

The frictionless Hertz problem is equivalent to pressing two identical rough cylinders against each other. In that case, the full contact path results in stick status. Next, if the cylinders are each subject to equal and opposite lateral forces, then the slip will occur on the contact patch's outer edges. This

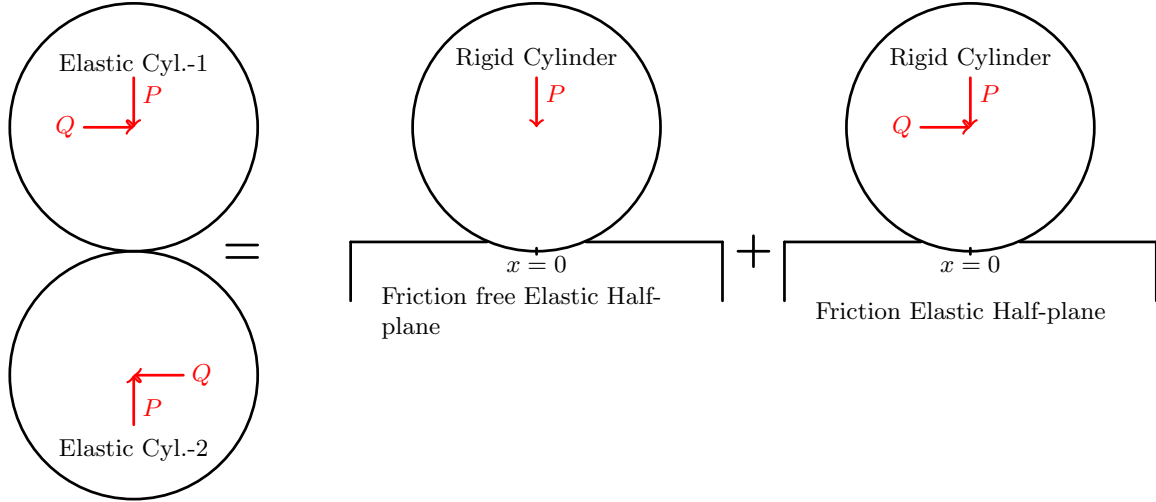


Figure 3.9: Mapping of two elastic cylinder contact to the rigid cylinder over the half-plane

contact problem – Mindlin Problem [52] – can be solved with use of the Goodman decoupling approximations (see Fig. ??). Analytical equations for stick-slip ratio (c) vs lateral tractions ($q(x)$) are shown in Eqn. (3.7) and (3.8) [56].

$$c = \sqrt{1 - \frac{Q}{\mu P}} = \frac{b}{a} \quad (3.7)$$

$$q(x) = \frac{\mu(2P)}{\pi a} \left[\sqrt{1 - \frac{x^2}{a^2}} - c \sqrt{1 - \frac{b^2}{a^2}} \right] \quad \text{For } |x| < b \quad (3.8)$$

$$q(x) = \frac{\mu(2P)}{\pi a} \sqrt{1 - \frac{x^2}{a^2}} \quad \text{For } b \leq |x| \leq a$$

The above two-cylinder Mindlin problem can be mapped to a similar problem of a rigid cylindrical indenter pressed against an elastic half-plane (see Fig. ??) in the following manner:

- In the absence of friction, the indenter is pressed against with force P over an elastic half-plane.
- Friction is turned on, but by construction, there is no shear traction on the interface, and there is no slip.
- A lateral force Q is introduced to the indenter.

(See Eqs. from 2.20 to 2.33 of ref [35] for the mapping). Also, this strategy of turning friction on and off in a calculation has a precedent [15].

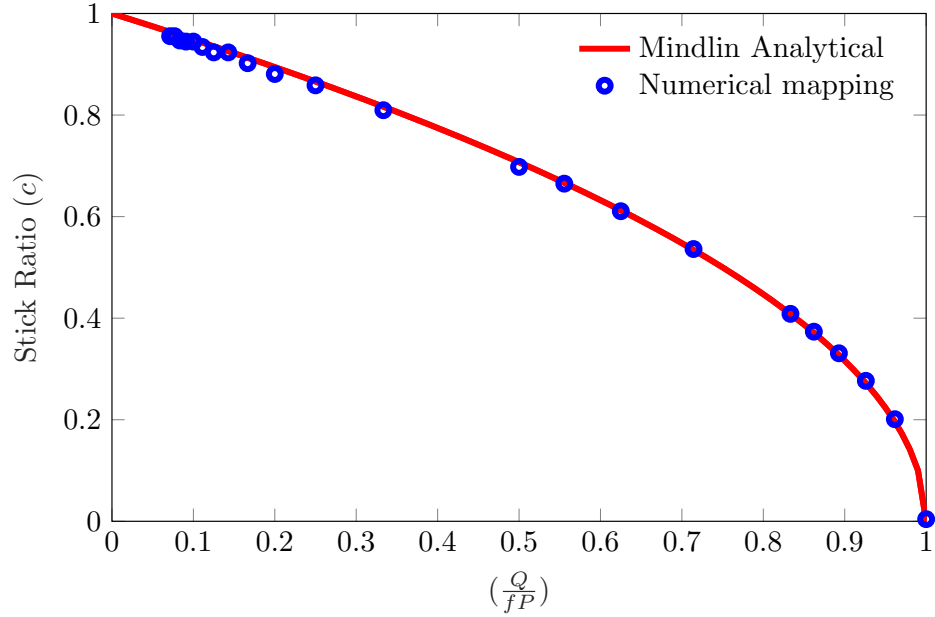


Figure 3.10: Verifying numerical stick ratio with analytical expression for Mindlin solution.

As the force Q is increased, slipping on each edge of the contact path will evolve. When the contact algorithm is employed with Goodman decoupling approximation ($C_{uw} = 0$), the resulting predicted stick-slip ratios are in good agreement with those of the Mindlin solution (see fig. 3.10).

3.3 Coulomb Friction Model in Mindlin Problem

We implemented the Coulomb friction model (μ_s) with both contact algorithms. We used the well-known Mindlin solution for comparison. Note the Mindlin solution is employing Goodman decoupling approximation. The mapping of the Mindlin problem to the rigid cylinder over an elastic half-plane is shown in section 5.

In the following analysis, the geometric and material properties of the problem from Section 3.1 are used again (radius of cylinder $R = 0.25$, shear modulus $G=1$, and Poisson's ratio $\nu = 0.3$). The elastic half-plane is more finely discretized in this problem than the previous, and 87 nodes are found to be in-contact with the normal load ($P = 0.001$). This finer mesh was chosen to obtain an adequate resolution of the stick-slip boundary and the shear stress at that boundary for comparison with the analytic solutions. The lateral load is set at $Q = 2.8 \times 10^{-4}$.

Figure 3.11 compares the normal pressure and lateral traction distributions of the analytic

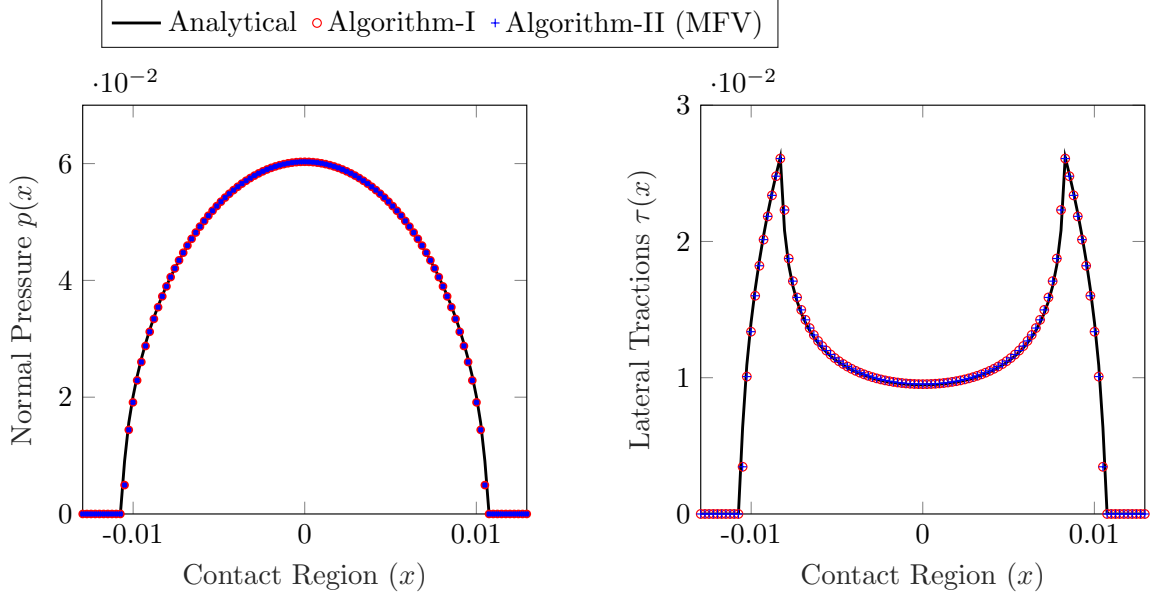


Figure 3.11: Comparing numerical tractions from Algorithm-I, Algorithm-II, and analytical expression for one-parameter friction model ($\mu = 0.7$) after application of lateral force: normal pressure distribution (left) and lateral traction distribution (right)

expression and of the two numerical algorithms. All three seem to be in line with each other for a one-parameter Coulomb friction model with friction coefficient $\mu = 0.7$. For the problem with these parameters, we are well within the limit calculated by Klarbring for existence and uniqueness of a single node (or rigid body) contact.

Both Algorithm-I and Algorithm-II are verified with the given analytical expressions. These verification established that the numerical results using the contact algorithms are in-line with the analytical results. In the upcoming sections, we illustrated the issues with Algorithm-I and improvements due to Algorithm-II.

3.4 Two-parameter Coulomb Friction Model in Mindlin Problem

Next, We demonstrate the robustness of the Method of First Violation (Algorithm-II) on a more complicated friction model – the two-parameter friction model – involving a coefficient of static friction, μ_s , and a coefficient of kinetic friction, μ_k . In this numerical problem $\mu_s = 0.7$, $\mu_k = 0.42$, but the loading sequence and geometry of the previous problem are employed again. For the sake of consistency, the Goodman decoupling approximation is used in this analysis as well. Figure 3.12

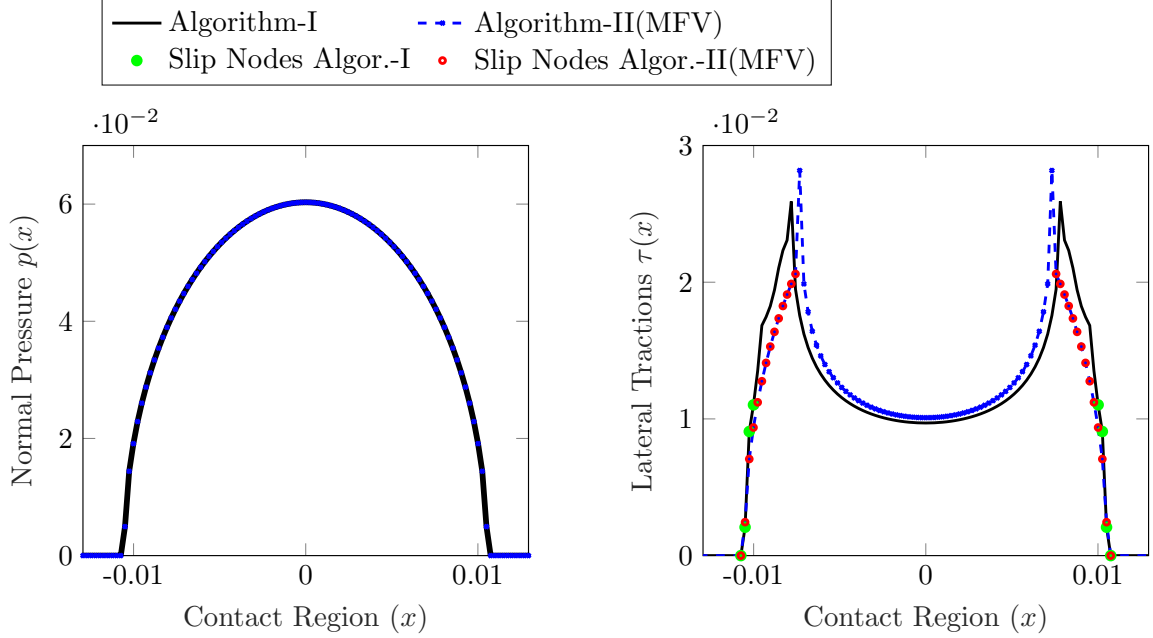


Figure 3.12: Comparing numerical tractions from Algorithm-I and Algorithm-II for two-parameter friction model ($\mu_s = 0.7$, $\mu_k = 0.42$) after application of lateral force: normal pressure distribution (left) and lateral traction distribution (right). For Algorithm-I, the region of stick is indicated by a solid black line, and the region of slip is indicated by a black line connecting solid green circles (\bullet). For Algorithm-II, the region of stick is indicated by a dashed blue line, and the region of slip is indicated by a dashed blue line connecting red dots (\bullet).

shows the normal pressure and lateral traction predictions of the two algorithms. (An analytical expression is not available in the literature). As expected, the two algorithms yield identical normal traction fields. However, there are serious discrepancies between the lateral tractions predicted by the two algorithms. Algorithm-II (MFV) predicts a smooth and symmetric distribution of shear traction with a clear separation between stick and slip boundaries (Fig. 3.12b). Algorithm-I shows a much wider stick region than does Algorithm-II. Most significantly, the stick region is not smooth; this is an artifact of nodes fluctuating back and forth between stick and slip status in the iterative process. In contrast, Algorithm-II assures that all constraints are satisfied at the beginning and end of each load step, and all points in between. It should be noted that in order to get convergence of Algorithm-I in this problem, it is necessary to set all nodes to stuck status after each load increment and then to release nodes according to how much they violate the constraining inequality ($\tau \leq \mu_s p$).

The above example demonstrates a situation where the more conventional contact algorithm

(Algorithm I) has difficulty converging to a unique solution; the two-parameter friction model is notorious for causing convergence problems [44]. Yet the Method of First Violation appears to address this problem with little difficulty.

A major source of interest in elastic frictional contact is predicting and understanding the contact mechanics associated with cyclic loading. Some preliminary results with the cyclic loading are presented in the later this chapter.

3.5 High-Coefficient of Friction with Full Elastic Coupling

We implemented both algorithms with a high coefficient of friction ($\mu_s = 3.0$) and a full elastic coupling. In this instance, the rigid cylinder is first pressed against a frictional elastic half-plane with normal load ($P = 10^{-3}$), and later pressed with a lateral load ($Q = 2 \times 10^{-4}$). The geometric and material properties of the rigid cylinder and elastic half-plane remain unchanged.

The Klarbring's results [45] apply to bodies in contact at a single point. His formula is suggestive that higher coefficients of friction might cause issues of existence, uniqueness, and numerical stability to manifest even in problems of distributed contact. Consequently, one should not be surprised that distributed contact problems become more challenging as the coefficient of friction increases.

Figure 3.13 shows that the lateral traction distribution predicted by Algorithm-I jumps alternately between positive and negative from node to node in the slip region and is irregular in stick region. Also, the discontinuous direction of friction in the slip regions obscures the boundary between stick and slip regions. Because of the full elastic coupling of this calculation, the jumps in lateral traction also influence the normal pressure, which also oscillates from node to node in the vicinity of the slip region. On the other hand, the lateral traction distribution predicted using Algorithm-II is smooth with a proper boundary between the slip and the stick regions. It should be pointed out that Algorithm-I often fails to converge for high values of friction coefficient and very fine meshes, yet this does not seem to be an issue with Algorithm-II.

A quick exploration of mesh convergence using Algorithm-II is summarized in Figure 3.14. In

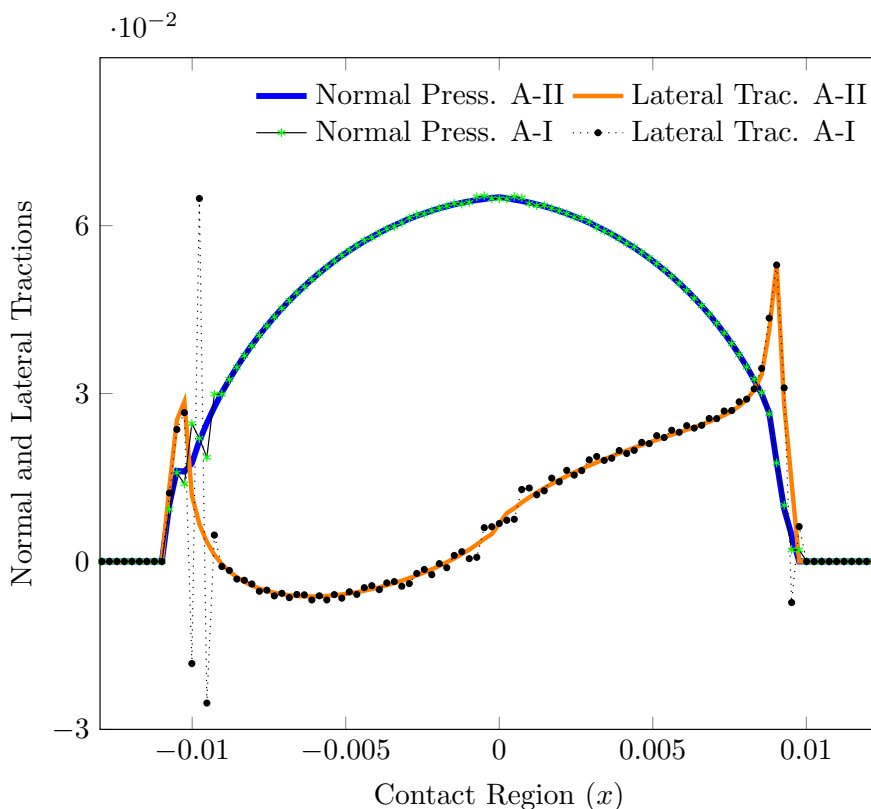


Figure 3.13: Normal and lateral traction distribution after a normal and lateral pressing of the cylinder against an elastic half-plane with coefficient of friction $\mu_s = 3$. Comparing the Algorithm-I and Algorithm-II with 85 contact nodes in both cases.

the figure, the Algorithm-II calculations of 3.13 are re-plotted and labeled as FM, corresponding to the fine mesh of 85 nodes in the contact patch. Also shown in that figure are the predictions of Algorithm-II when a coarser mesh (CM) having only 42 nodes is employed. The two sets of traction predictions align closely except near the edges of the slip zones, where the coarse mesh is incapable of capturing fine detail. Though not definitive, this calculation is at least consistent with mesh convergence of Algorithm-II. Of course, the finer meshes will be associated with smaller load steps to reach the first violations.

3.6 Implementation of Dahl Friction Model

The Method of First Violation (Algorithm-II) was also tested on a problem involving the Dahl friction model [24]. The Dahl model is a rate-independent, quasi-static continuous slip model,

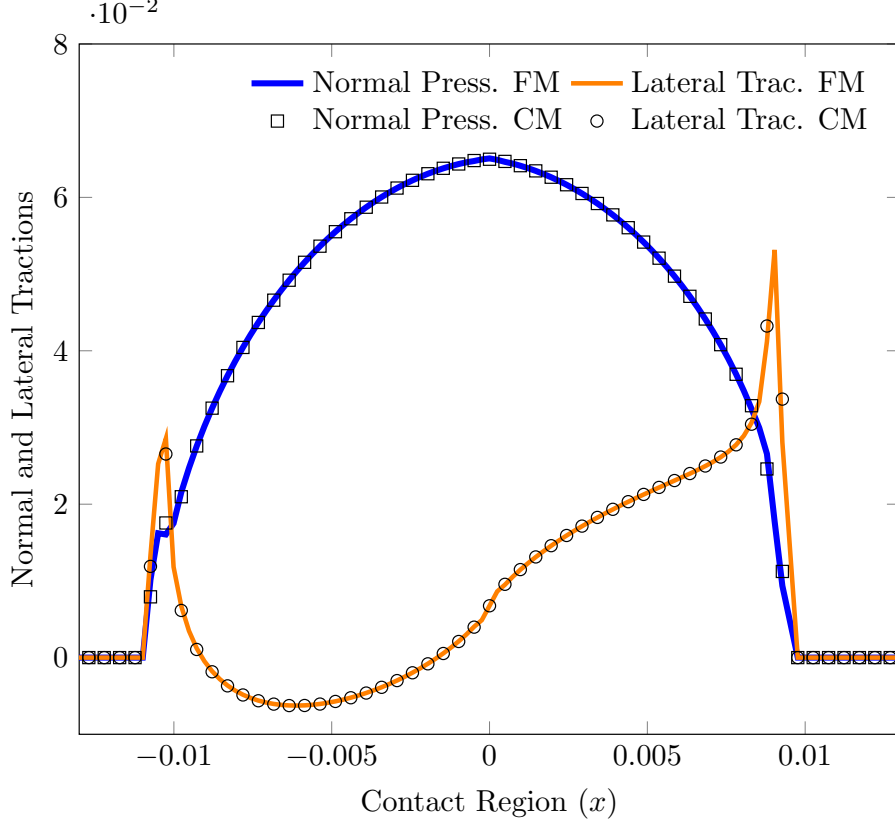


Figure 3.14: Normal and lateral traction distribution after a normal and lateral pressing of the cylinder against an elastic half-plane with $\mu_s = 3$. Comparing the tractions predicted by Algorithm-II using a fine mesh (FM) having 85 nodes in the contact patch and those predicted by Algorithm-II using a coarse mesh (CM) having only 42 nodes in the contact patch.

based on an idea of bristle stiffness (Eq. 3.9).

$$\frac{df}{du} = \sigma \left| 1 - \frac{f}{f_c} \operatorname{sgn}(\dot{u}) \right|^\gamma \operatorname{sgn} \left(1 - \frac{f}{f_c} \operatorname{sgn}(\dot{u}) \right) \quad (3.9)$$

where, f , f_c , and u are the friction force, maximum/cut-off friction force and the lateral displacement of contacting node respectively. σ and γ are the contact stiffness and exponents (Dahl parameters), respectively. In this model, lateral displacement of a node changes even while the friction force is less than cut-off friction ($f \leq f_c$) - unlike Coulomb friction. But, as friction force reaches the maximum force (f_c) the Dahl model behaves similar to Coulomb friction at macro-slip. This similarity with Coulomb friction is exploited in the numerical implementation of this friction model, which is briefly explained in the appendix B.

A contact problem is considered where the rigid indenter of the previous illustrations is pressed

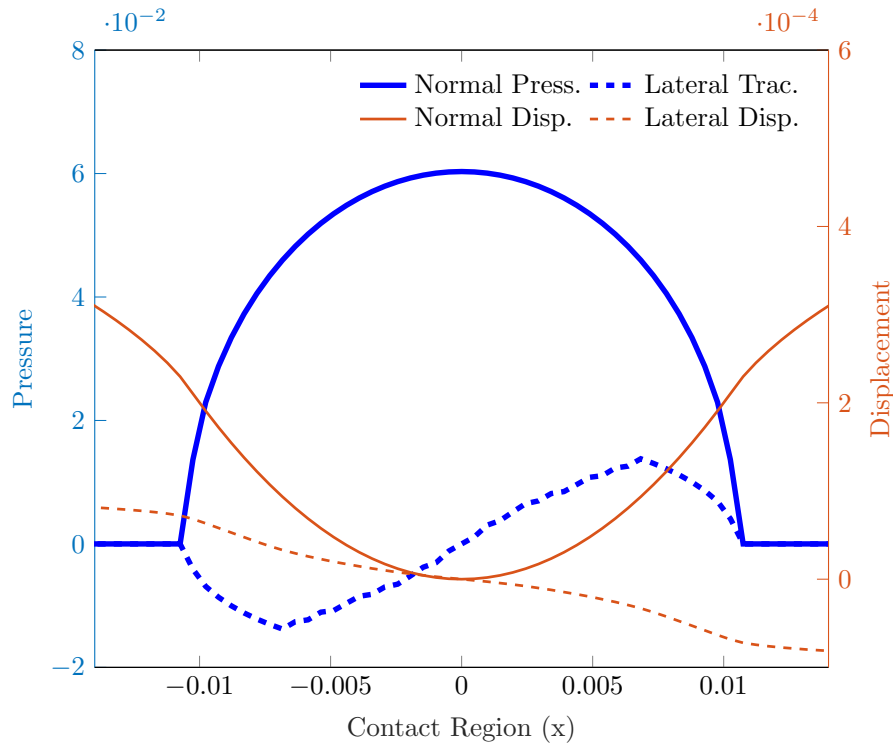


Figure 3.15: Implementing of the Method of First Violation algorithm with the Dahl friction model: ($\sigma = 1000$, $\gamma = 1$, $\mu_s = 0.3$). Algorithm-I would not converge to a solution for Dahl friction model.

with a normal force ($P = 0.001$) against an elastic half-plane where the frictional interface is represented by a Dahl model having parameters $\sigma = 1000$ and $\gamma = 1$, and the geometric and material properties are those of the from the previous problems. The maximum friction force at each node is ($f_{c_n} = \mu p_n$) with $\mu = 0.3$. Figure 3.15 shows the predicted normal and lateral traction and displacement distributions when the MFV algorithm is employed. Those predicted tractions and displacements are smooth with clear boundaries between stick and slip regions. This demonstrates that the MFV algorithm can provide stable results in problems beyond Coulomb friction. The authors attempted to apply Algorithm-I to this problems, but could not obtain a convergent solution.

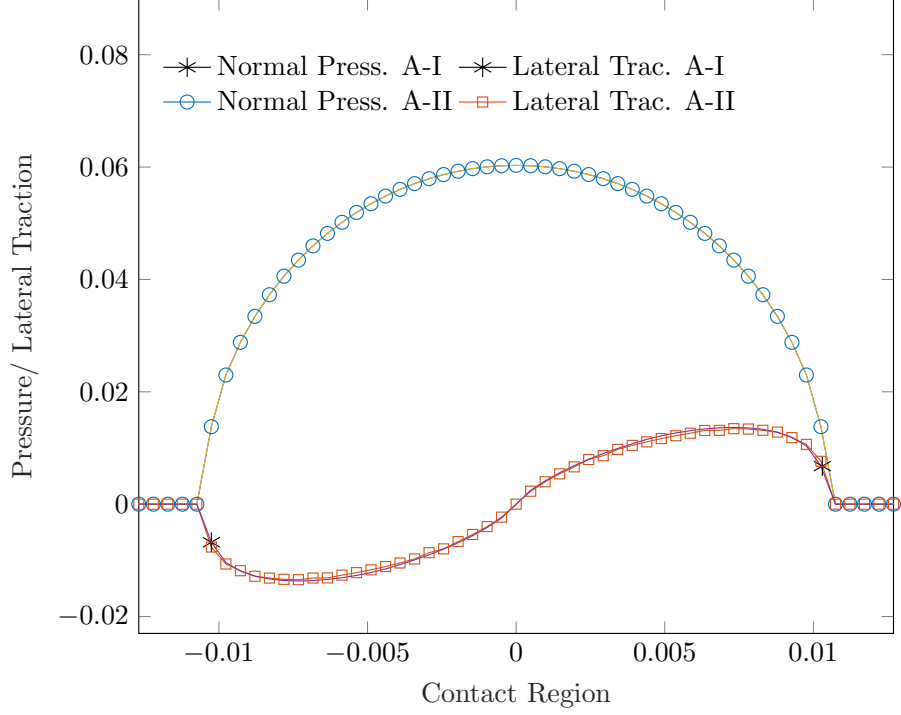


Figure 3.16: Normal and lateral traction distribution calculated for two-parameter friction ($\mu_s = 0.7$, $\mu_k = 0.49$) through Algorithm-I and Algorithm-II after a rigid cylinder is pressed against an elastic half-plane with a normal force ($P = 0.001$).

3.7 Two-parameter Coulomb Friction for a Cylinder Pressed against an Elastic Half-plane

A two-parameter Coulomb friction model is used between the indenter and the half-plane with static coefficient $\mu_s = 0.7$ and dynamic coefficient $\mu_k = 0.49$. To be able to compare numerical results with analytic ones, the Goodman decoupling approximation [31] is imposed by setting $C_{up} = 0$.

Initially, the rigid cylinder is pressed against the elastic half-plane with a normal force $P = 0.001$, bringing 43 nodes in the contact region. This results in symmetric normal pressure distribution and anti-symmetric lateral traction between two surfaces. In this case, the predictions calculated through Algorithm-I and Algorithm-II are identical, both shown on the left-hand side of Figure 3.16. Because of the imposition of the Goodman decoupling approximation, the normal pressure field is independent of the shear tractions and identical to the analytical expression, provided by Mindlin [52, 56]. There is no analytical expression available for lateral traction distribution for two-parameter Coulomb friction models.

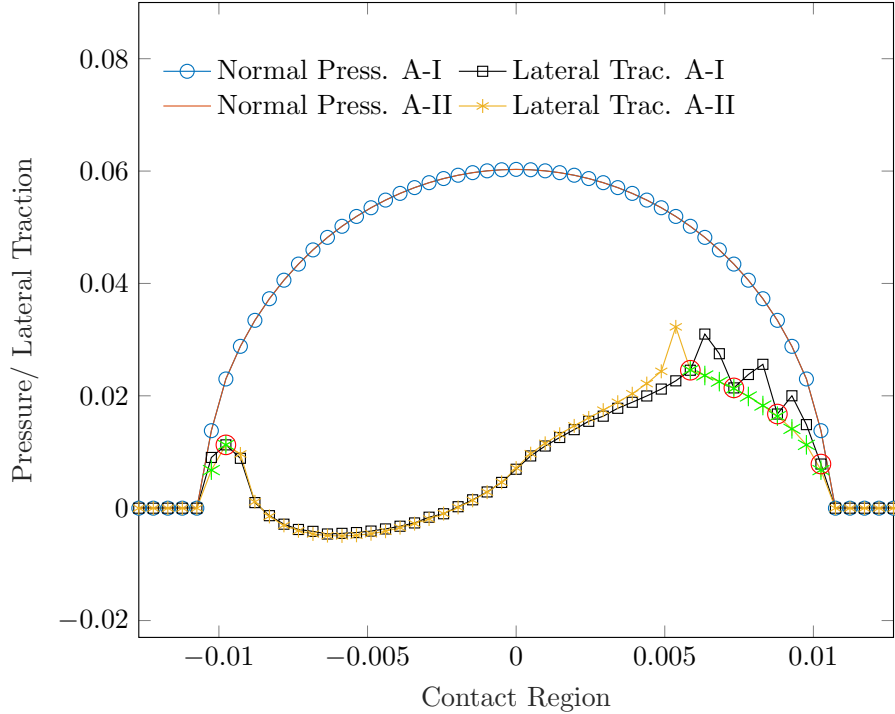


Figure 3.17: Normal and lateral traction distribution calculated for two-parameter friction ($\mu_s = 0.7$, $\mu_k = 0.49$) through Algorithm-I and Algorithm-II after a rigid cylinder is pressed against an elastic half-plane with a normal and lateral forces ($P = 0.001$, $Q = 0.000185$). Slipping nodes are represented through 'red o' and 'Green *' for A-I and A-II respectively.

Next, a lateral load of $Q = 0.000185$ is applied gradually on the indenter in the x-direction. The plot on the right-hand side of Fig 3.17 shows the normal and lateral traction distribution as calculated by Algorithms I and II. The normal pressure distribution remains unchanged because of Goodman's decoupling approximation; however, the lateral traction distributions calculated by the two methods show a fair difference. It is worth noting that the right-hand side of the shear traction field predicted by Algorithm-I follows a similar pattern to that predicted with Algorithm-II but shows significant spatial oscillation between stick and slip states. This is an indication of a failure of the algorithm to converge to a valid solution. Algorithm-II shows a proper separation between the stick and the slip regions. Both Algorithms involve small load increments, both are converged to the same loads, and the sums of the lateral tractions are also equal. Because the stress and displacement fields evolve from those of the previous load step, this small discrepancy can grow into large error as the load also evolves.

3.7.1 Cyclic Shear Loading with Two-Parameter Coulomb Friction

Having provided evidence that this formulation using the method of first violation appears to provide a proper solution with the two-parameter Coulomb friction, it seems reasonable to explore the path dependence of traction fields during cyclic loading [16].

We consider the same configuration as before (see 3.7), impose a vertical compressive load of $P = 0.001$, and then apply a cyclic lateral loading with amplitude $Q_{\max} = 0.000185$. The resulting lateral traction fields at multiple steps in the process are shown in Fig. 3.18. The following discussion is with reference to that figure.

Sub-figure(1) has the same traction distribution as of Fig. 3.17: that which exists immediately after the imposition of the vertical load. As soon as a rightward lateral load is applied, the left side node that had been slipping leftward switches to being stuck. Sub-figure(2) with lateral load $0.3 Q_{\max}$ shows a continuous slipping region on the right resulting from the rightward load adding to the initially rightward tractions from the previous load step.

Sub-figure(3) with lateral load $0.7 Q_{\max}$ shows a growth in the slipping region on the right and the beginning of slip on the left, where the rightward load has become sufficient to overcome the initial leftward traction and to bring that node into sliding to the right. Sub-figure(4) with lateral load Q_{\max} shows further growth in slipping regions on both ends. There is a clear separation between sticking and slipping regions. This traction distribution provides a pattern for the residual stresses in cyclic loading that we see below.

Sub-figure (5) shows the traction distribution just after the change in the direction of lateral load. All the nodes that had been slipping towards the right, now suddenly stick because the traction at each point has been reduced from that necessary for slip to just below that. These nodes remain stuck in sub-figure(6); the reduced load is again accommodated by a redistribution of traction among the stuck nodes without any actual sliding. In sub-figure (7), we see that as the applied load continues to decrease, the residual stress due to previous rightward sliding requires two nodes to start slipping leftward to maintain the force balance. Sub-figures (8) and (9) are in the same state and repeated to preserve periodicity. There is zero lateral load, but again some node must go into

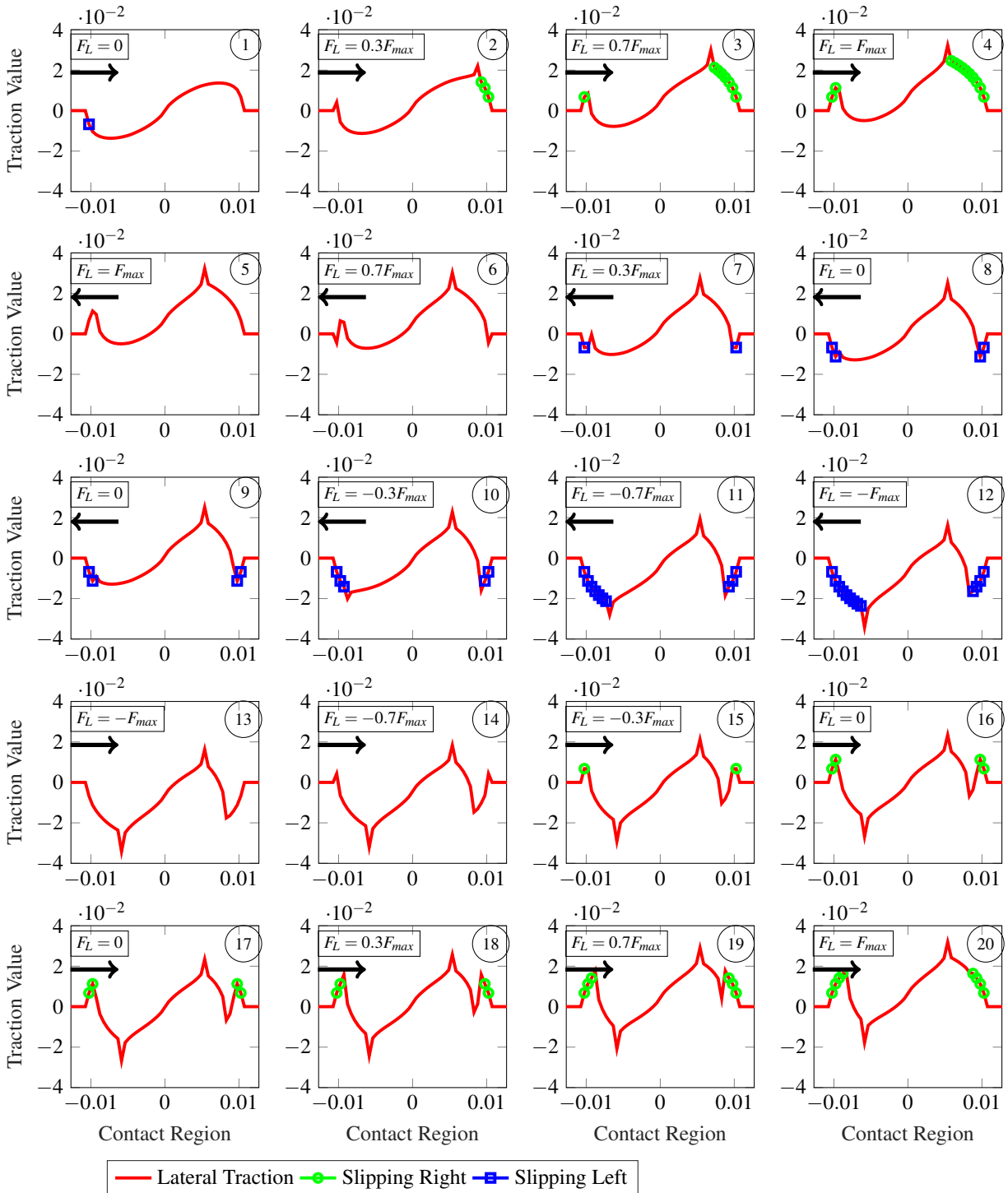


Figure 3.18: Evolution of lateral traction with lateral cyclic loading (Arrow shows the direction of lateral loading.) All tractions shown are physical traction normalized by G . [16]

slip in order for the integrated traction to be zero. Sub-figures (10), (11), and (12) show that the increase in load leftward increases the extent of the slip regions. Sub-figure (12) with lateral load $-Q_{\max}$ shows a new negative peak of traction, which separates the stick and slip regions. The region between these two peaks will remain stuck throughout the cycling process.

The traction fields of sub-figures 13-20 show the similar pattern of evolution as discussed for sub-figures 1-12, but the important observation is that steady-state has been reached by sub-figure 20: sub-figures 12 and 20 are right-left/up-down reflections of each other.

These traction fields illustrated in Fig. 3.18 provide an insight on how the traction distribution evolves, how slip zones form, grow, and disappear, and generally how each traction field unfolds from that of the previous load. This logical progression argues that the correct path dependence has been adequately captured by the "Method of First Violation" algorithm.

3.8 Algorithm Computational Efficiency

The relative efficiencies of the two algorithmic approaches is explored on our paradigm problem. A rigid cylinder is pressed normally over the elastic half-plane (same geometry and material properties from section 3.1) with normal load ($P = 0.004$) and friction ($\mu = 0.3$) for multiple load steps (δL_0). The efficiency of algorithms can be compared by counting the number (N_{ite}) of linear solves of Eq. 2.2, the most time-consuming part of the procedure. Figure 3.19 shows that the number of iterations using Algorithm-1 reduces with an increase in load step and that the number of iterations increases with an increase in contact nodes (mesh density). Though the increasing load step results in a faster solution, eventually the converged solution manifests visible anomalies. Red marks in Fig. 3.19 indicate non-physical solutions due to the attempt to resolve multiple contact violations associated with large load steps(δL_0). The optimal load step for this algorithm would appear to be a bit smaller than those which cause visible anomalies in the solution; this is suggested by the dashed blue line.

Figure 3.20 shows a concave up relation between the number of iterations on increasing the load step using Algorithm-II(MFV). On each curve in Fig. 3.20, all points represent an identical

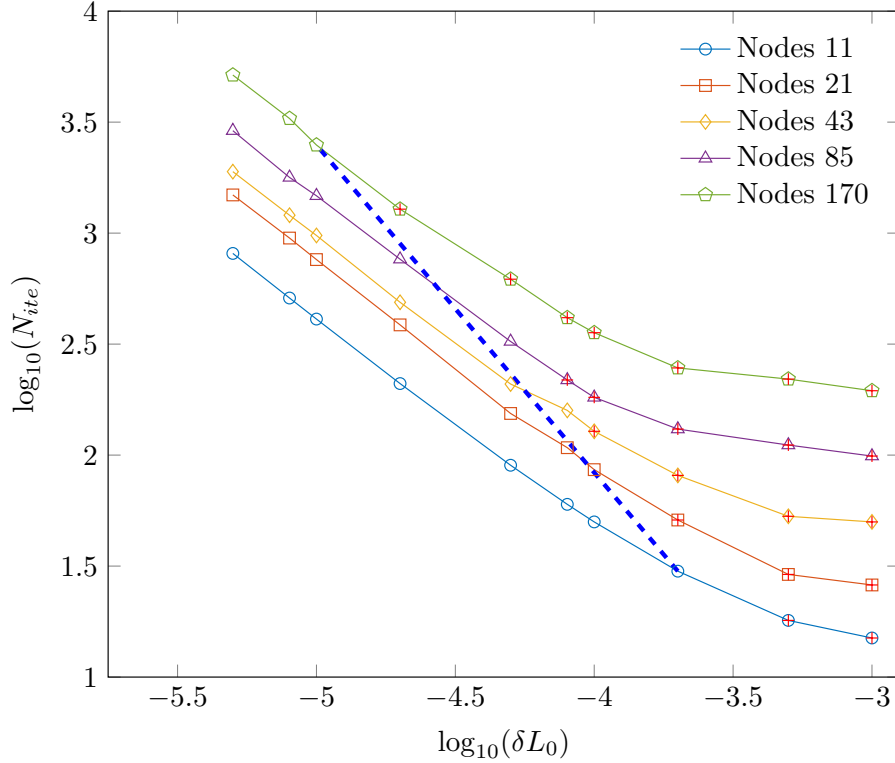


Figure 3.19: Number of iterations (N_{ite}) vs load-step (δL_0) using Algorithm-I for coarse to fine contact mesh (red marks shows the bad converged solution). Optimal load increments for this method on this problem are suggested by the dashed blue curve.

solution; the choice of nominal load step impacts only the compute time to achieve that solution. These solutions capture the same load history and are admissible solutions throughout that history. The black star in each curve in Fig. 3.20, indicates the optimal load step size for maximum efficiency (faster convergence). The blue curve of optimal load increments associated with Figure 3.19 is reproduced in Figure 3.20 showing that both methods have about the same optimal load steps and the compute times when those optimal load steps are employed.

3.9 Summary of the Algorithm Verification and Comparison

The contact algorithm - Method of First Violation (MFV) - based on the principle of first contact status violation is presented and its predictions are compared to those of a more conventional algorithm and with analytic expressions when available. The important role of contact history is emphasized and the capability of the MFV to capture and to accommodate that history dependence

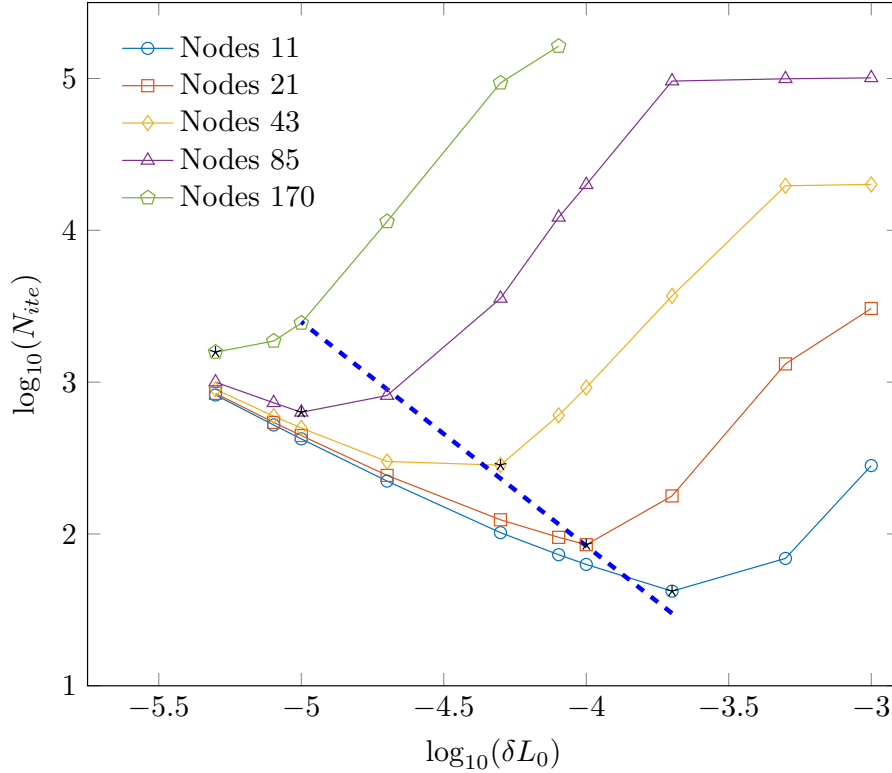


Figure 3.20: Number of iterations (N_{ite}) vs load-step (δL_0) using Algorithm-II(MFV) for coarse to fine contact mesh (Black marks shows the optimal load-step for faster and accurate solution). The blue dashed line is copied from Figure 3.19.

is discussed. The fidelity to load-displacement history derives from this algorithm providing node states that are consistent with all contact constraints at the beginning and end of every load step as well as all points in between.

The MFV algorithm predictions compared well with analytic solutions where they were available and also well with the predictions of a conventional algorithm when then that conventional algorithm provided numerically stable results.

The robustness of the Method of First Violation was also tested on three categories of contact problem know to be numerically challenging

1. A contact problem involving two-parameter friction. Here the MFV provided robust and physically plausible solutions while the conventional algorithm anomalies at the stick-slip interfaces.

2. A contact problem of Coulomb but with full coupling and a high coefficient of friction. The analogy with Klarbring's results for single point contact would suggest numerical difficulties for problems of coupled contact of elastic bodies with high coefficient of friction. Indeed the conventional algorithm resulted in very discontinuous shear tractions in the vicinity of the slip zone and corresponding jaggedness in the normal traction. The predictions of the MFV shows none of these difficulties.
3. The MFV was applied to contact involving an entirely different form of contact model, the Dahl equation. Here the MFV again performs robustly and makes plausible predictions of traction and displacement fields, though there do not appear to be alternate estimates to compare to. The authors were unable to get the conventional algorithm to converge on this problem.
4. The MFV is shown to be stable when used with the two-parameter friction model and to provide a reasonable evolution of the traction fields from each load step to the next.
5. In the problems studied, when the Method of First Violation is used with optimal nominal load steps, its efficiency is comparable to that of the conventional algorithm.

PART II

An Extremely Fine Mesh Strategy Using Compliance Matrices

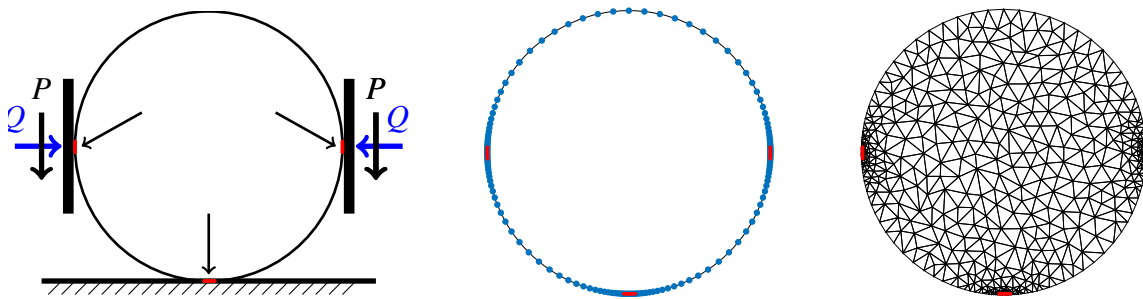
CHAPTER 4

COMPLIANCE FORMULATION FOR AN ELASTIC DISK AND FOR A HOLE IN AN INFINITE ELASTIC PLANE

The fundamental mechanics of contact problems is often elusive because of the intrinsic experimental difficulties (the physics takes place exactly where it cannot be seen). This intrinsic experimental difficulty is matched by similarly difficult computational impediments [37, 51] that requires a very fine mesh near the contacting interfaces. The finite element method is the most general approach to create very fine mesh/discretization on the interfaces. However, with a large number of the nodes on the interface also creates many more nodes inside the body, which means more degrees of freedom to solve with a big stiffness matrix, making the contact problem hard to analyze. The reduction methods are fairly common to reduce the stiffness matrix to only contacting nodes, but they are challenging due to the required inversion of the big matrix.

4.1 Computational Issues

The scope of the problem to be addressed is suggested in Figure 4.1. On the left is a problem of multiple contacts on an elastic disk; there are shear and normal tractions applied at the contact patches. It is only in the regions of the three contact patches that tractions and displacements are



(a) Contact problem expected to have 33 nodes in contact among the three contact regions.

(b) Boundary mesh of the disk with 147 nodes on the boundary.

(c) A coarse finite element mesh with 1903 nodes inside the elastic disk

Figure 4.1: A contact problem with normal (P) and lateral (Q) forces are applied pressing an elastic disk against a rigid surface with 33 boundary nodes in contact (11 nodes in each 4^{th} contact region).

essential to the problem in the sense that if the tractions in the contact patch were known, that would be sufficient to calculate stresses and displacements throughout the body.

The figure in the center is a surface discretization such as could be used for a boundary integral element [9] analysis of the problem; note that extraordinarily fine meshes are required in the regions of contact in order to have enough nodes to solve the contact problem with any fidelity. A gradual mesh transition away from contact reduces the number of degrees of freedom of the corresponding numerical problem. However, the surface mesh must be fine enough overall to achieve accuracy [68, 34, 70]. One would like to have several tens of nodes over each contact patch. Contact patches are usually substantially less than 2° of the osculating circle; for visibility, the surface mesh shown in Fig. 4.1b has 11 nodes over each contact patch of 4° and the mesh transition is relatively aggressive (15%). In reality, one would expect each contact patch to be on the order of 1° of the radius for the stresses to remain below yield, to have on the order of 50 – 200 nodes per contact patch to obtain a reasonable resolution of the traction field, and several thousand nodes around the surface. Further, the nature of the boundary element method is such that the corresponding matrices are dense (not sparse), and the systems of equations that must be solved at each iteration of the contact algorithm becomes onerous. One can use the analytic expressions [35, 57] for deformation of frictionless contact for a cylinder pressed against a rigid surface (or of two identical cylinders pressed against each other) to evaluate the width of the contact patch and the maximum von Mises stress, each as functions of geometry, elastic constants, and net compression load. Table 4.1 provides the contact angle achieved just as the peak stress within the cylinder reaches yield stress for each of six common metals. Note that most of the metals exceed their elastic limit within a degree of contact arc. In the case of friction and applied lateral loads, the contact angles would be yet smaller. To understand the interface physics and to have a conclusive test model, extremely fine discretizations are needed for each contact region.

The right-most mesh (Fig. 4.1c) is such as might be used for a finite element calculation, though for visibility the surface mesh is the same as the crude mesh of the center figure and the mesh transition away from the surface is also aggressive. Even so, there are approximately 1903

Metals	Elasticity's Modulus (GPa)	Yield Strength (MPa)	Poisson's Ratio	Contact arc angle (von-Mises)
Copper	117	70	0.36	0.223 ^o
Brass	102	117	0.35	0.428 ^o
Mild Steel ASTM 302	200	250	0.3	0.467 ^o
Aluminum	69	95	0.33	0.514 ^o
Stainless Steel AISI 302	180	502	0.3	1.041 ^o
Titanium	105	730	0.34	2.595 ^o

Table 4.1: Maximum contact arc for compressing an elastic disk onto a flat rigid surface above which the disk material exceeds its elastic limit.

nodes in the system shown in Fig. 4.1c. In an actual contact problem, one would expect to have to employ several tens of thousands of nodes. The corresponding equations – though banded – are still formidable and must be solved, either directly or indirectly, with the help of a static condensation, with each iteration of the contact algorithm. In general, solving contact problems with high resolution often becomes intractable.

A strategy that can mitigate the difficulty of computational contact analysis greatly is to pose the problem using compliance matrices. For the sake of discussion, consider a frictionless contact problem such that each node has one normal displacement, one tangential displacement, and potentially one normal pressure. Because the problem is frictionless, it is only the normal displacement (w_k) and normal pressure (p_k) that are necessary to address elastic contact. The usual finite element formulation where elasticity is expressed in terms of a stiffness matrix appears as:

$$\begin{Bmatrix} p_1 \\ p_2 \\ \vdots \\ p_N \end{Bmatrix} = [K] \begin{Bmatrix} w_1 \\ w_2 \\ \vdots \\ w_N \end{Bmatrix} \quad (4.1)$$

In this formulation, as the tractions change on just a few nodes in contact, the whole large system of equations must be solved. If we can formulate the elasticity in terms of a compliance matrix:

$$\begin{pmatrix} w_1 \\ w_2 \\ \vdots \\ w_N \end{pmatrix} = [C] \begin{pmatrix} p_1 \\ p_2 \\ \vdots \\ p_N \end{pmatrix} \quad (4.2)$$

then we observe that all the nodes not in contact are subject to zero pressure, and we can dispense with all the columns in C corresponding to those nodes. Further, the displacements outside the contact regions are not necessary to solve the contact problem, so the corresponding rows of C can also be deleted. The resulting system can be orders of magnitude smaller than the original.

A compliance representation of the elasticity is highly favorable to a solution of contact problems, but it does not naturally come out of boundary integral methods or stiffness-based finite element implementations. In fact, there are only a few shapes that lend themselves to a compliance formulation. One is the an elastic half-plane [35, 72]. A compliance formulation for the surface of a disk or for a hole in an elastic plane is developed in the body of this chapter.

Though the methods discussed below are restricted to narrow categories of two-dimensional geometries, they should provide the foundation for a computational test-bed sufficient to address some of the outstanding questions on interface mechanics, such as the significance of different frictional constitutive models in resulting contact stress distributions or elastic coupling between shear and normal displacement in conformal and non-conformal contact.

4.2 2D-Cylinder Airy Stress Function (Michell Solution)

The Michell solution is an expansion of the Airy stress function in polar coordinates and is often used in studying the elasticity of two-dimensional circular bodies [6, 56, 62].

$$\begin{aligned}
 \Phi_0(r, \theta) = & A_{01}r^2 + A_{02}r^2 \ln(r) + A_{03} \ln(r) + A_{04}\theta \\
 & + \left(A_{11}r^3 + A_{12}r \ln(r) + A_{14}r^{-1} \right) \cos \theta + A_{13}r\theta \sin \theta \\
 & + \left(B_{11}r^3 + B_{12}r \ln(r) + B_{14}r^{-1} \right) \sin \theta + B_{13}r\theta \cos \theta \\
 & + \sum_{n=2}^{\infty} \left(A_{n1}r^{n+2} + A_{n2}r^{-n+2} + A_{n3}r^n + A_{n4}r^{-n} \right) \cos(n\theta) \\
 & + \sum_{n=2}^{\infty} \left(B_{n1}r^{n+2} + B_{n2}r^{-n+2} + B_{n3}r^n + B_{n4}r^{-n} \right) \sin(n\theta)
 \end{aligned} \tag{4.3}$$

where the A_{mn} and B_{mn} are unknown coefficients. By definition, an Airy stress function satisfies the biharmonic equation ($\nabla^4 \Phi_0 = 0$), and indeed every term of the Michell expansion does so. The stress and displacement fields associated with an Airy stress function can all be expressed in terms of partial derivatives of Φ , and those fields for the Michell expansion have been tabulated in many texts, but are combined in Appendix Table ?? and E.2 in consistent notation for the convenience of the reader.

The Michell expansion has been used to find analytic expressions for traction and displacement distributions for many problems involving two-dimensional elastic disks or holes in an infinite elastic plane. The following is used in a somewhat different manner; it will be used to discretize the surfaces of disks or holes and to obtain a very efficient compliance formulation for elastic, frictional contact analysis.

Which terms in Equation 4.3 are actually employed depends on the geometry of the problem. Terms that generate non-integrable singular stress fields as $r \rightarrow 0$ are not used in problems involving a solid disk. Terms associated with stress fields that grow without bound as $r \rightarrow \infty$ are not used in problems involving unbounded boundaries. Some terms generate multi-valued displacement fields (secular terms not periodic in θ), and these must be combined to yield displacement fields that are periodic in θ .

4.2.1 General Discretization Strategy

A set of evenly spaced nodes are defined on the free surface(s) of the body of interest. This may be a very fine mesh because only the nodes in the vicinity of contact will contribute to the size of the numeric problem to be solved. A compliance matrix associated with that mesh is constructed using the strategy indicated Fig. 4.2.

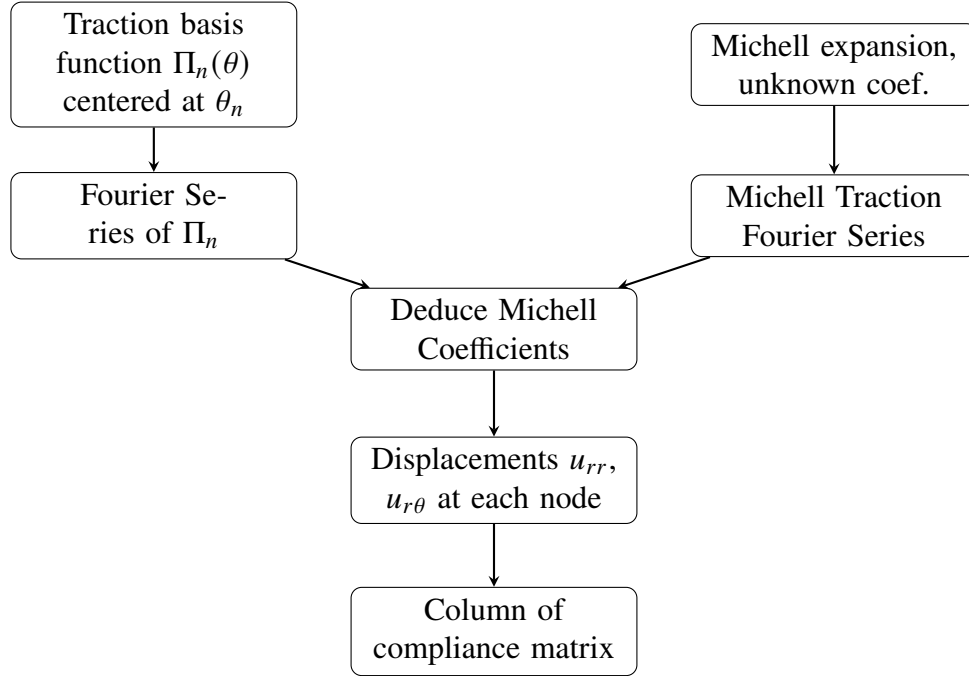


Figure 4.2: Flow chart using Michell expansion to create a compliance matrix.

The strategy of exploiting the Michell expansion to construct a compliance matrix is outlined in Figure 4.2.

1. A set of $2N$ basis functions Π_n for traction (one for each of radial traction and shear traction at each node) on the surface(s) of the region of interest is defined. This set of basis functions must be a partition of unity, have only local support, and must achieve their maximum amplitude at their associated node. The simplest such functions are the rectangular or box function

$$\phi_n(x) = H(x - (x_n - \Delta x/2)) - H(x - (x_n + \Delta x/2)) \quad (4.4)$$

which has a value of 1.0 between $(x_n - \Delta x/2)$ and $(x_n + \Delta x/2)$ and is zero elsewhere and the chapeau function

$$C_n(x) = \phi_n(x) (x_n - |x|) / (\Delta x/2) \quad (4.5)$$

which has a triangular shape, taking the value of 1.0 at x_n , zero at $x_n \pm \Delta x/2$, and zero outside of $(x_n - \Delta x/2, x_n + \Delta x/2)$ [10]. These basis functions are each decomposed into their Fourier components.

2. The contributions of each term of the Michell expansion to surface tractions are all trigonometric functions. Coefficients of each trig function are grouped.
3. Matching terms of both Fourier series yields a linear system of simultaneous equations for coefficients of the Michell expansion. In the problems considered below, these equations can be decoupled.
4. Given the Michell expansion coefficients, the radial and tangential displacements on the surface are evaluated at every node.
5. These displacements become the n^{th} column of the compliance matrix.

4.2.2 A Solid Elastic Disk

For an elastic disk with no holes (Fig. 4.3), all terms of the Michell expansion associated with non-integrable stress singularities at $r = 0$ are discarded ($\{A_{02}, A_{03}, A_{14}, B_{14}, A_{n2}, A_{n4}, B_{n2}, A_{n4}, A_{04}\} = 0$). Similarly, terms associated with multi-values of displacement should also be removed to provide a meaningful solution ($\{A_{12}, B_{12}, A_{13}, B_{13}\} = 0$). These restrictions result in a single valued displacement stress function expression with non-secular terms (Eq. 4.6) at each value of (r, θ) .

$$\begin{aligned} \Phi_0(r, \theta) = & A_{01}r^2 + A_{11}r^3 \cos(\theta) + B_{11}r^3 \sin(\theta) \\ & + \sum_{n=2}^{\infty} [(A_{n1}r^{n+2} + A_{n3}r^n) \cos(n\theta) + (B_{n1}r^{n+2} + B_{n3}r^n) \sin(n\theta)] \end{aligned} \quad (4.6)$$

The expression (4.6) is suitable for solid disks with no net forces or moments. When there are net forces and moments, some of the discarded terms can be brought in with the assurance that all singularities are integrable and that all displacements are single-valued.

The Φ_0 term $A_{04}\theta$ has stresses values as $\sigma_{rr} = 0, \sigma_{\theta\theta} = 0$ and, $\sigma_{r\theta} = 1/r^2$ (see the table ??). The $\sigma_{r\theta} = 1/r^2$ has a singularity at $r=0$, but this is an integrable singularity at the center of the disk, corresponding to a finite torque.

If one wishes to incorporate non-self equilibrating tractions to the boundary of a disk, one must balance them with some internal traction that will oppose the net forces and moments for the external distribution. Such terms are available from the Michell solution, but the cost is accommodating singularities at the center of the disk since our focus is on the surface of the disk, singularities in stress or displacement are acceptable.

The Φ_0 terms ($A_{12}r \ln(r) \cos(\theta)$, $A_{13}r\theta \sin(\theta)$, $B_{12}r \ln(r) \sin(\theta)$, and $B_{13}r\theta \cos(\theta)$) have multi-valued displacement terms and contain displacement elements that are proportional to θ . This issue can be resolved by taking linear combinations of these terms for which the multi-valued secular terms disappear (see Eq. 4.7).

$$A_{13} = -A_{12} \frac{\kappa + 1}{\kappa - 1} \quad \text{and} \quad B_{13} = B_{12} \frac{\kappa + 1}{\kappa - 1} \quad (4.7)$$

where, κ is a Kolosov's constant (Eq. 3.20 of [6]):

$$\kappa = \begin{cases} 3 - 4\nu & \text{for plane strain} \\ \frac{3 - \nu}{1 + \nu} & \text{for plane stress} \end{cases} \quad (4.8)$$

As these terms are non-secular now and represent the net forces and moments. The new stress function will be the following:

$$\begin{aligned} \Phi_0(r, \theta) = & A_{01}r^2 + A_{04}\theta \\ & + A_{11}r^3 \cos(\theta) + A_{12} \left[r \log(r) \cos(\theta) - \frac{\kappa + 1}{\kappa - 1} r\theta \sin(\theta) \right] \\ & + B_{11}r^3 \sin(\theta) + B_{12} \left[r \log(r) \sin(\theta) + \frac{\kappa + 1}{\kappa - 1} r\theta \cos(\theta) \right] \\ & + \sum_{n=2}^{\infty} \left[(A_{n1}r^{n+2} + A_{n3}r^n) \cos(n\theta) + (B_{n1}r^{n+2} + B_{n3}r^n) \sin(n\theta) \right] \end{aligned} \quad (4.9)$$

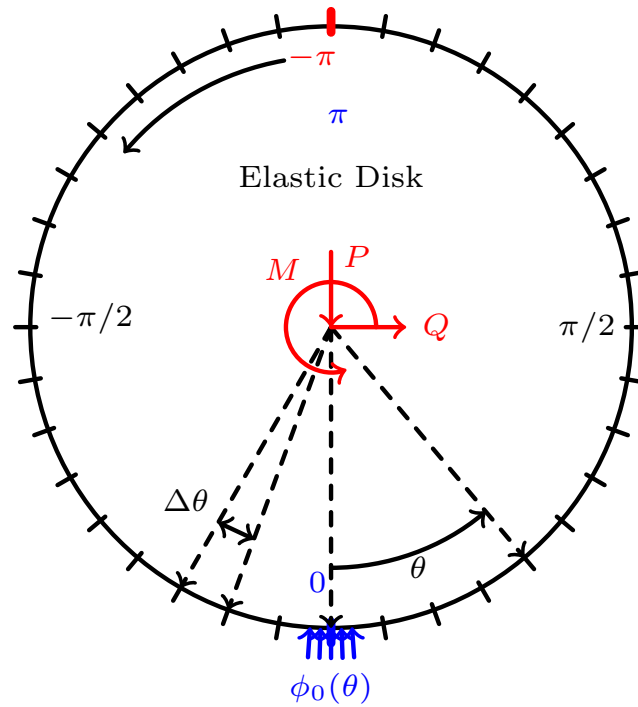


Figure 4.3: A solid disk with discretization from $-\pi$ to π

Stresses and displacements were calculated for the above stress function, which are shown in Appendix C.1.

4.2.2.1 Creating the Surface Displacement Field in an Elastic Disk

A very fine discretization is created on the elastic disk shown in Fig. 4.3 to formulate a numerical solution. The circular disk discretized into N intervals with the equal length of $\Delta\theta = 2\pi/N$ from $-\pi$ to π as shown in Fig. 4.3. Unit tractions (normal and then shear) are imposed, one at a time in each interval, and the corresponding displacement field is evaluated at nodes placed at the centers of that and of every other interval. For instance, unit pressure load $\phi_0(\theta)$ is applied radially on the disk at $\theta = 0$; taking a value of one in the region of $(-\Delta\theta/2, \Delta\theta/2)$, and zero in at any other region of $(-\pi, \pi)$. The coefficients of the Fourier expansion for $\phi_0(\theta)$ can be calculated in closed form, as shown in Eq. 4.10 and those coefficients are used to deduce the coefficients of the terms of the Michell solution for that traction field and in turn the corresponding displacement at each node. (This process is outlined in C.2.)

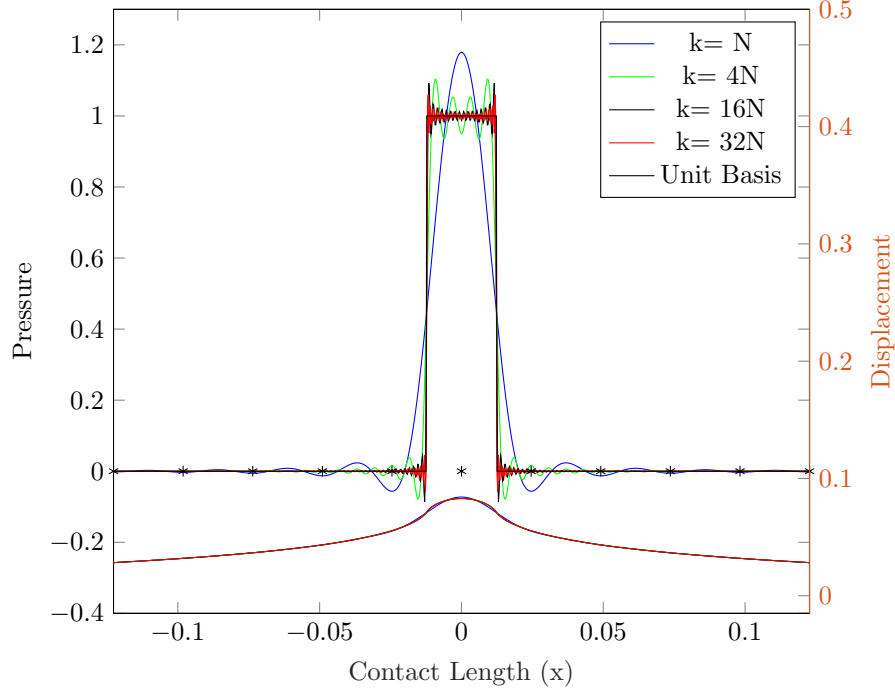


Figure 4.4: The displacement field resulting from the unit pressure over $\Delta\theta$ centered at $\theta = 0$ is obtained by summing a Fourier series. Though there would be Gibbs phenomena if the pressure field were recovered from Fourier series, there is no Gibbs phenomena associated with the displacement field.

$$\phi_0(\theta) = \frac{\Delta\theta}{2\pi} + \frac{2}{\pi} \sum_{k=1}^{Harm} \frac{1}{k} \cos(k\theta) \sin(k\Delta\theta) \quad (4.10)$$

The displacement field corresponding to basis traction $\phi_0(\theta)$ is also expressed in the Fourier series. It should be noted that though there would be a Gibbs phenomenon if it were necessary to construct $\phi_0(\theta)$ from its Fourier series, there are no Gibbs phenomena in the construction of the corresponding displacement field (Fig. 4.4). The convergence of the displacement field with the number of harmonics ($Harm$) depends on the width of $\Delta\theta$ and as one sees from Fig. 4.4 it is more than sufficient to use $Harm = 4\frac{2\pi}{\Delta\theta} = 4N$ harmonics.

The Michell terms (A's and B's) for unit normal and shear tractions over $\Delta\theta$ centered at $\theta = 0$ for the solid elastic disk are listed in the Tab. 4.2. These A's and B's values are substituted in formulae (Eqs.C.6) and the corresponding radial and tangential displacements are evaluated. Eqs.

Terms	Radial Traction	Tangential Traction
A_{01}	$\Delta\theta/(4\pi)$	0
A_{04}	0	$\Delta\theta R^2/(2\pi)$
A_{11}	$\frac{(\kappa - 1) \sin(\frac{\Delta\theta}{2})}{2(1 + \kappa)\pi R}$	0
A_{12}	$\frac{(1 - \kappa)R \sin(\frac{\Delta\theta}{2})}{(1 + \kappa)\pi}$	0
B_{11}	0	$\frac{-(\kappa + 3) \sin(\frac{\Delta\theta}{2})}{2(1 + \kappa)R\pi}$
B_{12}	0	$\frac{-(\kappa - 1)R \sin(\frac{\Delta\theta}{2})}{(1 + \kappa)\pi}$
A_{n1}	$\frac{R^{-n} \sin(\frac{n\Delta\theta}{2})}{n(n + 1)\pi}$	0
A_{n3}	$\frac{R^{2-n} \sin(\frac{n\Delta\theta}{2})}{n(n - 1)\pi}$	0
B_{n1}	0	$\frac{R^{-n} \sin(\frac{n\Delta\theta}{2})}{n(1 + n)\pi}$
B_{n3}	0	$\frac{R^{2-n}(n - 2) \sin(\frac{n\Delta\theta}{2})}{n^2(n - 1)\pi}$

Table 4.2: Michell coefficients for applied radial and tangential unit tractions over $\Delta\theta$ centered at $\theta = 0$ and $r = R$ on the elastic solid disk

4.11 are displacements due to unit radial pressure, Equations 4.12 are displacements due to unit tangential tractions, and the subscript *SD* refers to 'Solid Disk'.

$$\begin{aligned}
w_{0SD}^r(\theta) &= \frac{R(\kappa - 1)\Delta\theta}{8\pi\mu} + \frac{(\kappa - 3 + 4 \ln(R))\kappa R \sin(\Delta\theta/2) \cos(\theta)}{4\pi\mu(\kappa + 1)} \\
&+ \frac{R(1 + \kappa(n - 1) + n) \sin(n\Delta\theta/2) \cos(n\theta)}{2n(n^2 - 1)\pi\mu}
\end{aligned} \tag{4.11}$$

$$\begin{aligned}
u_{0SD}^r(\theta) &= \frac{(\kappa^2 + \kappa - 4 + 4\kappa \ln(R))R \sin(\Delta\theta/2) \sin(\theta)}{4\pi\mu(\kappa + 1)} \\
&+ \frac{R(\kappa(n - 1) - 1 - n) \sin(n\Delta\theta/2) \sin(n\theta)}{2n(n^2 - 1)\pi\mu}
\end{aligned}$$

$$\begin{aligned}
w_{0SD}^\theta(\theta) &= -\frac{(\kappa^2 + \kappa - 4 - 4\kappa \ln(R))R \sin(\Delta\theta/2) \sin(\theta)}{4\pi\mu(\kappa + 1)} \\
&+ \frac{R(1 - \kappa(n - 1) + n) \sin(n\Delta\theta/2) \sin(n\theta)}{2n(n^2 - 1)\pi\mu}
\end{aligned} \tag{4.12}$$

$$\begin{aligned}
u_{0SD}^\theta(\theta) &= \frac{R\Delta\theta}{4\pi\mu} + \frac{(\kappa^2 + 5\kappa + 8 + 4\kappa \ln(R))R \sin(\Delta\theta/2) \cos(\theta)}{4\pi\mu(\kappa + 1)} \\
&+ \frac{R(\kappa(n - 1) + 1 + n) \sin(n\Delta\theta/2) \cos(n\theta)}{2n(n^2 - 1)\pi\mu}
\end{aligned}$$

We used these displacement fields ($w_{0SD}^r(\theta)$, $u_{0SD}^r(\theta)$, $w_{0SD}^\theta(\theta)$, and $u_{0SD}^\theta(\theta)$) to construct a compliance matrix in the later section 4.3.

4.2.3 A Hole in an Infinite Elastic Plane

Next consider another 2D circular geometry – a hole in an elastic infinite plane (see Fig. 4.5). Its stress and displacement fields can also be expressed in terms of the Michell Airy stress function (Eq. 4.3). Terms that are unbounded for large r (especially at $r \rightarrow \infty$) (those associated with $\{A_{01}, A_{03}, A_{11}, B_{11}, A_{n1}, A_{n3}, B_{n1}, B_{n3}\}$) must be dropped. Terms that are multi-value must be dropped or combined so as to remove that feature (Eq.4.7). This results in the following stress function:

$$\begin{aligned}
\Phi_0(r, \theta) = & A_{01}r^2 + A_{03} \ln(r) + A_{04}\theta + A_{23}r^2 \cos(\theta) + B_{23}r^2 \sin(\theta) \\
& + A_{12} \left[r \log(r) \cos(\theta) - \frac{\kappa + 1}{\kappa - 1} r\theta \sin(\theta) \right] + A_{13}r\theta \cos(\theta) \\
& + B_{12} \left[r \log(r) \sin(\theta) + \frac{\kappa + 1}{\kappa - 1} r\theta \cos(\theta) \right] + B_{13}r\theta \sin(\theta) \\
& + \sum_{n=2}^{\infty} \left[(A_{n2}r^{2-n} + A_{n4}r^{-n}) \cos(n\theta) + (B_{n2}r^{2-n} + B_{n4}r^{-n}) \sin(n\theta) \right]
\end{aligned} \tag{4.13}$$

Stresses and displacements were calculated for this stress function using Michell tables ?? and E.2 are shown in the D.1.

4.2.3.1 Creating Surface Displacement Field for a Hole in an Infinite Plane

The hole of radius R in the infinite plane is very finely discretized from $-\pi$ to π with N small nodes, as shown in the Fig. 4.5. A unit pressure $\phi_0(\theta)$ (Eq. 4.10) is applied over an interval $\Delta\theta$ centered at $\theta = 0$. This pressure distribution is expanded in Fourier series (Eq. 4.10) and coefficients are matched to the trigonometric polynomials of stresses (Eqs. D.2), yielding Michell coefficients (Appendix D.2). A similar process is performed with respect to a unit shear traction over $\Delta\theta$. The Michell terms (A's and B's) are listed in Tab. 4.3 for both unit radial and tangential tractions. These A and B values are substituted in the displacement (Eqs. D.7) and yield corresponding radial and

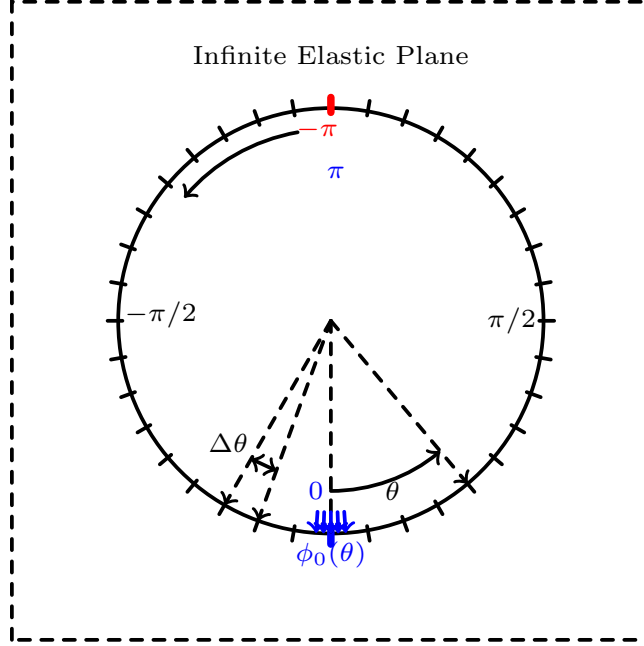


Figure 4.5: An infinite plane with a hole discretized from $-\pi$ to π

Terms	Radial Traction	Tangential Traction
A_{03}	$\frac{\Delta\theta R^2}{2\pi}$	0
A_{04}	0	$\frac{\Delta\theta R^2}{2\pi}$
A_{12}	$-\frac{(\kappa - 1)R \sin(\frac{\Delta\theta}{2})}{(1 + \kappa)\pi}$	0
A_{14}	$-\frac{(\kappa - 1)R^3 \sin(\frac{\Delta\theta}{2})}{2(1 + \kappa)\pi}$	0
B_{12}	0	$\frac{(\kappa - 1)R \sin(\frac{\Delta\theta}{2})}{(1 + \kappa)\pi}$
B_{14}	0	$\frac{(\kappa + 3)R^3 \sin(\frac{\Delta\theta}{2})}{2(1 + \kappa)\pi}$
A_{n2}	$-\frac{R^n \sin(\frac{n\Delta\theta}{2})}{n(n - 1)\pi}$	0
A_{n4}	$\frac{R^{n+2} \sin(\frac{n\Delta\theta}{2})}{n(n + 1)\pi}$	0
B_{n2}	0	$-\frac{R^n \sin(\frac{n\Delta\theta}{2})}{n(n - 1)\pi}$
B_{n4}	0	$\frac{R^{n+2}(2 + n) \sin(\frac{n\Delta\theta}{2})}{n^2(n + 1)\pi}$

Table 4.3: Michell coefficients for applied radial and tangential tractions over $\Delta\theta$ centered at $\theta = 0$ and $r = R$ for the hole in the elastic plane.

tangential displacement fields (Eqs. 4.14 and 4.15). Equations 4.14 are the displacements due to application of unit radial pressure and equations 4.15 are displacements due to unit tangential traction.

$$w_{0Hole}^r(\theta) = \frac{R\Delta\theta}{4\pi\mu} - \frac{(\kappa + 1 - 4\kappa \ln(R))R \sin(\Delta\theta/2) \cos(\theta)}{4\pi\mu(\kappa + 1)} - \frac{R(1 + \kappa(n + 1) + n) \sin(n\Delta\theta/2) \cos(n\theta)}{2n(n^2 - 1)\pi\mu} \quad (4.14)$$

$$u_{0Hole}^r(\theta) = -\frac{(\kappa + 1 + 4\kappa \ln(R))R \sin(\Delta\theta/2) \sin(\theta)}{4\pi\mu(\kappa + 1)} + \frac{R(\kappa(n + 1) + 1 - n) \sin(n\Delta\theta/2) \sin(n\theta)}{2n(n^2 - 1)\pi\mu}$$

$$w_{0Hole}^\theta(\theta) = \frac{(\kappa + 1 + 4\kappa \ln(R))R \sin(\Delta\theta/2) \sin(\theta)}{4\pi\mu(\kappa + 1)} - \frac{R(1 + \kappa(n + 1) - n) \sin(n\Delta\theta/2) \sin(n\theta)}{2n(n^2 - 1)\pi\mu} \quad (4.15)$$

$$u_{0Hole}^\theta(\theta) = -\frac{R\Delta\theta}{4\pi\mu} - \frac{(\kappa + 1 - 4\kappa \ln(R))R \sin(\Delta\theta/2) \cos(\theta)}{4\pi\mu(\kappa + 1)} - \frac{R(\kappa(n - 1) - 1 + n) \sin(n\Delta\theta/2) \cos(n\theta)}{2n(n^2 - 1)\pi\mu}$$

These displacement fields ($w_{0Hole}^r(\theta)$, $u_{0Hole}^r(\theta)$, $w_{0Hole}^\theta(\theta)$, and $u_{0Hole}^\theta(\theta)$) are the displacements on the surface of a hole in an infinite elastic plane for an unit radial and tangential force. These displacement fields can be used to construct a compliance matrix.

4.3 Creating a Compliance Matrix

In previous sections, the pressure-displacement relationships for a solid elastic disk and for a hole in an infinite elastic plane were developed for cases of unit tractions over intervals $\Delta\theta$ centered at $\theta = 0$. In the following, these results are expanded to construct the full compliance matrix.

As before, the surface of the elastic disk is discretized with N nodes evenly distributed over the surface (Fig. 4.3). The inter-nodal distance is $\Delta\theta = 2\pi/N$. Each node corresponds to radial and tangential displacements to their tractions centered on them. Applied traction fields are represented

using $2N$ basis functions is shown in Eq. 4.16.

$$p_r(\theta) = \sum_{k=-M}^{M-1} p_k^r \psi^k(\theta) \quad p_\theta(\theta) = \sum_{k=-M}^{M-1} p_k^\theta \psi^k(\theta) \quad (4.16)$$

where M is half the number of Nodes N , p_k^r and p_k^θ are the radial and tangential tractions at the corresponding $\theta_k = k\Delta\theta$, and $\psi_k(\theta)$ is a basis function centered at θ_k .

At this stage, the basis functions are assumed to form a partition of unity and by symmetry, each basis function is assumed to be obtained from the previous one by a shift of $\Delta\theta$. It would be natural here to use either box functions (Eq 4.4) or chapeau functions (4.5); box functions were chosen because of the simpler expressions that result, but chapeau functions would be only slightly more difficult to implement. The box function ψ_k is defined by

$$\psi_k(\theta) = \phi_0(\theta - \theta_k) \quad (4.17)$$

Similarly, the radial and tangential displacement fields can be expressed

$$\begin{aligned} w^r(\theta) &= \sum_{k=-M}^{k=M-1} w_k^r(\theta) p_k^r + \sum_{k=-M}^{k=M-1} w_k^\theta(\theta) p_k^\theta + W_{tot}^r \\ u^\theta(\theta) &= \sum_{k=-M}^{k=M-1} u_k^r(\theta) p_k^r + \sum_{k=-M}^{k=M-1} u_k^\theta(\theta) p_k^\theta + U_{tot}^\theta \end{aligned} \quad (4.18)$$

where W_{tot}^r and U_{tot}^θ are unknown rigid body constant for radial and tangential displacements, respectively; and

$$\begin{aligned} w_k^r(\theta) &= w_{0SD}^r(\theta - \theta_k), \quad u_k^r(\theta) = u_{0SD}^r(\theta - \theta_k), \\ w_k^\theta(\theta) &= w_{0SD}^\theta(\theta - \theta_k), \quad u_k^\theta(x) = u_{0SD}^\theta(\theta - \theta_k) \end{aligned} \quad (4.19)$$

These relationships are illustrated for $\psi_k(\theta)$ and $w_k^r(\theta)$ for the $k = -1, 0, 1$ in Fig. 4.6. The displacement corresponding to the pressure distribution would be calculated through Eq. 4.18. These linear equations can be employed directly to create a compliance matrix in polar coordinate involving radial and tangential components of tractions and displacements as shown in Eq. 4.21.

Furthermore, the net forces and moments applied to the cylinder must equilibrate the tractions of the contact region as shown in Fig. 4.7. These are introduced in the compliance matrix through the Eq. 4.20.

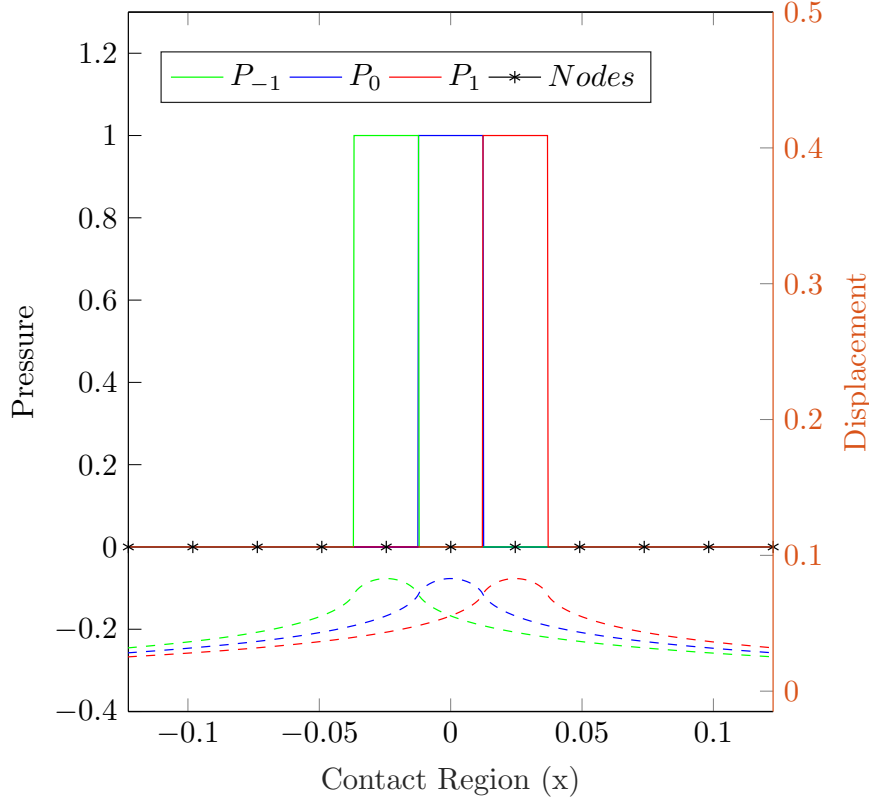


Figure 4.6: On moving the unit normal pressure the corresponding displacement field (dashed) is also moving that is one of the columns of compliance matrix

$$\begin{aligned}
 P &= \sum_{k=-M}^{k=M-1} (-p_k^r \cos \theta_k + p_k^\theta \sin \theta_k) R \Delta \theta, \\
 Q &= \sum_{k=-M}^{k=M-1} (p_k^r \sin \theta_k + p_k^\theta \cos \theta_k) R \Delta \theta, \\
 \text{and } M &= \sum_{k=-M}^{k=M-1} p_k^\theta R^2 \Delta \theta
 \end{aligned} \tag{4.20}$$

The external forces and moments applied to the disk can be imposed either through Michel components that are singular at the center of the disk (such as $r \ln(r) \cos(\theta)$) or more smoothly by tractions imposed on the disk surface. If one is interested only in the traction and displacement fields near contact, St. Venant's principle permits one to use either approach. In fact, if one wants to analyze the stress and displacement fields arising from forces conveyed through a rod going through the center of the disk, the singular forces and moment applied at the center might be more appropriate.

$$\begin{pmatrix} \vdots \\ w_n^r \\ \vdots \\ u_n^\theta \\ \vdots \\ \hline P/R\Delta\theta \\ Q/R\Delta\theta \\ M/R^2\Delta\theta \end{pmatrix} = \begin{bmatrix} C_{rr} & C_{\theta r} & -\cos\theta_n & \sin\theta_n & 0 \\ \vdots & \vdots & \vdots & \vdots & \vdots \\ C_{r\theta} & C_{\theta\theta} & \sin\theta_n & \cos\theta_n & 1 \\ \vdots & \vdots & \vdots & \vdots & \vdots \\ \hline -\cos\theta_n & \dots & \sin\theta_n & 0 & 0 & 0 \\ \sin\theta_n & \dots & \cos\theta_n & 0 & 0 & 0 \\ 0 & \dots & 1 & 0 & 0 & 0 \end{bmatrix} \begin{pmatrix} \vdots \\ p_n^r \\ \vdots \\ p_n^\theta \\ \vdots \\ \hline W_{tot} \\ U_{tot} \\ \theta_{tot} \end{pmatrix} \quad (4.21)$$

where W_{tot} , U_{tot} and θ_{tot} are the rigid body displacements in normal, horizontal and angular directions. P , Q , and M are normal force, lateral force, and moment applied on the disk. The four different parts of compliance matrix C_{rr} , $C_{\theta r}$, $C_{r\theta}$, and $C_{\theta\theta}$ correlate radial displacement to radial traction, tangential displacement to radial traction, radial displacement to tangential traction, and tangential displacement to tangential traction, respectively. Together, these compliance matrices comprise to form the compliance matrix C_{Polar} in polar coordinate. The Goodman decoupling approximation [31] can be implemented by setting $C_{\theta r} = 0$.

However, in most of the contact analyses, we are dealing with problems expressed in terms of rectangular coordinates. This is accommodated by transforming each nodal traction and nodal displacement from polar to rectangular coordinates in the usual manner. Eq. 4.22 shows a single node transform at θ_k .

$$\begin{aligned} p_k^y &= -p_k^r \cos(\theta_k) + p_k^\theta \sin(\theta_k), & p_k^x &= p_k^r \sin(\theta) + p_k^\theta \cos(\theta), \\ w_k &= -w_k^r \cos(\theta_k) + u_k^\theta \sin(\theta_k), & u_k &= w_k^r \sin(\theta) + u_k^\theta \cos(\theta), \end{aligned} \quad (4.22)$$

Formally,

$$C_{\text{Rect}} = T_w^T C_{\text{Polar}} T_p \quad (4.23)$$

where T_w^T and T_p are the rotational transformation matrices for the displacement and pressure, C_{polar} and C_{Rect} are the compliance matrices in polar and rectilinear coordinates. Because C_{Rect} involve

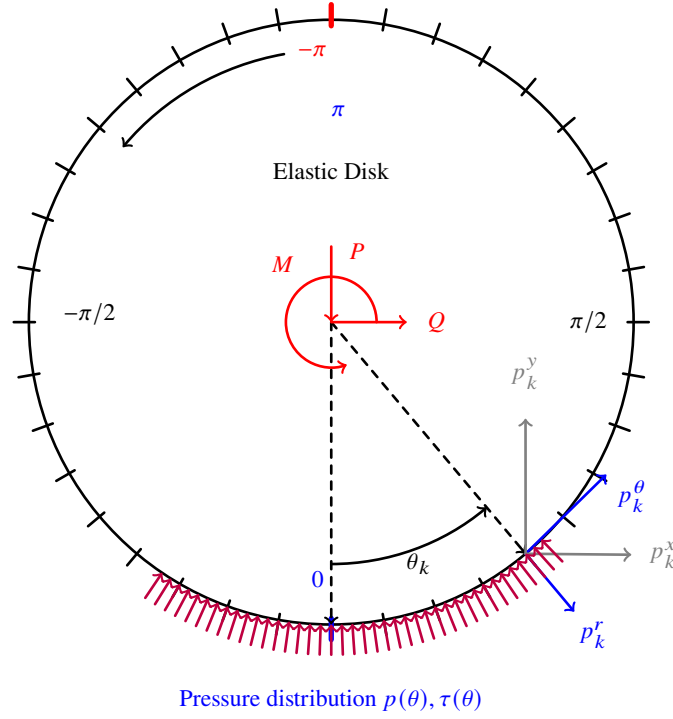


Figure 4.7: Shifting of the displacement basis to create compliance matrix

only nodes in the contact region, it is a fairly small matrix, and the above matrix multiplications would not be onerous; in practice, the transformations are done analytically as the compliance matrix in the rectangular frame is assembled. The final compliance matrix for a solid disk is shown in Eq. 4.24.

$$\left\{ \begin{array}{c} \vdots \\ w_n \\ \vdots \\ u_n \\ \vdots \\ P \\ Q \\ M \end{array} \right\} = \left[\begin{array}{ccc|ccc} & & & \vdots & \vdots & \vdots \\ & C_{yy} & C_{yx} & 1 & 0 & \sin(\theta_n) \\ & & & \vdots & \vdots & \vdots \\ & C_{xy} & C_{xx} & 0 & 1 & \cos(\theta_n) \\ & & & \vdots & \vdots & \vdots \\ \hline R\Delta\theta & \dots & 0 & 0 & 0 & 0 \\ 0 & \dots & R\Delta\theta & 0 & 0 & 0 \\ R^2 \sin \theta_n \Delta\theta & \dots & R^2 \cos \theta_n \Delta\theta & 0 & 0 & 0 \end{array} \right] \left\{ \begin{array}{c} \vdots \\ p_n^y \\ \vdots \\ p_n^x \\ \vdots \\ W_{tot} \\ U_{tot} \\ \theta_{tot} \end{array} \right\} \quad (4.24)$$

where p_n^y and p_n^x are nodal normal and horizontal tractions; w_n and u_n are nodal normal and

horizontal displacements. The four different parts of compliance matrix C_{xy} , C_{yx} , C_{xy} , and C_{xx} correlate normal displacement to normal pressure, normal displacement to horizontal traction, horizontal displacement to normal pressure, and horizontal displacement to horizontal traction, respectively. Together these four matrices comprise the compliance matrix in rectilinear coordinate C_{Rect} . A similar procedure, but using Eqs. 4.14 and 4.15, can be used to calculate as a compliance matrix for the surface of a hole in an infinite plane.

Further, to actually perform analysis of contact between two surfaces, one needs both the discretization of elasticity and a contact algorithm. There are multiple contact algorithms available, such as [1, 4, 18] that could be employed, and the Method of First Violation of [18] was selected because of its robustness. In the next chapter, compliance matrix formulation is employed with the MFV contact algorithm, where it is first verified with available analytical expressions and later used for simulating other contact problems.

4.4 Summary of Compliance Matrix Formulation

An extremely fine discretization strategy for two-dimensional circular surfaces such as disks, long cylinders, and holes in an infinite plane is described in detail. The closed-form analytical expressions of displacement basis are provided to create a compliance matrix. The discretization strategy has several visible benefits with respect to contact analysis.

1. Only degrees of freedom on the surface are involved, resulting in a smaller system of equations than is the case with finite element analysis.
2. The process generates a compliance rather than stiffness matrix, permitting the retention of only the degrees associated with the contact region and associated equations.
3. The strategy facilitates extremely fine meshing over the contact patch, as is necessary to obtain clear resolution of interface tractions and displacements.

CHAPTER 5

VERIFICATION OF COMPLIANCE FORMULATION AND OTHER CONTACT PROBLEMS

Contact problems are notoriously difficult, and most do not have analytical solutions, these that do usually have solutions obtained by virtue of some simplifying assumptions. A particularly important analytical solution is the two-dimensional Mindlin problem of two identical elastic cylinders pressed together by a normal force P and then subject to a shear force Q [52] which is discussed in the previous chapter. These expressions for contact length ($2a$) and normal pressure distribution ($p(x)$) can be used for the preliminary comparisons and verification, and they are available in [6, 56]. Figure 5.1 shows two frictionless concentric disks/cylinders pressed against each other, and Figure 5.2 shows a cylinder pressed against the inside of a hole in a plane. If both bodies are elastic, it is necessary to create commensurate meshes on each body in the vicinity of contact. For a small contact region, analytic expressions for contact length and pressure distribution are shown in Eq. 5.1.

$$a = \sqrt{\frac{2PA}{\pi K}}, \quad p(x) = -\frac{2P\sqrt{a^2 - x^2}}{\pi a^2} \quad (5.1)$$

where, $A = \frac{\kappa_1 + 1}{G_1} + \frac{\kappa_2 + 1}{G_2}$, $K = \frac{1}{R_1} + \frac{1}{R_2}$

where, κ_1 , G_1 , and R_1 are the Kolosov's Constant, shear modulus, and radius of the first cylinder. Similarly, κ_2 , G_2 , and R_2 are properties of the second cylinder. P is the total force applied through the center of the cylinder. By varying these geometric and material properties, we can formulate multiple contact problems and use these expressions to verify the above compliance formulation.

Numerical and analytical results are compared below. Because analytical solutions are usually expressed in terms of normal pressure p and shear traction τ , results are reconciled by observing that for the configurations shown, $p = p^y$ and $\tau = p^x$. Expressions are normalized and non-dimensionalized using Eq. 5.2. \tilde{p} and $\tilde{\tau}$ are the dimensionless normal and lateral tractions. \tilde{w} and \tilde{u} are the dimensionless normal and lateral displacements. \tilde{x} is the dimensionless coordinate along

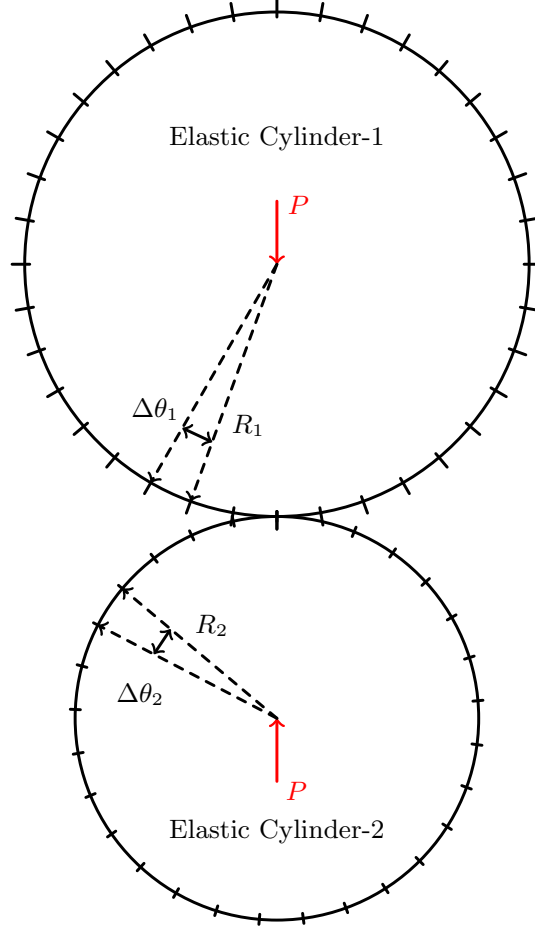


Figure 5.1: Two concentric elastic cylinders pressed against each other

the contact region. \tilde{P} and \tilde{Q} are dimensionless normal and lateral forces.

$$\begin{aligned}
 \tilde{p} &= pA, & \tilde{\tau} &= \tau A, & \tilde{w} &= wK, & \tilde{u} &= uK \\
 \tilde{x} &= \frac{\theta_1 R_1 K}{4\pi} = \frac{\theta_2 R_2 K}{4\pi} \tilde{P} = 4\pi PAK, & \tilde{Q} &= 4\pi QAK
 \end{aligned} \tag{5.2}$$

5.1 Verification Problems

5.1.1 An Elastic Cylinder Pressed against a Rigid Half-plane

The contact problem of an elastic cylinder pressed against a rigid half-plane, can be obtained from the two-dimensional Mindlin solution by setting the radius of the second cylinder R_2 to infinity and setting its shear modulus to infinity as well (consider Fig. 5.1). For this verification case, the geometric and material properties for the first elastic cylinder are radius $R_1 = 2m$, Poisson

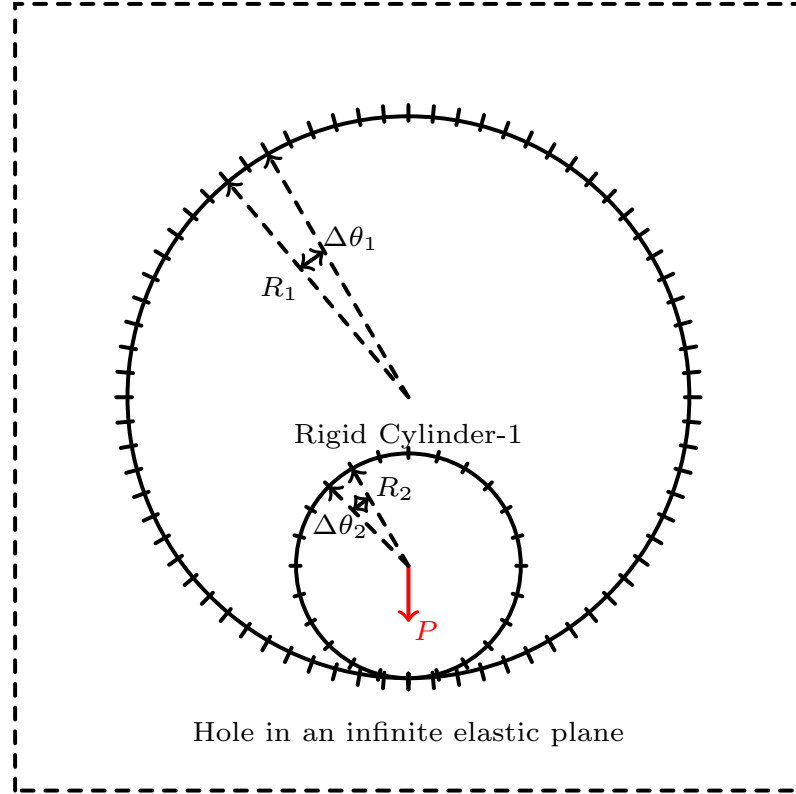
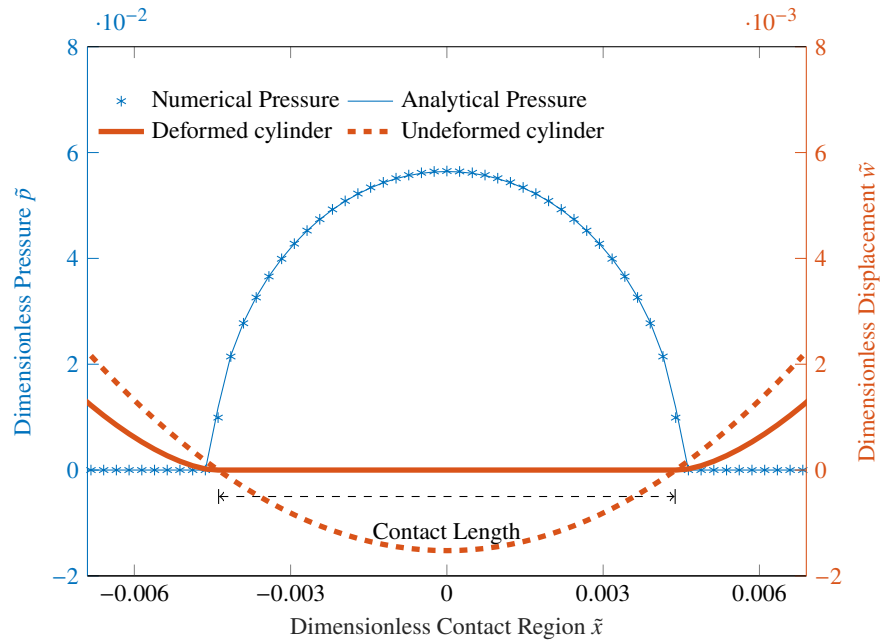


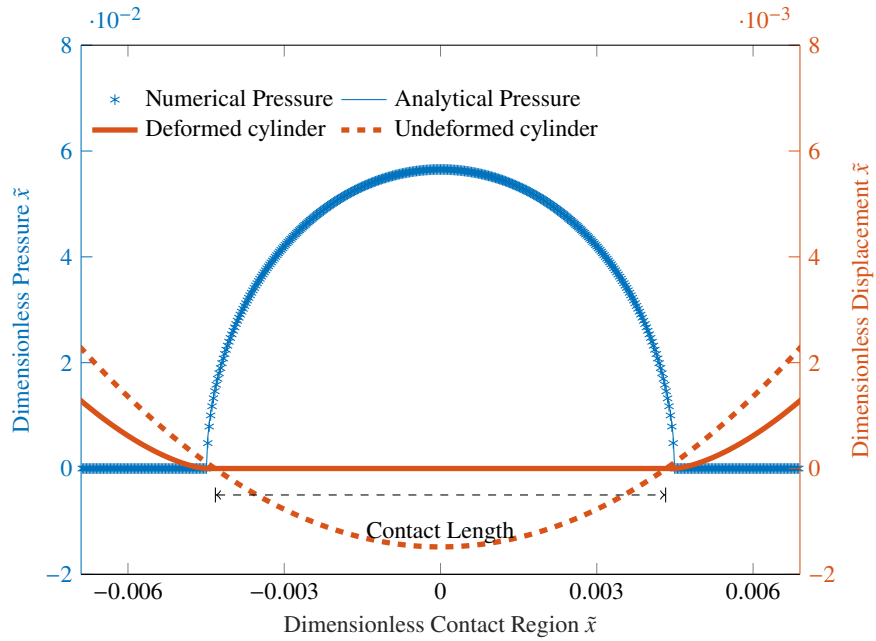
Figure 5.2: A rigid cylinder pressed inside a hole in an elastic half-plane

ratio $\nu_1 = 0.3$, and shear modulus $G_1 = 77GPa$, causing Eq. 5.1 to yield contact parameters $A = 9.1 \times 10^{-12} m^2/Pa$ and $K = 0.5 m^{-1}$. The first cylinder is nominally discretized with 2049 nodes on its surface from $-\pi$ to π with $\Delta\theta = 0.18^\circ$, but in fact only a very small compliance matrix is constructed – involving only degrees of freedom of nodes anticipated to be in the vicinity of contact. The cylinder is pressed with a normal force $P = 1.09 \times 10^9 N/m$ against the rigid surface, resulting in a contact arc of 6.67° and a contact length of $2a = 0.233 cm$ (Eq. 5.1). Figure 5.3 shows that the normalized analytical and numerical pressure fields appear identical. In this calculation, there are 37 nodes in the contact patch, and each load step involved solving an elasticity problem of roughly double that number of equations and degrees of freedom.

The same contact problem is again analyzed using an extremely fine discretization in the anticipated contact region. The cylinder is discretized with 513 nodes from -5° to 5° with $\Delta\theta = 0.0195^\circ$. The normal force P is again $1.09 \times 10^9 N/m$ is resulting in 331 nodes (6.47° contact angle) in contact as shown in the fig 5.3b.



(a) Elastic cylinder pressed against the rigid half-plane: coarse mesh



(b) Elastic cylinder pressed against the rigid half-plane: very fine mesh

Figure 5.3: Comparison of analytical and numerical normal pressure distribution for a elastic cylinder pressed against a rigid half-plane with a coarse mesh (on top) and with a fine mesh (on bottom).

5.1.2 Rigid Cylinder Pressed inside of a Hole in an Infinite Elastic Plane

A rigid cylinder pressed against the inside of a hole in an infinite elastic plane can be constructed by making the first cylinder rigid ($G_1 = \infty$) and changing the radius of the second cylinder to a negative value (as shown in Fig. 5.2). The first cylinder has radius $R_1 = 1m$ and the hole has radius $R_2 = -4m$, Poisson's ratio $\nu = 0.3$ and shear modulus $G_2 = 77GPa$. The hole is discretized to have 513 nodes in the estimated contact region from -1.5° to 1.5° , providing an extremely fine mesh for analysis with $\Delta\theta_2 = 0.0058^\circ$. The rigid cylinder is subject to a normal force $P = 0.104$ resulting in the contact length of $2a = 0.50cm$ and contact angle of 0.5° on the hole. In the numerical solution, 81 nodes on the surface of the hole are in contact with the indenter. Figure 5.4 shows that analytical and numerical pressure distributions appear to be identical.

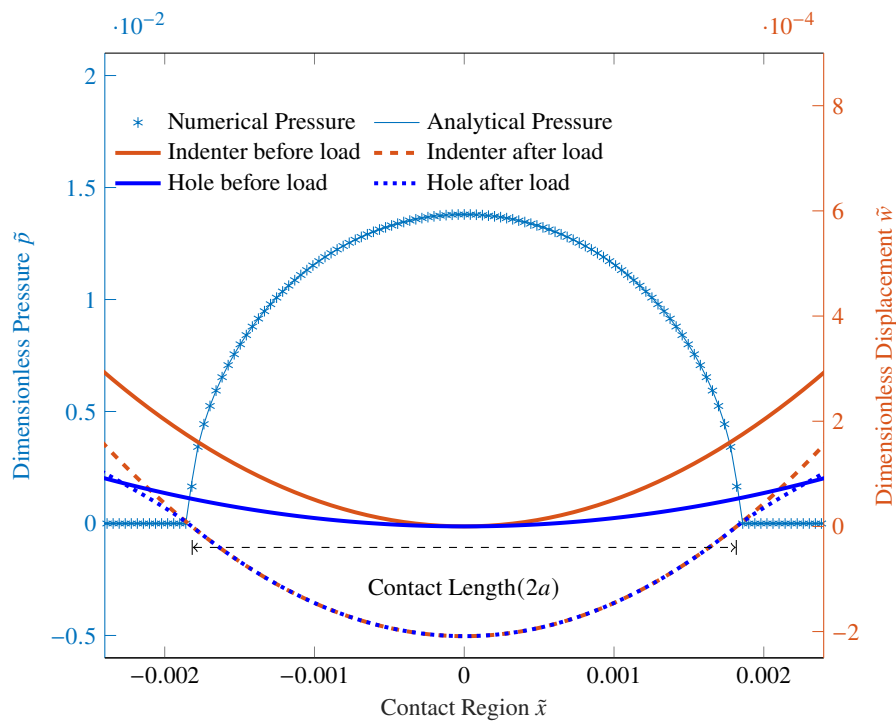


Figure 5.4: Rigid cylinder indenter pressed against a hole inside an infinite elastic plane.

5.1.3 Normal Contact with Friction for an Elastic Cylinder Pressed against a Rigid Half-plane

Consider the case of an elastic cylinder pressed against a frictional rigid half-plane. In this case, the elastic cylinder is discretized with 1025 nodes in the anticipated contact region from -1.5° to 1.5° . The cylinder has the same material and geometric properties as those employed in previous Section 5.1.1. The numerical solution for stick ratio is compared with the same Spence expression discussed in chapter 3 section 3.2.1.

Figure 5.5 shows that the stick ratio from the Spence expression appears identical to the stick ratio calculated from numerical simulation with Goodman decoupling is also imposed. The stick ratio curve with full elastic coupling is only slightly different due to a small Dundur coupling parameter [26, 35].

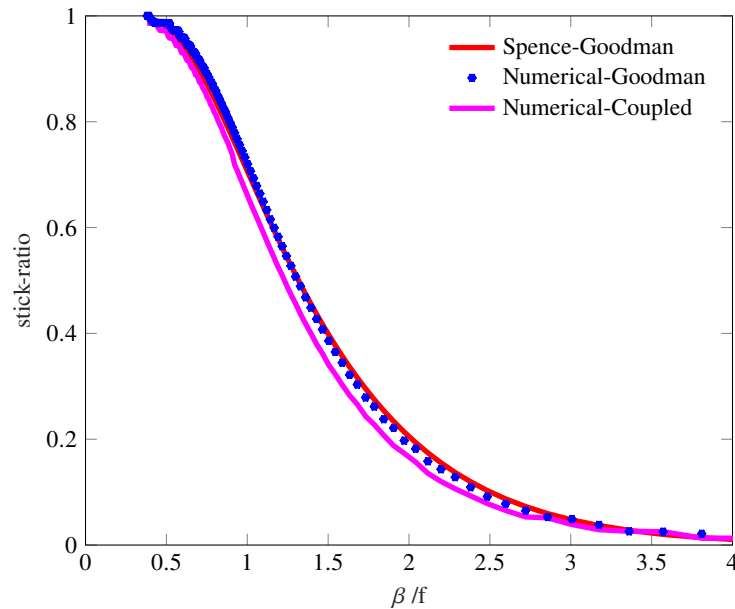


Figure 5.5: Elastic cylinder pressed against a rigid half-plane with friction. The stick ratios for multiple friction coefficients are compared with the analytical expression provided by Spence.

Another contact problem – that of two identical cylinders pressed against each other with normal and lateral forces (the two-dimensional Mindlin problem) – is mapped to the problem of an elastic cylinder pressed against a rigid half-plane in the same manner as the problem of a rigid cylinder pressed on an elastic half-plane, which is discussed in the chapter 3 section 5 with corresponding

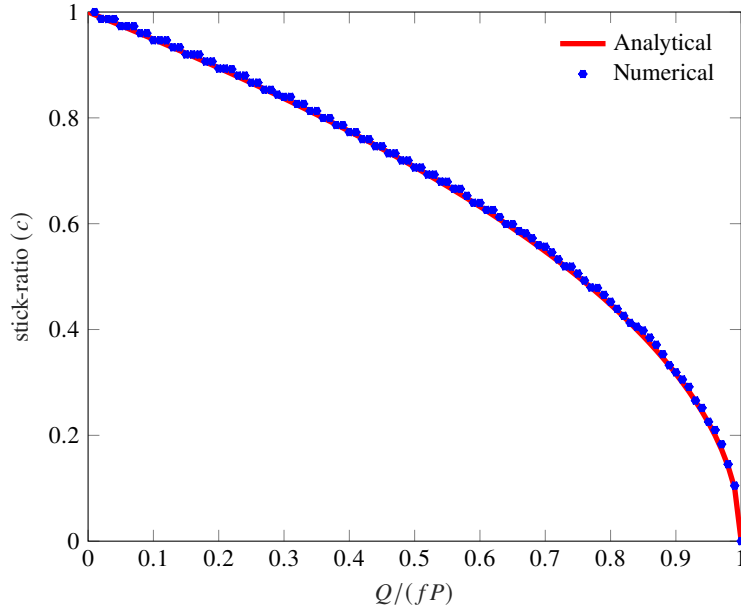


Figure 5.6: Mindlin contact mapping is created using elastic cylinder pressing on a rigid half-plane with friction. Stick ratio for multiple friction coefficients are compared with analytical expression provided by Mindlin.

analytical expressions.

In this verification problem, the elastic cylinder is pressed against the rigid half-plane with normal force $P = 2.2 \times 10^7 N/m$ and then subjected to lateral force $Q = 4.4 \times 10^6 N/m$. The stick ratios are calculated using multiple friction coefficients and compared with analytical results: Fig. 5.6. The distributed lateral tractions fields $\tilde{\tau}(\tilde{x})$ are calculated numerically for four friction coefficients (1, 0.8, 0.6, 0.2) and compared with analytical values as shown in Fig. 5.7. In each of these figures, the numerical results appear to be almost indistinguishable from the analytic values.

5.1.4 von-Mises Stress Distribution in an Elastic Cylinder in Contact

In previous sections, very fine meshes made possible by the compliance formulation introduced here were employed to perform contact calculations with very high resolution of displacements and tractions in the contact patch. Observing that knowing the traction distribution over the surface of a cylinder is sufficient to uniquely determine the Michell coefficients (Tab. 4.2), one may use those coefficients to construct the stress distribution throughout the cylinder explicitly (Eqs. C.2.1). This

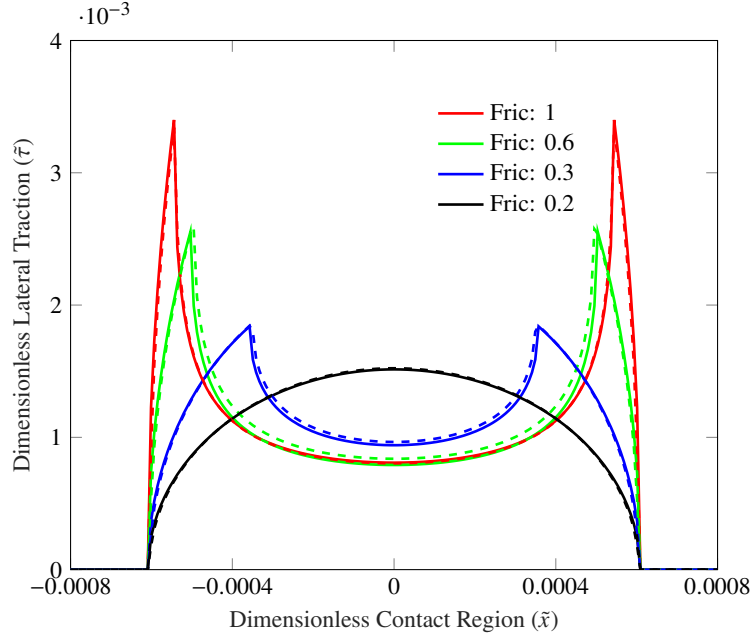


Figure 5.7: The Mindlin two-cylinder contact problem is mapped into that of an elastic cylinder pressed against a rigid half-plane with friction. The numerically calculated lateral traction distribution (connected lines) for multiple friction coefficients are compared with analytical values (dashed lines).

is true also for the case of a hole in the elastic plane (Tab. 4.3 & Eqs. D.2.1).

This construction of the stress field from the results of contact analysis is illustrated on the following problem. An elastic cylinder with the same geometric and material properties as in Section 5.1.1 is pressed against the friction-free rigid plane with normal force $P = 1.09 \times 10^8$, resulting in 33 nodes in contact. Normal and lateral tractions are calculated during the contact analysis that is used with Eqs. C.9 and C.10 to calculate stresses (σ_{rr} , $\sigma_{r\theta}$, and $\sigma_{\theta\theta}$) throughout the interior of the body and these are used to evaluate von-Mises stress. The von-Mises stress is normalized by p_0 and plotted in Fig. 5.8 where the circumferential and radial coordinates are normalized by a , the half-width of the contact patch. The maximum von-Mises stress does not occur on the surface but at a point $(0, 0.71a)$ inside the cylinder. This stress contour plot is almost identical to Figure 3.5(a) of [56].

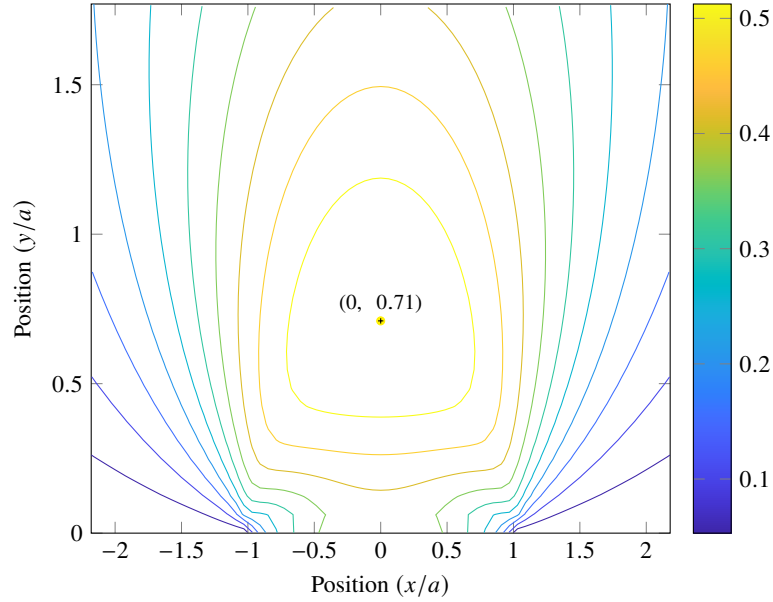


Figure 5.8: Contour plot for normalized von-Mises stress inside the elastic disk on pressing against rigid plane on friction free surface with contact angle 0.64° . The positions are non-dimensionalize with the contact length parameter (a).

5.2 Two Identical Elastic Cylinders Pressed and Sheared

Two identical concentric cylinders are pressed against each other with equal and opposite normal forces $P = 8.24 \times 10^6 N$. Each cylinder has radius $R = 3m$, modulus of elasticity $E = 200GPa$, and Poisson's ratio $\nu = 0.3$. Normal compression of cylinders results in the contact length of $2a = 2.4cm$ and contact angle of 0.47° with 79 nodes in contact. After the normal force has been applied, equal and opposite lateral forces $Q = 2.74 \times 10^6 N$ are applied on the two cylinders. In these numerical experiments, two friction models were employed: the simple Coulomb friction model ($\mu_s = 0.7$), and the two-parameter Coulomb friction model ($\mu_s = 0.7, \mu_k = 0.49$).

Three load cases of contact between identical cylinders are considered:

1. The cylinders are pressed together by a normal force P .
2. Normal force P and then lateral force Q are applied; friction is represented by a one-parameter Coulomb friction model.
3. Normal force P and then lateral force Q are applied; friction is represented by a two-parameter

Coulomb friction model.

The surface tractions and displacements of each of the three cases are shown in Fig. 5.9, and the stress fields near the surface are shown in 5.10.

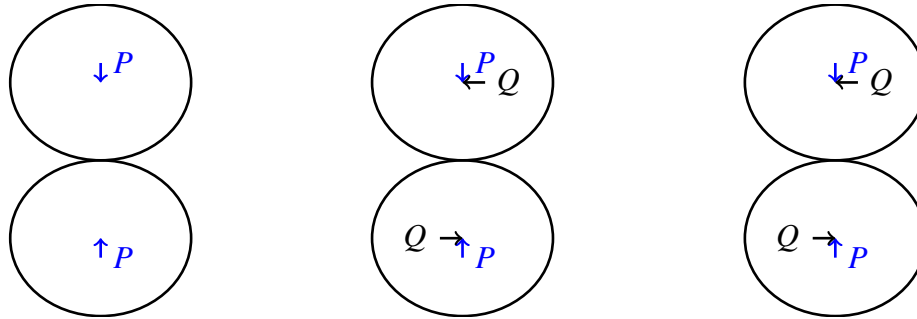
5.2.1 Comparing Surface Traction and Displacement

The numerical tractions and stresses are normalized using $p_0 = \frac{2P}{\pi a}$, and the horizontal and vertical coordinates are each normalized by contact length a . The cases are presented column-wise: the first column is associated with normal loading and, by symmetry, all shear tractions on the interface are zero; the center column shows the effect of a lateral force applied after the normal force and where friction is modeled by the one-parameter Coulomb model; and the right column shows the effect of a lateral force applied after the normal force and where friction is modeled by a two-parameter Coulomb friction model (static and dynamic friction).

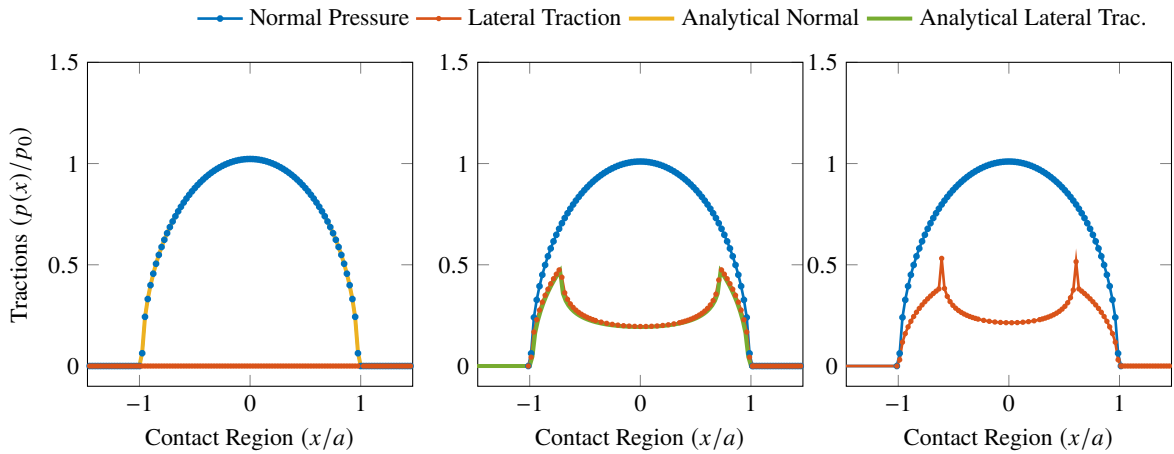
In the first column of Fig. 5.9, the normal pressure distribution from numerical simulation agrees almost exactly with the analytical expressions. The surfaces of the two cylinders are flat in the contact patch. By symmetry, there is no slipping in the contact patch, independent of the friction model. There is an equal lateral displacement on each interface, towards the interface.

In the second column of Fig. 5.9, applied lateral force Q results in lateral traction that is indistinguishable from the analytical distribution. The contact region divides into two slip regions near the edges, with 22 nodes slipping, and a stuck region in the middle with 57 nodes sticking. Lateral displacement differs between the two bodies in the regions of slip.

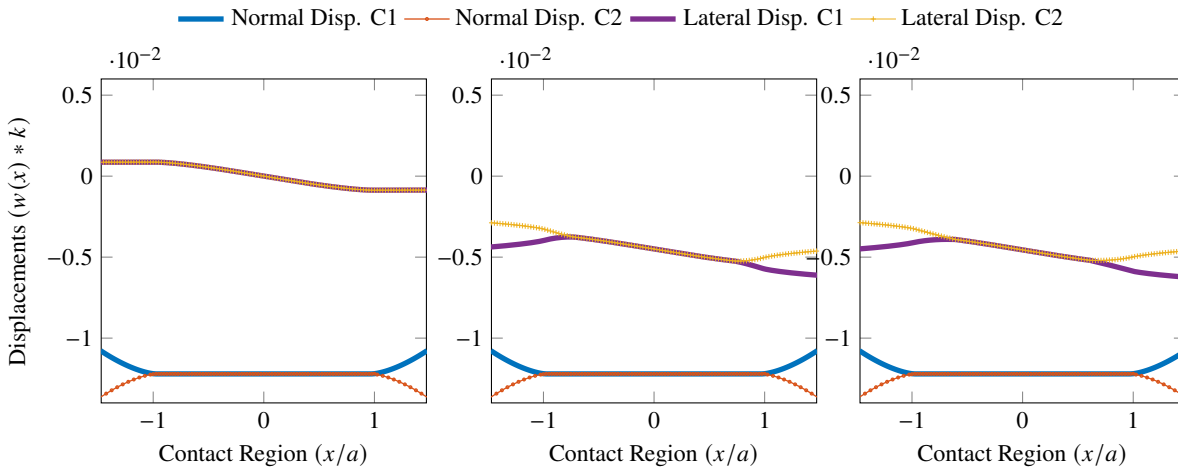
In the third column of Fig. 5.9, the same lateral force Q is applied, but a two-parameter Coulomb friction model ($\mu_s = 0.7$ and $\mu_k = 0.49$) employed. Due to the complexity of the friction model, there are no available analytic expressions to compare against these numerical solutions. The discontinuous nature of lateral traction clearly shows the boundary between the stick region and the slip regions, with 30 nodes slipping and 49 nodes sticking. The stick region reduces by $0.2a$, and relative lateral displacement in the slip region increases compared to the one-parameter



(a) Identical cylinders pressed together by normal force P (left); normal force P applied first followed by application of shear force Q where Coulomb friction μ_s is employed (center); But employing a two-parameter Coulomb friction μ_k, μ_s (right)



(b) Non-dimensionalized normal and lateral tractions ($p(x)/p_0$ and $\tau(x)/p_0$)



(c) Non-dimensionalized normal and lateral displacement fields ($w(x)K$ and $u(x)K$) for cylinder 1 (C1) and cylinder 2 (C2)

Figure 5.9: Surface traction and displacement distributions for three cases: normal force P , only (left); Shear force, Q applied after normal force P and employing a Coulomb friction model (center); Shear force Q applied after normal force P and employing a two-parameter friction model (right).[17]

Coulomb friction case. The normal pressure and normal displacement remain unchanged in all three cases because of the Goodman decoupling approximation.

5.2.2 Comparing Stress Distributions inside the Cylinders

The numerical contact analysis provides the surface tractions at the contact path and those are used, via the Michell expansion, to calculate stresses inside the cylinder. A region from $-2a$ to $2a$ on the surface and extending a distance of $2a$ into the cylinder is chosen to illustrate the stress contours. Stresses due to normal compression of the disks are shown in the first column of Fig. 5.10. Radial stress (σ_{rr}), circumferential stress ($\sigma_{\theta\theta}$), and von-Mises stress (σ_{vM}) are symmetric with respect to y-axis, but shear stress $\sigma_{r\theta}$ is anti-symmetric and is zero on the surface. The maximum von-Mises stress occurs on the y axis at a distance of $0.7a$ from the contact plane, and is consistent with values calculated from the analytic solutions [56, 58].

The application of the lateral force Q leaves radial stress σ_{rr} contours almost unchanged. Small changes are seen in the $\sigma_{\theta\theta}$ as its symmetry breaks down and it slightly increases near the contacting interface. Both friction models provide almost the same σ_{rr} and $\sigma_{\theta\theta}$. The tangential stresses $\sigma_{r\theta}$ and von-Mises stress σ_{vM} differ dramatically from the case of $Q = 0$ due to the non-zero surface shear stresses $\sigma_{r\theta}$.

When the one-parameter Coulomb friction model is employed, the maximum von-Mises stress σ_{vM} occurs either on the contact patch within the slip region or slightly above that, depending on the friction coefficient [58]. In the problem shown, the maximum von-Mises stress occurs near the trailing edge of the contact surface at $0.82a$.

When the two-parameter Coulomb friction model is used, the maximum von-Mises stress σ_{vM} occurs exactly at the stick-slip boundary ($0.62a$).

The stresses fields inside the body are not significantly affected by the choice of using the simple Coulomb friction model or using the two-parameter Coulomb friction model. The differences are visible near the contact interface, and those differences might have significance with respect to material fatigue and failure. The maximum von-Mises stress associated with one-parameter

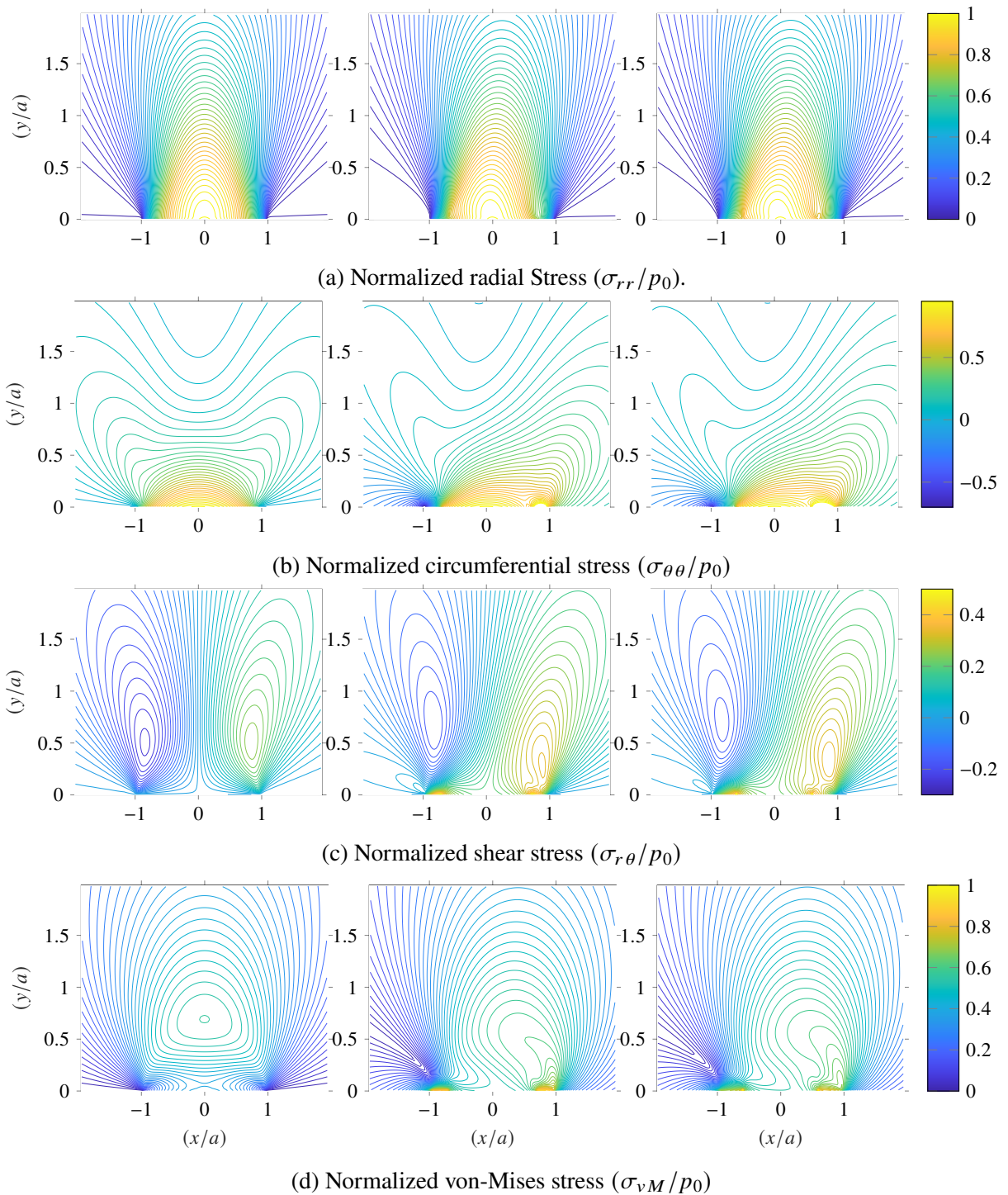


Figure 5.10: Stress distributions for three cases: normal force, P , only (left); Shear force, Q applied after normal force and employing a Coulomb friction model (center); shear force, Q applied after normal force and employing a two-parameter friction model (right). Horizontal and vertical coordinates are normalized by a . [17]

Coulomb friction is located in the trailing slip region, but for the case of two-parameter Coulomb friction, that maximum is located at the trailing boundary of the stick-slip region.

5.3 Summary of the 2D Compliance Verification

The compliance matrix formulation is verified with available analytical expressions for normal pressure, normal displacements, contact length, lateral tractions, and stick ratio. Numerical calculations agree extremely well with analytic results. The compliance formulation has been shown to increase the discretization resolution possible in elastic, frictional contact mechanics.

The contact analysis of two identical cylinders pressed against each other with normal and lateral forces provides a similar distribution of stress fields inside the cylinders for the one-parameter and the two-parameter Coulomb friction models. On the other hand, the tractions and displacements on the contact patch differ between the two friction models, and this difference might have ramifications with respect to friction and failure.

PART III

Comparison of Decoupling Approximations and their Ramifications

CHAPTER 6

ELASTIC DECOUPLING APPROXIMATIONS

Frictional contact is a major part of the tribology universe, yet analytical and numerical tools to provide detailed insight have been elusive. What analytic solutions exist are generally reliant on simplifying assumptions – such as the Goodman decoupling assumption – and where tribological analysis and design is based on those solutions, the decoupling assumptions have to be taken on faith. It has been difficult to assess the validity of these assumptions numerically because of the very fine spatial resolution required in the contact regime and the resulting huge system of equations to be solved at each contact iteration. This numerical limitation has been mitigated recently by the development of a compliance formulation for the case of contact among two dimensional round surfaces such as disks or holes and the validity of the decoupling assumptions has been investigated in the context of such geometries.

6.1 Decoupling Approximations in Elastic Contact

Solving contact problems analytically is extremely complex and only possible for a small number of surface geometries, usually with some level of elastic decoupling approximation. The most common decoupling is the Goodman decoupling (GD) approximation [31] asserting that “normal displacements resulting from lateral traction are negligible compared to the normal displacements resulting from normal traction.” This decoupling approximation has been exploited regularly by researchers such as Mindlin [52] and Spence [63, 64] to provide analytical expressions for the width of the contact patch, stick-slip regions in the contact patch, lateral traction, displacement distributions, and relations between the lateral force and stick-slip ratio in terms of the applied loads or displacements. Another, more severe, decoupling approximation ignores any elastic coupling between normal and lateral loads so that “normal displacement and lateral displacement result only from normal force and lateral force respectively.” [30, 69]. This full decoupling (FD) approximation reduces the complexity of the problem significantly and results in faster though generally not as

accurate predictions. It is most often implemented for understanding cyclic loading and uneven contact where the contact calculations of a coupled system over a very large number of steps would be prohibitive.

Researchers [7, 8, 29, 30] have explored the impact of elastic coupling to understand the process of frictional shakedown behavior (frictional shakedown happens as initial residual tractions and displacements reduces the amount of partial slip during the steady state). The elastic coupling is required to have a shakedown in the contact problem [29, 69]. Because of this, we narrowed our focus to understand the impact of decoupling approximations on contact parameters. Flicek et al. [30] explored the impact of elastic coupling on the contact problem with cyclic shear loading. They measured level of coupling by a norm of matrices and analyzed the effect of initial transient conditions on steady state contact parameters over the range of geometries, material combinations, and friction coefficients. They showed that the coupling effects are higher for the material mismatch than geometric mismatch for a contact problem.

The Goodman approximation is helpful in deriving analytic contact solutions, but its assistance in numerical contact calculations is minimal. On the other hand, complete decoupling facilitates both development of approximate analytic solutions and substantially speeds up numerical calculations - presumably at the cost of accuracy. In this study, effects of Goodman decoupling and full decoupling are assessed by comparison to similar calculations done with full coupling; examining contact parameters such as surface traction distributions, stick ratios, and steady-state dissipation. This numerical investigation is now tractable because of a recently derived compliance formulation for elastic two-dimensional circular bodies, dropping degrees of freedom outside the contact regions from the system of equations to be solved and making extremely fine meshes at the contact tractable. For this study, five different contact configurations are formulated using circular elastic cylinders and holes. Multiple simulations are conducted by varying the lateral load and friction coefficient for each contact problem.

6.2 Analytical Expressions

Most of the analytical expressions have been discussed in the verification process in previous chapters. Some of these expressions represents the level of elastic coupling through material properties and geometries. For a quick refresher, we have reintroduced them here.

$$A = \frac{\kappa_1 + 1}{G_1} + \frac{\kappa_2 + 1}{G_2}, \quad \beta = \frac{\frac{\kappa_1 - 1}{G_1} - \frac{\kappa_2 - 1}{G_2}}{\frac{\kappa_1 + 1}{G_1} + \frac{\kappa_2 + 1}{G_2}} \quad \text{and} \quad K = \frac{1}{R_1} + \frac{1}{R_2} \quad (6.1)$$

A is the measure of the mutual compliance of the two bodies, β is a material mismatch parameter also known as Dundur's parameter, and K is the mean curvature of the contacting bodies. G represents the shear modulus, R denotes the radius of curvature of the body, and κ is the Kolosov's constant (Eq. 3.20 of [6]); with subscripts 1 and 2 refer to each of the two cylinders,

$$\kappa = \begin{cases} 3 - 4\nu & \text{for plane strain,} \\ \frac{3 - \nu}{1 + \nu} & \text{for plane stress} \end{cases} \quad (6.2)$$

where ν is the Poisson's ratio. Parameter β captures the elastic mismatch between the two bodies and is strongly associated with elastic coupling seen in compliance or stiffness matrices.

If the material properties (G and ν) are the same for both elastic bodies ($\beta = 0$) that results in equal amount of transverse yielding in lateral displacement. This corresponds to entire contact region with zero traction for a normal force which is same as employing a full decoupling approximation [17, 69]. If one of the materials is rigid and other one is isotropic elastic, then this choice of materials brings the maximum level of elastic coupling for the analysis [35] because the material mismatch parameter β becomes maximum and is independent of shear modulus.

$$\beta = \frac{\kappa_1 - 1}{\kappa_2 + 1} \quad \text{and} \quad A = \frac{\kappa_1 + 1}{G_1} \quad (6.3)$$

Energy dissipation due to frictional work is one of the contact parameters of interest during cyclic shear loading. It connects vibration-damping analysis with the contact mechanics. During a cyclic shear loading, two contacting surfaces move relative to each other in the slip region. The

friction force in the slip region generates non-conservative and dissipative work which can be calculated numerically by first summing up the frictional work at each interval for a load step and later summing up load steps for a cyclic interval. The analytical expressions for the dissipation due to cyclic shear loading are limited. For two-identical cylinders pressed together and cyclically sheared, Fleury et al. [27, 28] extended the Mindlin solution to provide a closed-form integral expression for the dissipation per unit length:

$$D = \int_{-a}^a 2aA\mu^2 p_0^2 \sqrt{1 - \left(\frac{x}{a}\right)^2} \left[\left(\frac{x}{a}\right) \sqrt{\left(\frac{x}{a}\right)^2 - \left(\frac{b}{a}\right)^2} - \left(\frac{b}{a}\right)^2 \log \left(\frac{x}{b} + \sqrt{\left(\frac{x}{b}\right)^2 - 1} \right) \right] dx \quad (6.4)$$

The dimensionless dissipation per cycle is defined

$$\begin{aligned} \mathcal{D} &= \frac{D}{P^2 A} \frac{8\mu^2}{\pi^2} \int_{-a}^a \sqrt{1 - (s)^2} \left[s\sqrt{s^2 - c} - c^2 \log \left(\frac{s}{c} + \sqrt{\left(\frac{s}{c}\right)^2 - 1} \right) \right] ds \\ &= \frac{8\mu^2}{\pi^2} \mathcal{G}(c) \end{aligned} \quad (6.5)$$

where, $s = \frac{x}{a}$ and $c = \frac{b}{a}$ is a stick ratio during cyclic shear loading at maximum shear force.

Note that because the above expression is for identical cylinders pressed together, therefore $\beta = 0$, and it does not provide insight into coupling, but it will be shown to be a useful nondimensionalization.

6.2.1 Contact Problems

Simulations are performed for fully coupled, partly coupled (Goodman), and fully decoupled analyses for multiple load combinations and following five different geometries:

1. A rigid indenter of radius $0.97R$ is pressed inside a elastic circular hole of radius R ($KR = 0.03$).
2. A rigid indenter of radius $0.5R$ is pressed inside a elastic circular hole of radius R ($KR = 1$).
3. A elastic cylinder of radius R is pressed over a rigid half-plane ($KR = 1$).

4. A elastic cylinder of radius R is pressed over a rigid cylinder of radius $0.5R$ ($KR = 3/2$).
5. A elastic cylinder of radius R is pressed over a rigid cylinder of radius R ($KR = 2$).

Note that the radius R is the larger of the radii of each configuration and the dimensionless quantity KR could range from zero to infinity, but in these analyses the range of KR is from 0.03 to 2.0 (In the numerical calculations performed for this study R had a value of 4.0 meters, but the particular value of R becomes irrelevant after normalization and non-dimensionalization). In all calculations, shear modulus of the larger cylinder (or hole) $G = 77$ GPa, Poisson's ratio $\nu = 0.3$ and coefficient of friction $\mu = 0.7$ is assumed. In each case, the larger cylinder (or hole) is elastic and the smaller one is rigid.

6.3 Surface Traction for a Cyclic Lateral Force

In this case, a rigid cylinder is pressed against the inside of an elastic hole of twice its radius. The indenter is pressed with sufficient force $P = 8.0 \times 10^7 N$ to cause a contact area of $2a = 0.022R$; this corresponds to 1.26° of the surface of the hole. After the normal load is imposed, a cyclic lateral force $Q = 0.65\mu P$ is applied to the rigid cylinder. The numerical experiments are conducted with three levels of elastic coupling: full elastic coupling (FC), Goodman decoupling (GD), full elastic decoupling (FD). The resulting surface tractions are shown in figure 6.1. There are three columns: the first column with FC, the second with GD, and the third is associated with the FD.

In the first row of Fig. 6.1, the indenter is pressed against the hole with normal force P . The resulting normal traction is symmetric about the y -axis, but the contact patch and the pressure distribution are a little narrower for the fully coupled case than for the GD and FD cases because of the retarding effects of surface shear traction. The lateral traction is self-equilibrating and anti-symmetric about the y -axis for FC and GD. For the full decoupling case, there is no lateral traction caused by the application of the normal load.

The second row of Figure 6.1 corresponds to a lateral force Q applied while the indenter remains pressed against the surface of the hole. For the GD and FD analyses, the normal pressure distribution remains unchanged from that calculated in the previous step (recall that for GD and FD

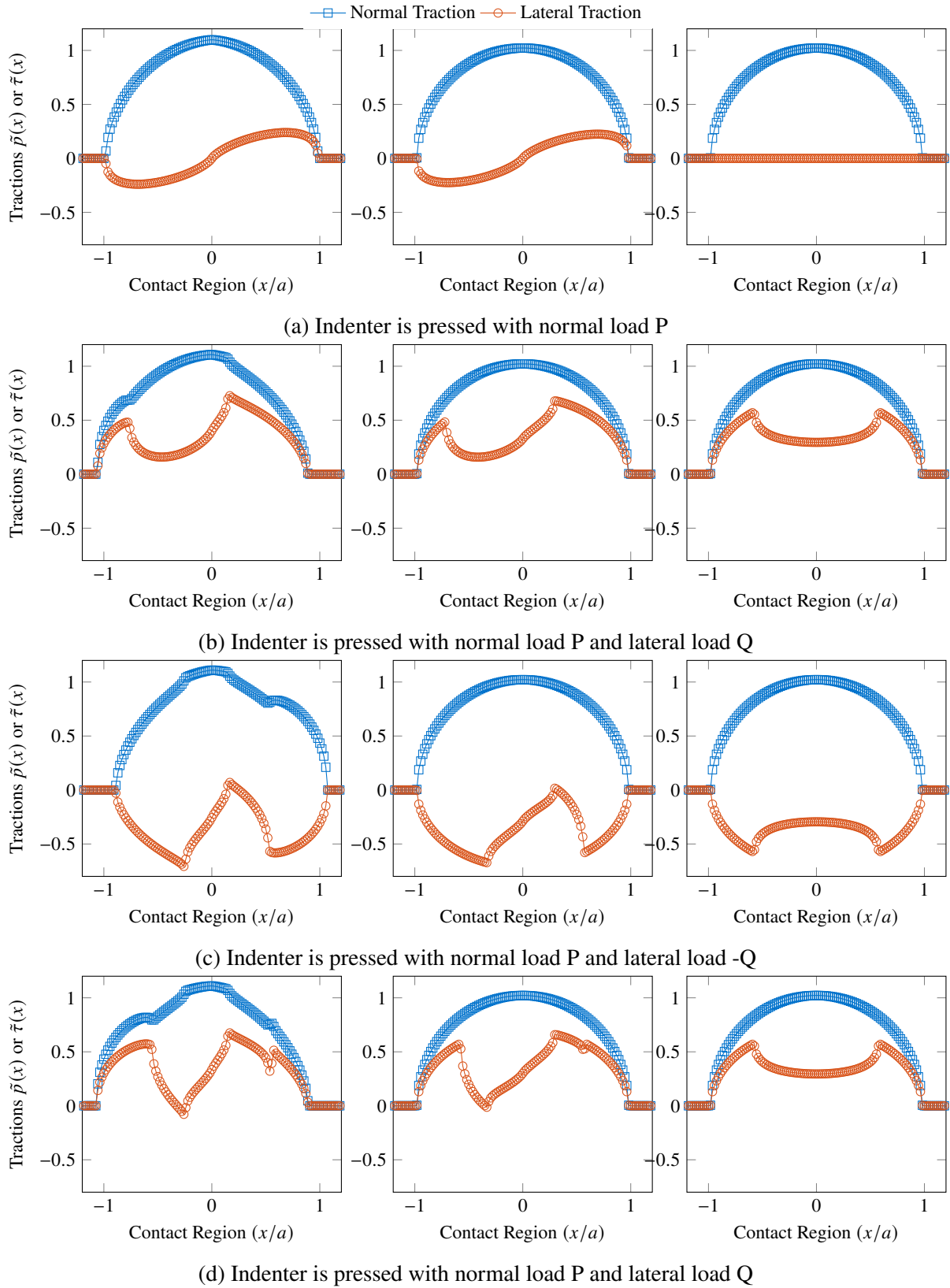
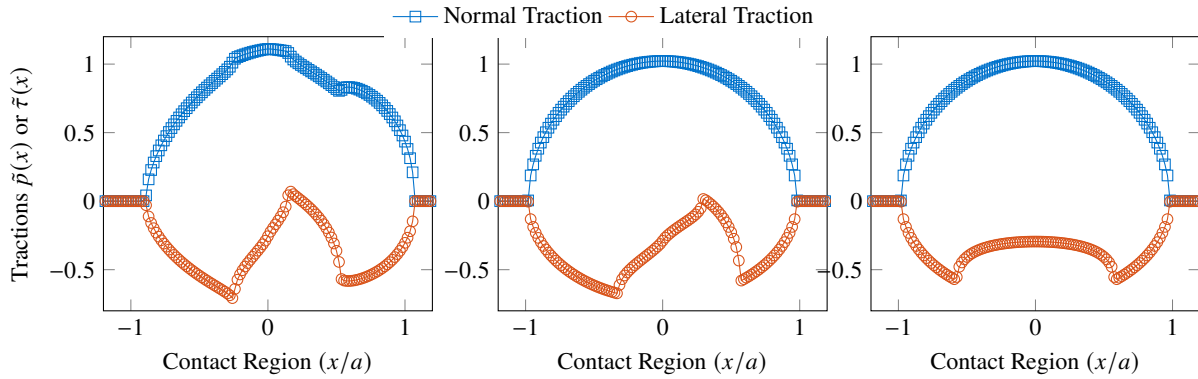


Figure 6.1: Surface traction distributions for three cases: fully coupled (FC) (in left); Goodman decoupled approximation (GD) (in center); fully decoupled approximation (FD) (in right).

Figure 6.1 (cont'd):

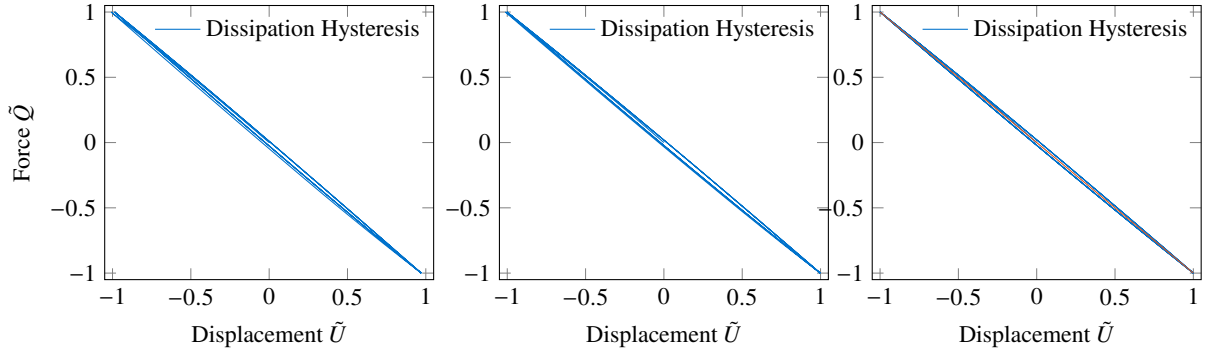


analyses the shear tractions do not influence normal displacement). However, for the FC analysis, normal traction does change slightly from the previous case as symmetry is lost due to coupling with the shear traction. Also, the contact region is shifted to the left by $0.1a$. The lateral traction distributions for the FC and GD cases are similar and both distributions lose symmetry on the application of the lateral force. In the case of FD, lateral traction is symmetric.

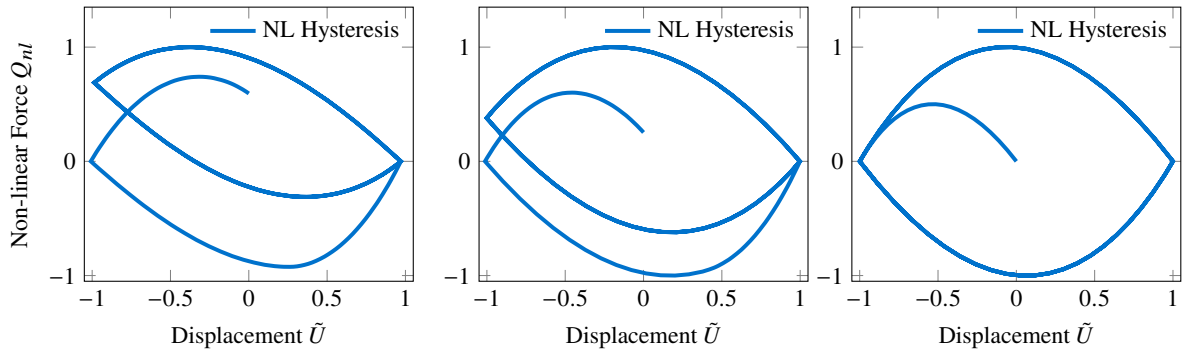
In the third row of Fig. 6.1, the applied lateral force is slowly reversed to $-Q$. The normal traction for FC is changed again; the shape is altered to have one more inflection and the contact region shifts toward the right by $0.2a$. One can identify the stick and slip region boundaries through the inflections in normal traction distribution. The lateral traction reflects the shift in the contact patch as well. For the GD case, the normal traction distribution is unchanged and the shear traction is similar to, though distinguishable, from that of the FC case. For the FD analysis, the lateral traction distribution is reflected vertically.

The fourth row of the Fig. 6.1 reflects the applied lateral force slowly reverting to Q to complete a cycle. For the FC case, the normal traction continues to evolve and acquires another inflection and the lateral traction also changes, acquiring one more local maximum. For the GD analysis, the lateral traction distribution continues to show qualitative similarity to that of the FC case. For the FD case, the lateral traction is the same as that of step 2 where Q had the same value.

The fifth row of the Fig. 6.1 has to do with reversing the shear force again to $-Q$. Of course, the tractions in FD case are identical to those of step three when the shear and normal forces were



(a) Normalized dissipation hysteresis where \tilde{Q} and \tilde{U} are normalized with force Q and maximum U_{tot} from FD respectively



(b) Non-linear part of Hysteresis

Figure 6.2: Normalized dissipation hysteresis and non-linear part of hysteresis: fully coupled (in left); Goodman decoupled (in center); fully decoupled (in right). Non-linear part is generated by removing the linear

the same. Particularly interesting are the tractions of the FC and GD analyses, where the normal and shear tractions appear to have reverted to what they were in Step 3. From this point on, the traction distributions at the end of each shear loading are exactly what they were in the previous step having that shear load. The same surface traction behavior is observed for the other four contact geometries.

From the above, one can observe that though the normal traction distribution associated with the GD analysis can be remarkably different from that of the FC analysis, but the shear tractions are quantitatively very similar. The FD analyses show extremely different shear tractions profiles than either the FC or GD cases.

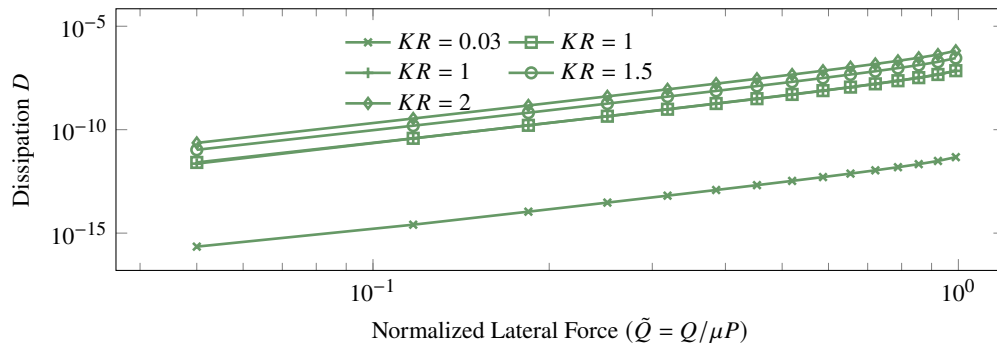
Frictional dissipation is associated with wear and is also important as a source of vibration damping, but in addition it provides some insight into frictional contact. The contact formulation

employed here provides net force on each body and net relative displacement at each point in the cycle. These histories are used to construct the hysteresis curves shown in Fig. 6.2a. Once the curves become closed, a steady-state has been achieved and the area within the curve is the dissipation per cycle. Because these frictional contact are *almost* elastic, these curves result in almost linear and difficult to differentiate. This limitation is addressed by subtracting its linear part from each curve (figure 6.2b). For the FC and the GD, the first three-quarters of the first cycle reflects the effect of the initial shear traction distribution. Once a steady-state is achieved, the dissipation per cycle is the area enclosed by the loop. For the FD case, the steady-state curve results after a quarter cycle. If scaled in the same way (removing the same linear part), steady-state curves for GD and FD are nearly identical and result in the same dissipation.

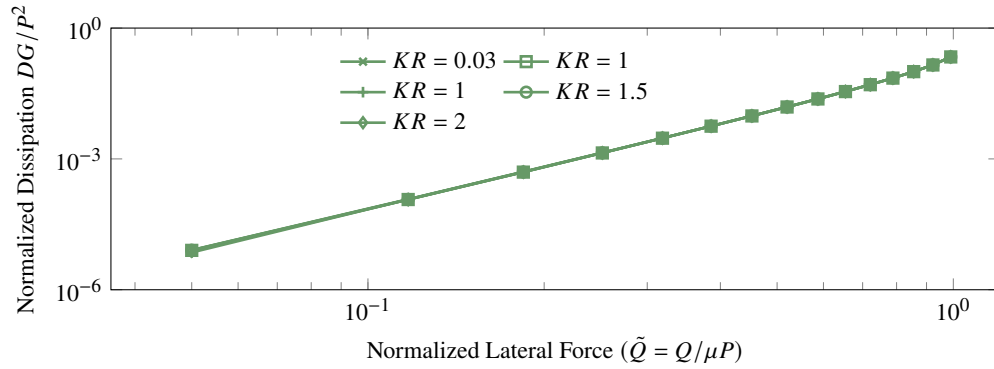
6.4 Variation with Lateral Force

The five contact geometries discussed in the section 6.2.1 are simulated over a range of shear load amplitudes. For each case, four load cycles are simulated resulting in at least three steady-state cycles. Dissipation and stick ratio for all three coupling choices are calculated and compared. Also, the L_1 norm in each case is calculated for the differences between the FC tractions and those of the GD and FD approximations. In each case the larger-diameter body is treated as elastic with the parameters employed in Section 6.3 and the other body is treated as rigid. The applied normal force P is adjusted for geometry such that the contact patch will have a width of 0.088m with a contact angle of 1.26° relative to the larger diameter body. The elastic parameters A and β are the same for all geometries though the curvature K (defined Eq. 6.1) will differ for each geometry.

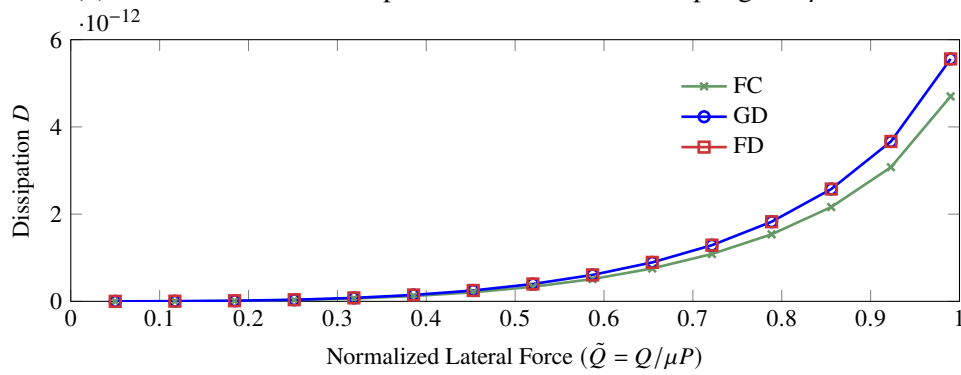
For each contact geometry, steady-state dissipation is calculated and plotted against the normalized lateral force ratio ($\tilde{Q} = Q/\mu P$) for FC as shown in Fig 6.3a. As expected, dissipation increases with increase in lateral load. Each contact geometry (KR) is associated with a different dissipation curve. On the other hand, when properly normalized and nondimensionalized, all the dissipation curves converge to a single curve (Fig. 6.3b) – this is anticipated from the nondimensionalization of the relevant integral equations. The log-log plot of dimensionless dissipation vs dimensionless



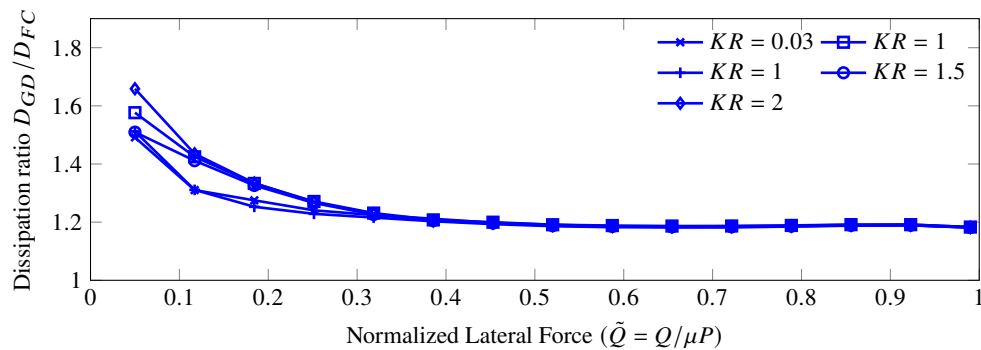
(a) Dissipation values with full elastic coupling and $\mu = 0.7$



(b) Non-dimensional Dissipation with full elastic coupling and $\mu = 0.7$



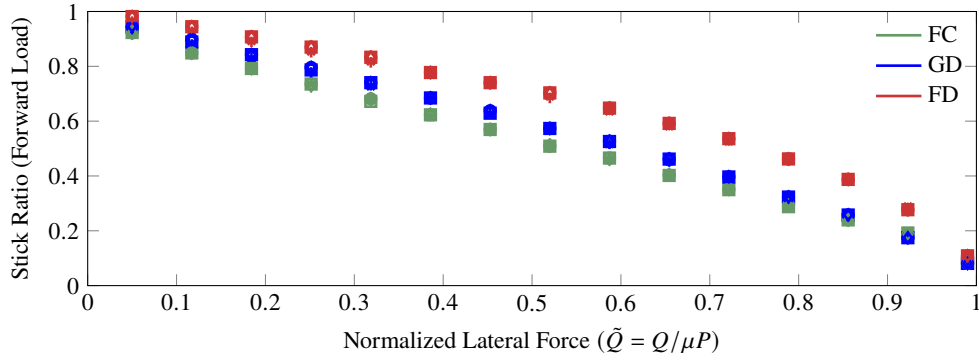
(c) Dissipation values for $KR = 1$ with $\mu = 0.7$ friction coefficient



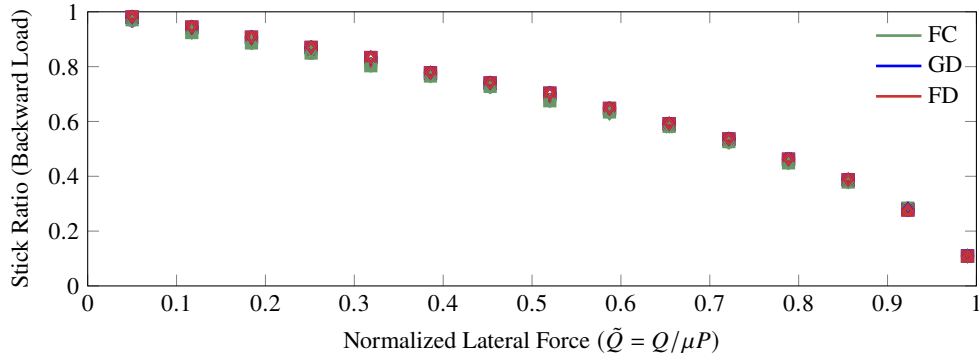
(d) Ratio of Goodman dissipation to fully coupled dissipation with $\mu = 0.7$

Figure 6.3: For the five contact geometries, contact parameters such as Dissipation, Stick ratio, and errors in surface tractions are plotted against over a range of lateral force (\tilde{Q}). All calculation involved $\mu = 0.7$ friction coefficient.

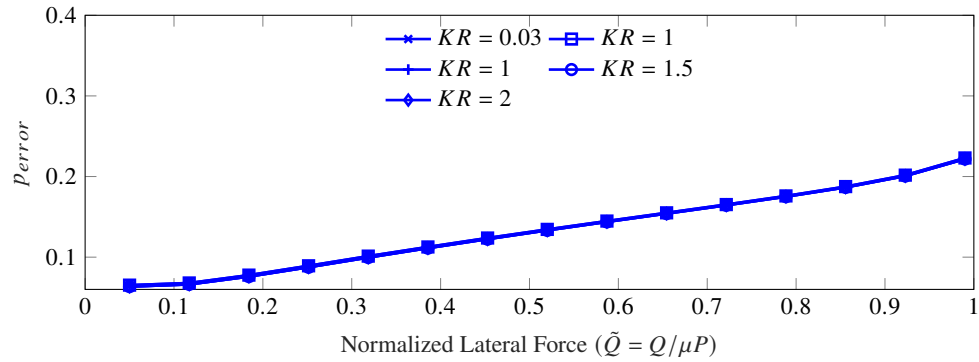
Figure 6.3 (cont'd):



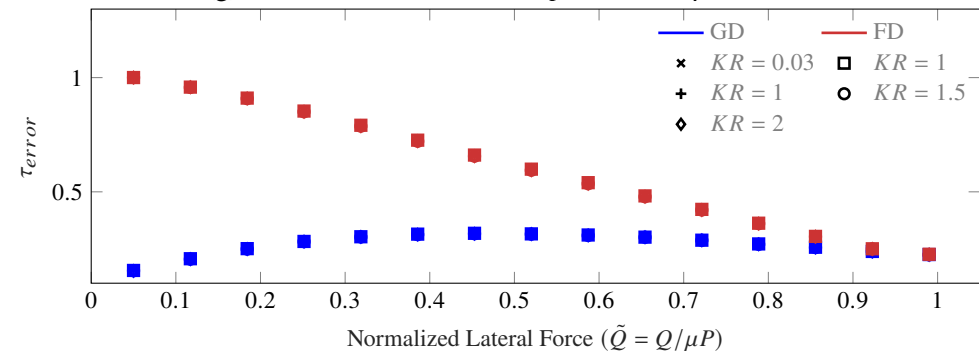
(e) Stick ratio after a forward lateral load with $\mu = 0.7$



(f) Stick ratio after a backward lateral load with $\mu = 0.7$



(g) Errors in Normal traction p_{error} with $\mu = 0.7$



(h) Errors in Lateral traction τ_{error} with $\mu = 0.7$

shear force is nearly linear over the range of loads applied. At low values of load, the slope of the curve for this FC problem is roughly 3.15. For each decoupling approximation, dissipation is calculated with varying lateral force as shown in figure 6.3c. When plotted on a log-log graph (not shown here), the slope is close to 3.0 – as suggested in [32]. Dissipation values are nearly equal for GD and FD, which are higher than those of the FC analysis at each level of lateral force. The dissipation values for GD are divided by dissipation values of FC, and the resulting values are plotted in Fig. 6.3d. This plot indicates that the decoupling approximations over-predict dissipation by 20% to 50% as compared to the full coupling solution. These ratios are independent to the mean curvature (K).

Figure 6.3e and 6.3f show the stick ratios for forward shear load and the reverse direction load respectively. The stick-ratios for all three couplings are independent of the mean curvature (K). In the case of backward lateral loading ($-Q$), stick ratios are nearly the same for all three coupling cases. It is in application of the initial shearing load that the cases differ. Stick ratios are lowest for FC contact, highest for FD contact, and intermediate for the GD case. For the case of FD contact, the stick ratios are the same for both loading and unloading.

Errors in the surface tractions due to the GD and FD approximations are calculated with aid of the L_1 norm using the following relation:

$$\begin{aligned}
 p_{\text{error}} &= \frac{\int |p(x) - p(x)^{\text{FC}}| dx}{\int |p(x)^{\text{FC}}| dx} = \frac{\sum_{i=1}^N |p_i - p_i^{\text{FC}}| \Delta x}{\sum_{i=1}^N |p_i^{\text{FC}}| \Delta x}, \\
 \tau_{\text{error}} &= \frac{\int |(\tau(x) - \tau(x)^{\text{FC}})| dx}{\int |\tau(x)^{\text{FC}}| dx} = \frac{\sum_{i=1}^N |\tau_i - \tau_i^{\text{FC}}| \Delta x}{\sum_{i=1}^N |\tau_i^{\text{FC}}| \Delta x},
 \end{aligned} \tag{6.6}$$

where p^i , and τ^i are nodal normal and lateral tractions respectively, while superscript FC represents the tractions for full elastic coupling; N is the total number of nodes in the contact region and Δx is the length of the interval.

By assumption, the normal traction distributions for GD and FD do not change with change in the lateral load though those of the FC cases do, so it is sufficient to show the error in normal traction calculated for GD as shown in Fig. 6.3f. The error increases from 0% to 23% with increase in the lateral force. Error in lateral traction is calculated for both GD and FD and shown in Fig. 6.3g. For

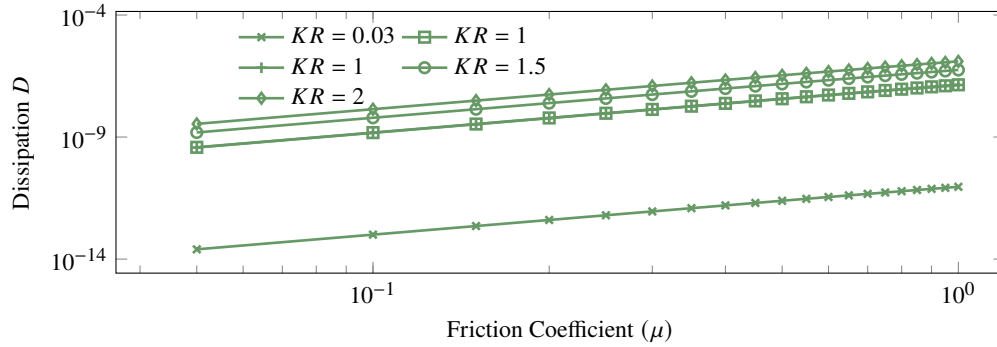
the GD case, error in lateral traction first increases to a maximum of 35% and later reduces to 20% with increase in lateral force. For the FD case, error in lateral traction reduces with an increase in lateral force from 100% to 20%. For small lateral load, the lateral traction distribution is similar for GD and FC. This is understood by observing that at zero lateral load the shear traction of the FD case is zero – representing 100% error with respect to the FC case.

At very high lateral load, nearly all of the the contacting region starts to slip, resulting in 20% error for GD and FD because the contact region shifts by $0.1a$ for FC.

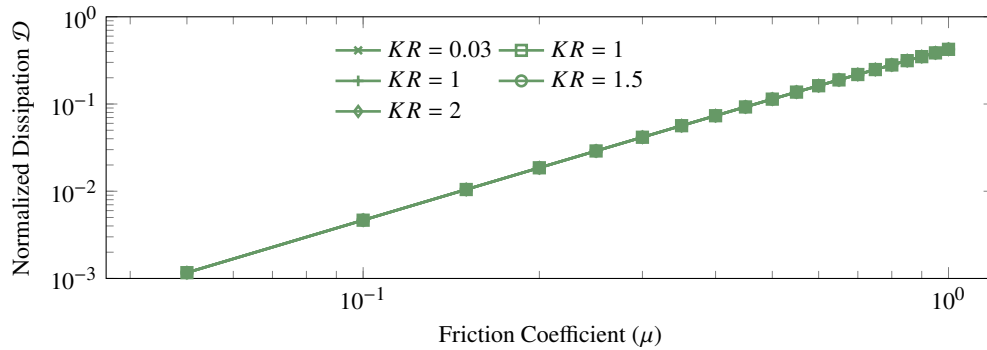
6.5 Variation with Coefficients of Friction

Again, the same five contact geometries are simulated over the range of friction coefficients (from 0.05 to 1) , but with a fixed lateral force ratio ($\tilde{Q} = Q/\mu P = 0.99$). The applied normal forces (P) and the elastic properties (A and β) are the same as in the previous case such that the contact patch has a width of 0.088m for all five geometries. Steady-state dissipation and errors in the surface tractions are compared for the five contact geometries as shown in Fig. 6.4. Numerical simulations (not shown here) indicate that in either forward or reverse loading, so long as the force ratio \tilde{Q} is constant, there is little dependence on coefficient of friction μ .

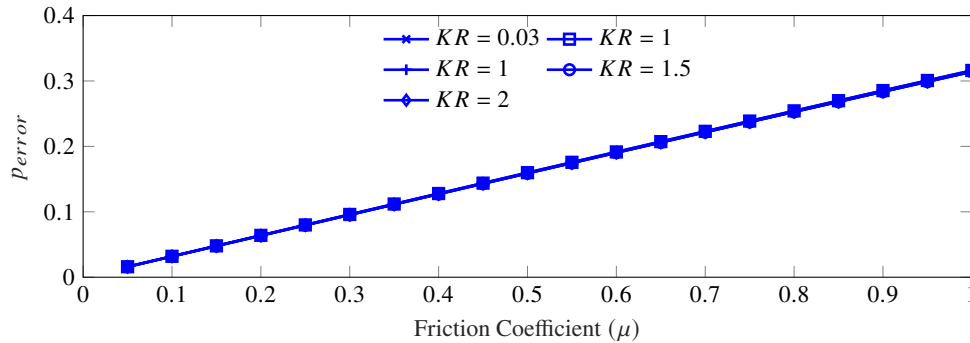
The steady-state dissipation is calculated and plotted against the friction coefficients. The dissipation increases with the increase in friction coefficient and also with the increase in KR , as shown in Fig. 6.4a. Again on non-dimesionalizing the dissipation, all dissipation curves converge to a single curve, as shown in Fig. 6.4b and become independent of mean curvature values, also expected by the dissipation Eq. 6.5. The log-log plot of dissipation against friction coefficients is linear in nature. The slope of the curve is 2 for all three cases (FC, GD, and FD), which represents a quadratic relation also anticipated from the dimensionaless dissipation equation 6.5. Errors in surface traction are calculated over the range of coefficients of friction using Eq. 6.6 that result independent of the mean curvature value K . Figure 6.4 shows that both errors in normal and lateral traction increase with the increase in the coefficient of friction and are independent of the decoupling approximation due to tiny stick region at high lateral force ratio ($\tilde{Q} = 0.99$). The



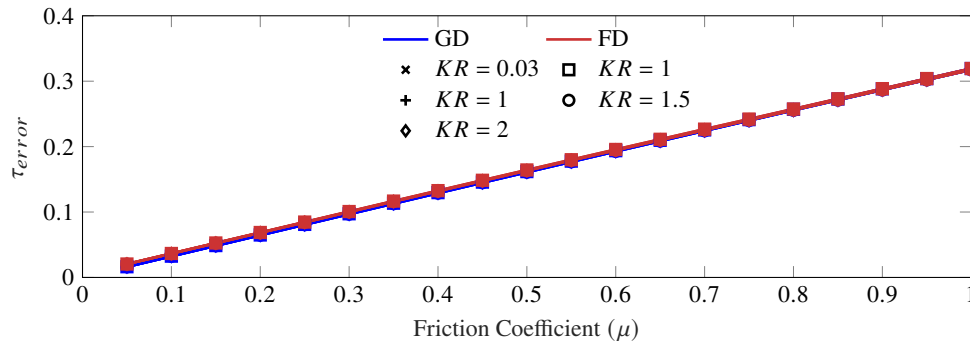
(a) Dissipation with full elastic coupling and $\tilde{Q} = 0.99$



(b) Non-dimensional dissipation values with full elastic coupling and $\tilde{Q} = 0.99$

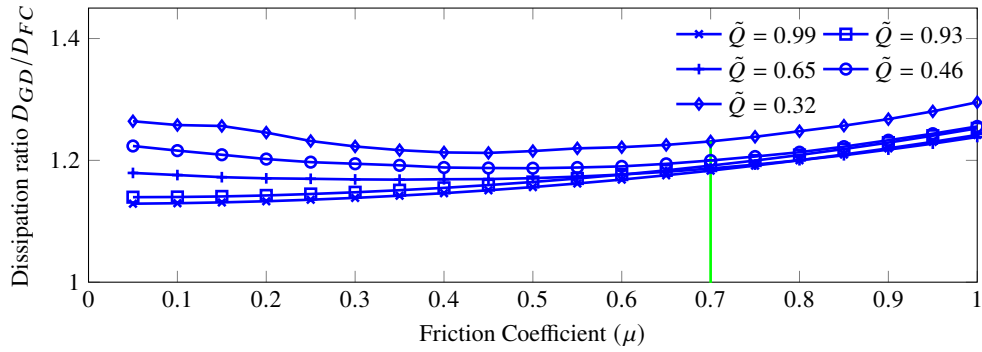


(c) Errors in Normal traction p_{error} with $\tilde{Q} = 0.99$

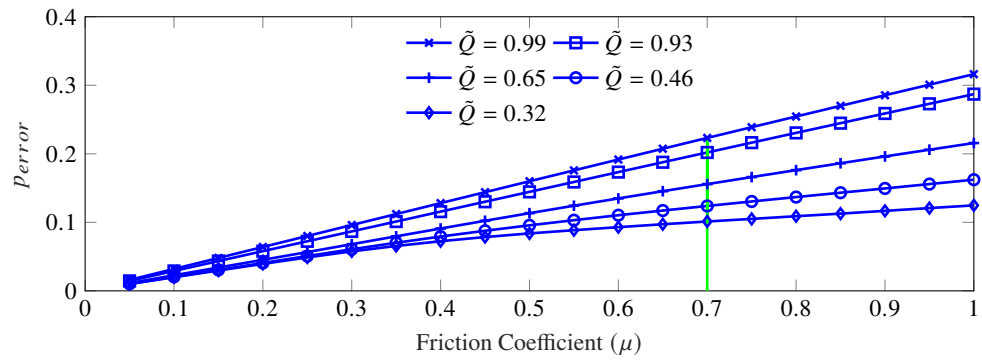


(d) Error in Lateral traction τ_{error} with $\tilde{Q} = 0.99$

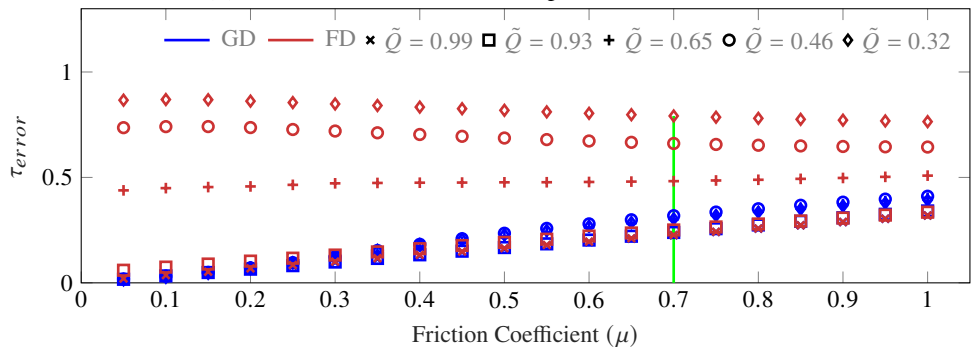
Figure 6.4: For the five contact geometries, contact parameters such as Dissipation, Stick ratio, and errors in surface tractions are plotted against over a range of friction coefficients (μ). All calculation involved $\tilde{Q} = Q/(\mu P) = 0.99$ lateral force.



(a) Dissipation with full elastic coupling for $KR = 1$



(b) Errors in Normal traction p_{error} for $KR = 1$



(c) Errors in Lateral traction τ_{error} for $KR = 1$

Figure 6.5: For a rigid cylinder pressed inside a circular hole of twice radius, contact parameters such as Dissipation, Stick ratio, and errors in surface tractions are plotted against over a range of friction coefficients (μ) and five different lateral ratio \tilde{Q} .

non-dimensionalized contact parameters are independent of the mean curvature even with variation in friction coefficients.

Next, a contact problem – a rigid cylinder pressed inside the elastic hole twice its radius – is simulated with five different lateral load ratios (\tilde{Q}) over a range of friction coefficients. The dissipation value for GD is divided by dissipation value for FC to calculate a dissipation ratio. The ratio is plotted against the friction coefficients as shown in Fig. 6.5. The dissipation ratio increases with increasing friction coefficients for high lateral load ($\tilde{Q} = 0.99, 0.93$). But this ratio results in a concave up curve for low lateral load, as shown in Fig. 6.5. The dissipation ratio varies from 1.14 to 1.30 for the five lateral forces, concluding at least a 14% overestimation of dissipation calculated with decoupled approximation.

Errors in normal tractions increase with increasing friction coefficients and lateral load, as shown in Fig. 6.5b. Errors in lateral traction depend significantly on the decoupling approximations. For the GD case, error increases with increase in the coefficient of friction. The maximum value of error observed is 35%. But for the FD case, error in lateral tractions reduces for lower lateral ratios and increases for higher lateral ratios, as shown in Fig. 6.5c.

6.6 Discussion

Both qualitative and quantitative ramifications of the decoupling assumptions can be assessed on the basis of the simulations reported here. Shear tractions and stick ratios calculated using the Goodman decoupling approximation are consistently in good qualitative agreement with the fully coupled (correct) traction distributions. Dissipations and normal tractions remain the same for the Goodman decoupling and full decoupling approximations. As expected, the shear traction distributions associated with full decoupling bear little resemblance to the traction distributions predicted by the full coupling model or the Goodman decoupling model. The fully coupled analysis shows the contact patch shifting from side to side as lateral forces are applied. By construction, neither the Goodman's model or fully-decoupled analyses show any motion of the contact patch.

As expected from analyses of the underlying integral equations, the appropriately nondimension-

alized energy dissipation plots are independent of the geometrical parameter KR . The decoupling approximations almost always lead to over-predicting the dissipation. For the cases of Goodman decoupling and full decoupling, the log-log plots of dissipation vs shear load show slopes close to 3.0, consistent with Goodman's observation [32]. On the other hand, the fully coupled model yields slightly higher slopes, close to 3.15. For all three coupling treatments, the dissipation increases proportionally to the square of friction coefficient. Other nondimensional parameters such as stick-ratios, errors in the surface tractions also happen to be independent of KR .

The normalized normal traction is the same for GD and FD, but visibly distinguishable from FC. The errors in surface traction are sensitive to lateral force ratio and friction coefficients. Because increase in lateral force ratio or the friction coefficients causes high lateral traction in the contact region, the impact of the normal tractions for the fully coupled system and results in the higher normal traction error.

The errors in lateral traction are significantly different for Goodman decoupling and full decoupling. For the Goodman decoupling, errors in lateral traction increase with increase in lateral traction due to its qualitative similarity with fully coupled case. For full decoupling, small lateral force leads to small lateral traction which is different than lateral traction calculated for the fully coupled case. In some cases, this difference results in almost 100% error.

6.7 Summary of Effects of Elastic Decoupling Approximations

The research presented here assess the seriousness of compromises in accuracy that results from exploitation of the simplifying approximations of Goodman and of full decoupling. A few notable points are:

- Goodman decoupling approximation showed surprisingly good results in capturing the shape of lateral tractions and stick ratio. However, Goodman decoupling shows some serious errors in measuring dissipation and surface tractions. The Goodman decoupling does not predict the shift of contact region which is important for tribological analysis.
- Full decoupling approximation did not predict a proper lateral traction. However, it is no

worse than Goodman decoupling in estimating the dissipation and normal traction. It shows serious errors both quantitatively and qualitatively compared to the fully coupled case.

CHAPTER 7

CONCLUSION AND FUTURE RESEARCH

In this chapter, a brief summary of the dissertation is presented, highlighting the main achievements. Brief concluding remarks are provided with directions to continue this research work in the future.

7.1 Summary

The aim of this research was to develop a numerical test-bed to solve and analyze contact problems. A robust contact algorithm and an extremely fine discretization method are required to create numerical test-bed.

Contact Algorithm: To address this, a contact problem – a rigid indenter pressed against an elastic half-plane is analyzed where an elastic half-plane is discretized to create a compliance matrix. Applying the conventional algorithm showed issues with convergence, so a new contact algorithm – the Method of First Violation (MFV) is developed that showed robustness and fidelity with contact path. The conventional algorithm and MFV are compared and verified using analytical expressions for surface tractions, stick-ratio, and displacements.

The MFV's robustness was shown by employing a two-parameter Coulomb friction model, Dahl friction, and one-parameter Coulomb friction with a high coefficient of friction. For the same cases, a conventional algorithm would not converge or provide correct solutions. The path-dependent integrity of the MFV is shown through surface traction evolution during cyclic shear loading when the two-parameter friction model is employed. The computational efficiency of MFV is of the similar order to the conventional algorithm if optimal nominal load step is used.

Fine Mesh Strategy: A compliance matrix formulation is derived for two-dimensional circular elastic cylinders, disks, and holes in an infinite plane. Michell's Airy stress function is used with the Fourier series to calculate stresses and displacements inside and on the surface of an elastic body. First, radial and tangential displacements over the contacting surface are calculated by applying a unit radial and tangential force on a discretized interval for a circular disk or hole. This calculated

displacement basis is used as a column of compliance matrix, and other columns are assembled by the circular shifting of the displacement basis. The resulting polar compliance matrix is converted to Cartesian form through rotational transformations.

Contact problems of an elastic cylinder pressed against a rigid half-plane and a rigid cylinder pressed inside a circular hole are analyzed using compliance matrices. These compliance matrices with the MFV contact algorithm are verified with available analytical expressions of surface traction, stick ratio, stresses, and surface displacements. Another contact problem – Two identical elastic cylinders pressed against each other and sheared – is analyzed for two friction models (one-parameter Coulomb and two-parameter Coulomb) while employing Goodman decoupling approximation. Contact parameters such as surface traction, surface displacements, and stresses in and over the contacting surfaces are compared. The change in friction model caused a slight change in stress fields inside the contacting surfaces, and most of the differences are noticed in surface tractions, slip, and the location of maximum von-Mises stress.

Comparing Decoupling Approximations: Multiple contact problems are numerically simulated using MFV and the compliance matrix strategy. Five different contact geometries are designed using elastic cylinders, holes, and half-plane, where Goodman decoupling approximation and full decoupling approximations are employed along with full elastic coupling in contact problems. Numerical simulations are conducted over a range of lateral force ratios and friction coefficients. Contact parameters calculated from decoupling approximations are compared with corresponding full elastic coupling. Both qualitative and quantitative ramifications of the decoupling approximations are assessed, showing some serious differences between contact parameters.

7.2 Concluding Remarks

The frictional contact problems are notoriously complex and require a robust contact algorithm with an extremely fine discretization in the contact region for its analysis. These concerns are addressed by developing a robust contact algorithm – Method of first Violation – and deriving a compliance formulation for the two-dimensional disks, cylinders, and holes. These two developments provide

a robust test-bed to analyze the contact problems. This test-bed is used to compare the Goodman and full decoupling approximations with full coupling and to assess the level of accuracy and compromises due to these decoupling approximations. Now, this test-bed offers opportunities to explore other complex contact problems that were previously difficult or intractable.

7.3 Future Research

In the future, this research can be expanded in multiple directions. Some of these have been planned to be explored in the near future.

- Develop a similar compliance matrix formulation for other geometries such as annular disks and cams. A compliance formulation for annular disks or cylinders may require a similar approach with a little more complicated math.
- Employ other friction models on this test-bed and compare and correlate the numerical results with the experimental results of joints.
- Develop a formulation that can connect the finite element approach with compliance formulation of elastic bodies with circular contact profiles such as cams and gears. One would hope to explore the contact analysis through compliance formulation and predict the other important parameters outside the contact region through finite element analysis.
- Implement this extremely fine mesh for elastohydrodynamic lubricant contact and conduct contact analysis for contact problems such as rotating shafts and roller bearings.

APPENDICES

APPENDIX A

COMPLIANCE MATRIX FORMULATION FOR ELASTIC HALF-PLANE

Consider a rigid cylinder pressing an elastic half-plane with consequent normal pressure $p(x)$ and a lateral traction $\tau(x)$ as shown in Fig A.1. These distributed tractions result in the normal and lateral displacements $w(x)$ and $u(x)$ respectively, which can be calculated using Eqns. (A.1) and (A.2) [6, 35]. These expressions involve singular kernels and constants C_1 and C_2 representing arbitrary rigid body displacements.

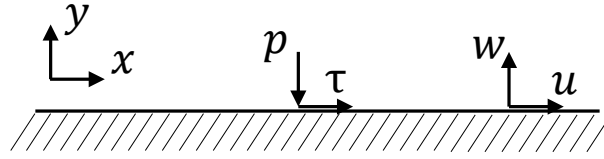


Figure A.1: Coordinates x, y ; tractions p, τ ; and displacements u, w on the surface of an elastic half-plane

$$w(x) = - \int \frac{p(\zeta)(\kappa + 1) \log |x - \zeta|}{4\pi\mu} d\zeta - \int \frac{\tau(\zeta)(\kappa - 1) \operatorname{sgn}(x - \zeta)}{8\mu} d\zeta + C_1 \quad (\text{A.1})$$

$$u(x) = - \int \frac{\tau(\zeta)(\kappa + 1) \log |x - \zeta|}{4\pi\mu} d\zeta + \int \frac{p(\zeta)(\kappa - 1) \operatorname{sgn}(x - \zeta)}{8\mu} d\zeta + C_2 \quad (\text{A.2})$$

These equations are the basis for creating the discretization method discussed below.

A.1 Discretization

In order to use numerical simulation to obtain insight into the mechanics taking place in a contact patch, it is necessary to have a very fine mesh in that region. In most general applications, this is done using finite element analysis where a fine mesh in the contact region requires meshing the full substrate structure with a grid that gradually increases in coarseness away from the contact patch. This involves a huge number of degrees of freedom that must be solved at each iteration of each load step. Though there are various flavors of efficiencies available, such as static reduction

of the degrees of freedom not in the region of the contact patch [23, 36], implementation of those efficiencies also involve tremendous computer resources and substantial compute time.

In the particular case where the elastic component is a half-plane, it is possible to formulate the problem so that the only degrees of freedom are the displacement and tractions on the surface of the half-plane in the vicinity of the region of contact.

With reference to Equations A.1 and A.2, we consider some set of N basis functions $\phi^k(x)$ such as those used in one-dimensional finite element analysis so that in the interval $(-R, R)$ containing the region of contact, we express our tractions in terms of those basis functions.

$$p(x) = \sum_{k=-M}^{k=M} \phi^k(x) p_k \quad \text{and} \quad \tau(x) = \sum_{k=-M}^{k=M} \phi^k(x) \tau_k \quad (\text{A.3})$$

where p_k and τ_k are the values of pressure and shear stress at at location x_k , respectively. In the development that follows, the shape functions used are disjoint step-functions constructed so as to serve as a partition of unity in $(-R, R)$. Implicit in the above definition is an assignment of $N = 2M + 1$ nodal locations:

$$x_k = 2 a k \quad \text{where} \quad a = R/N \quad (\text{A.4})$$

The step basis functions $\phi^k(x)$ are now defined as

$$\phi^k(x) = \begin{cases} 0 & \text{if } x \leq x_k - a \\ 1 & \text{if } x_k - a < x < x_k + a \\ 0 & \text{if } x \geq x_k + a \end{cases} \quad (\text{A.5})$$

The displacements $w_k^p(x)$, $u_k^p(x)$, $w_k^\tau(x)$, and $u_k^p(x)$ associated with these pressure basis functions are provided in [35] for the case of $k = 0$ and are presented in the below A.3. The remaining basis functions expressed in terms of $w_0^p(x)$, $u_0^p(x)$, $w_0^\tau(x)$, and $u_0^p(x)$:

$$\begin{aligned} w_k^p(x) &= w_0^p(x - x_k), & u_k^p(x) &= u_0^p(x - x_k), \\ w_k^\tau(x) &= w_0^\tau(x - x_k), & u_k^\tau(x) &= u_0^\tau(x - x_k) \end{aligned} \quad (\text{A.6})$$

These relationships are illustrated for $\phi_k(x)$ and $w_k^p(x)$ for $k = -1, 0, 1$ in Figure A.2, where normal displacement distribution also shifted by $+\Delta x$ or $-\Delta x$ on shifting the normal unit pressure.

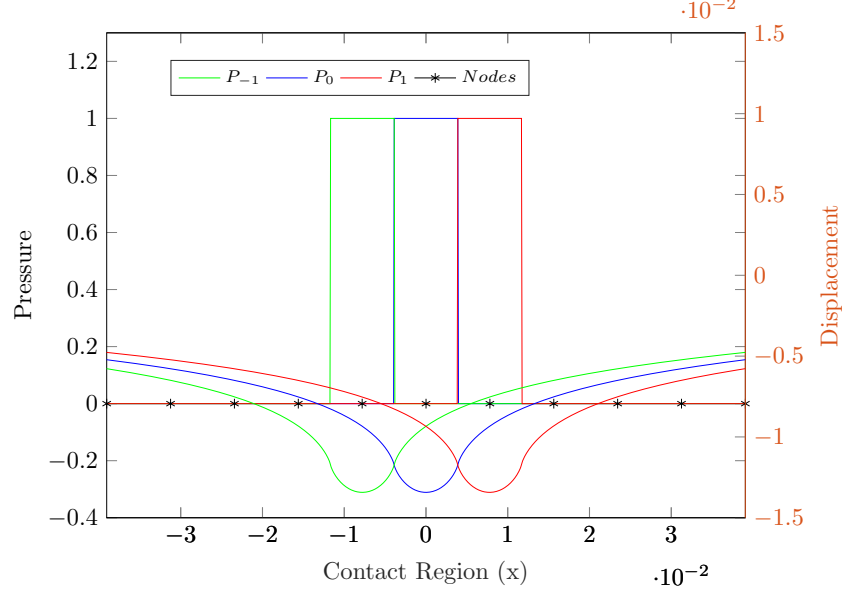


Figure A.2: Unit normal pressure and corresponding displacement on shifting by $-\Delta x$ and Δx

The displacements corresponding to Equation A.3 are

$$\begin{aligned}
 w(x) &= \sum_{k=-M}^{k=M} w_k^p(x) p_k + \sum_{k=-M}^{k=M} w_k^\tau(x) \tau_k + W_{tot} \\
 u(x) &= \sum_{k=-M}^{k=M} u_k^p(x) p_k + \sum_{k=-M}^{k=M} u_k^\tau(x) \tau_k + U_{tot}
 \end{aligned} \tag{A.7}$$

and W_{tot} and U_{tot} are yet unknown rigid body vertical and horizontal displacements, respectively.

A.2 Compliance Matrix

Evaluating Equation A.6 at the nodal locations ($\{x_k\}$) yields a compliance matrix for displacements in terms of tractions. In order to accommodate the unknown rigid body displacements W_{tot} and U_{tot} , it is necessary to add two force equilibrium equations

$$F_N = \sum_{k=-M}^{k=M} p_k \Delta x \quad \text{and} \quad F_L = \sum_{k=-M}^{k=M} \tau_k \Delta x \tag{A.8}$$

where $\Delta x = 2a$ and F_N and F_L are the net normal and lateral forces imposed on the half plane, respectively. All these relationships are shown in Equation A.9. It is assumed that at every step two of W_{tot} , U_{tot} , F_N , and F_L are known.

$$\left\{ \begin{array}{c} \vdots \\ w_n \\ \vdots \\ u_n \\ \vdots \\ P \\ Q \end{array} \right\} = \left[\begin{array}{cc|cc} C_{wp} & C_{w\tau} & 1 & 0 \\ & & \vdots & \vdots \\ C_{up} & C_{u\tau} & 0 & 1 \\ & & \vdots & \vdots \\ \hline \Delta x & \dots & 0 & 0 \\ 0 & \dots & \Delta x & 0 \end{array} \right] \left\{ \begin{array}{c} \vdots \\ p_n \\ \vdots \\ \tau_n \\ \vdots \\ W_{tot} \\ U_{tot} \end{array} \right\} \quad (\text{A.9})$$

A.3 Displacements Associated with Unit Normal Pressure and Unit Shear Traction Functions for $k = 0$

The displacements associated with the traction basis functions for pressure and shear are provided in [35]. The normal displacement due to unit normal pressure in $(-a, a)$ is

$$w_0^p(x) = \frac{-A}{2\pi} \left[(a+x) \ln \left(\frac{a+x}{a} \right)^2 + (a-x) \ln \left(\frac{a-x}{a} \right)^2 \right] \quad (\text{A.10})$$

for $x \in (-\infty, \infty)$

The lateral displacement due to unit pressure in $(-a, a)$ is¹.

$$u_0^p(x) = \begin{cases} -A\beta x & \text{for } x \in (-a, a) \\ -A\beta a \operatorname{sgn}(x) & \text{otherwise} \end{cases} \quad (\text{A.11})$$

The lateral displacement due to unit shear traction in the interval $(-a, a)$ is:

$$u_0^\tau(x) = \frac{A}{2\pi} \left[(a+x) \ln \left(\frac{a+x}{a} \right)^2 + (a-x) \ln \left(\frac{a-x}{a} \right)^2 \right] \quad (\text{A.12})$$

for $x \in (-\infty, \infty)$

The normal displacement due to unit shear traction in $(-a, a)$ is¹.

$$w_0^\tau(x) = \begin{cases} -A\beta x & \text{for } x \in (-a, a) \\ -A\beta a \operatorname{sgn}(x) & \text{otherwise} \end{cases} \quad (\text{A.13})$$

¹ Equations of lateral displacement due to normal pressure A.11 and normal displacement due to lateral traction A.13, differ by factor of two from the corresponding equations in "Mechanics of Elastic Contacts" [35] in chapter 14 at page 427. However, substituting these traction and displacement expressions into the integral equations of Chapter 2 of that book and of Chapter 12 of [6] indicate that the expressions used here are correct.

Above,

$$A = 2 \frac{1 - \nu^2}{E} \quad \text{and} \quad \beta = \frac{1 - 2\nu}{2(1 - \nu)} \quad (\text{A.14})$$

For plane strain $\kappa = 3 - 4\nu$, and $E = 2G(1 + \nu)$

$$A\beta = \frac{(\kappa - 1)}{4G} \quad (\text{A.15})$$

APPENDIX B

IMPLEMENTAION OF DAHL FRICTION MODEL WITH ALGORITHM-II (METHOD OF FIRST VIOLATION)

The rate-independent Dahl model can be compared to Coulomb friction model and has similarities to it as shown in the Fig. B.1. The Dahl model and Coulomb friction differ in the regime where force is less than f_c , the force necessary to cause sliding. In that regime the Dahl model provides a force evolution equation (Eq. 3.9) while Coulomb friction imposes a no-slip condition. The parameter σ is a contact stiffness associated with interface mechanics before slip. This differential relationship can be implemented numerically using a finite difference method with explicit integration. In the partial slip regime ($f < f_c$) the Dahl model becomes (Eq. B.1), which can be expressed in the simpler form of Eq. B.2.

$$\frac{f - f_0}{u - u_0} = \sigma \left| 1 - \frac{f_0}{\mu p_0} \operatorname{sgn}(u_0) \right|^\gamma \operatorname{sgn} \left(1 - \frac{f}{\mu p_0} \operatorname{sgn}(u_0) \right) \quad (\text{B.1})$$

$$\text{using, } K = \sigma \left| 1 - \frac{f_0}{\mu p_0} \operatorname{sgn}(u_0) \right|^\gamma \operatorname{sgn} \left(1 - \frac{f}{\mu p_0} \operatorname{sgn}(u_0) \right) \quad (\text{B.2})$$

$$f - Ku = f_0 - Ku_0$$

where, f_0 , u_0 and p_0 are the known friction force, lateral displacements, and normal pressure values of the last equilibrium configuration. σ and γ are the Dahl parameters. Quantities f and u are the

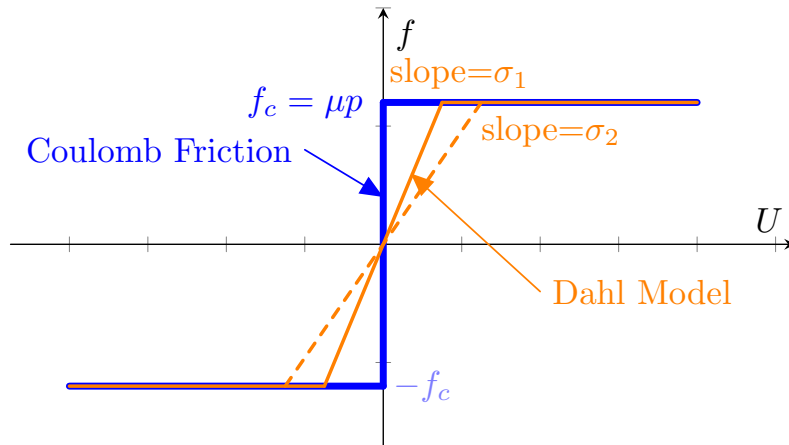


Figure B.1: Comparing Dahl friction model with Coulomb friction model.

friction force and lateral displacement, to be calculated for the end of the load step.

Nodal Statuses	Equality Constr.	Inequality Constr.
Contact and Partial slip	$\tau - Ku = \tau_0 - Ku_0, w = g$	$ \tau \leq f, p \geq 0$
Contact and Slip Right	$\tau = f, w = g$	$\dot{u} \geq 0, p \geq 0$
Contact and Slip Left	$\tau = -f, w = g$	$\dot{u} \leq 0, p \geq 0$
Not-in-Contact	$p = 0, \tau = 0$	$w \leq g$

Table B.1: Equality and inequality constraints for Dahl friction model.

The equality and inequality constraints are similar to those of Coulomb friction except in the region of partial slip (which corresponds to the stick region for Coulomb friction). The equality constraints for each node (B.1) can be incorporated into a system matrix similar to Eq. 2.2 and Algorithm-II can be applied with few other changes. Among those changes is resetting the shear traction of sliding nodes when normal traction decreases, also, because of the explicit formulation of the constitutive equation, accuracy and stability require use of small times steps as well calculation of those that cause transition of node status.

APPENDIX C

MICHELL COEFFICIENTS FOR A SOLID ELASTIC DISK WITH NO HOLES

The Michell Airy stress function for a solid elastic disk after discarding the secular and multi-value terms is following:

$$\begin{aligned}
 \Phi_0(r, \theta) = & A_{01}r^2 + A_{04}\theta + A_{11}r^3 \cos(\theta) + A_{12} \left[r \log(r) \cos(\theta) - \frac{\kappa + 1}{\kappa - 1} r\theta \sin(\theta) \right] \\
 & + B_{11}r^3 \sin(\theta) + B_{12} \left[r \log(r) \sin(\theta) + \frac{\kappa + 1}{\kappa - 1} r\theta \cos(\theta) \right] \\
 & + \sum_{n=2}^{\infty} [(A_{n1}r^{n+2} + A_{n3}r^n) \cos(n\theta) + (B_{n1}r^{n+2} + B_{n3}r^n) \sin(n\theta)]
 \end{aligned} \tag{C.1}$$

C.1 Stresses and Displacements

The stresses and displacements are calculated for the stress function Eq. C.1 using Michell Table ???. Radial stress σ_{rr} and tangential stress $\sigma_{r\theta}$ at $r = R$ results in the radial and tangential tractions applied on the surface of the disk and are sufficient to formulate a compliance matrix. Thus, circumferential stress $\sigma_{\theta\theta}$ is not required for calculation.

$$\begin{aligned}
 \sigma_{rr} = & 2A_{01} + \left[2rA_{11} + A_{12} \left(\frac{1}{r} - \frac{(\kappa + 1) 2}{(\kappa - 1) r} \right) \right] \cos(\theta) + \left[2rB_{11} + B_{12} \left(\frac{1}{r} + \frac{(\kappa + 1) (-2)}{(\kappa - 1) r} \right) \right] \sin(\theta) \\
 & + \sum_{n=2}^{\infty} [(A_{n1}(-(n + 1)(n - 2)r^n) + A_{n3}(-n(n - 1)r^{n-2}))] \cos(n\theta) \\
 & + \sum_{n=2}^{\infty} [(B_{n1}(-(n + 1)(n - 2)r^n) + B_{n3}(-n(n - 1)r^{n-2}))] \sin(n\theta) \\
 \sigma_{r\theta} = & \frac{A_{04}}{r^2} + \left[2rA_{11} + A_{12} \frac{1}{r} \right] \sin(\theta) + \left[2rB_{11} + B_{12} \frac{1}{r} \right] \cos(\theta) \\
 & + \sum_{n=2}^{\infty} [(A_{n1}(n(n + 1)r^n) + A_{n3}(n(n - 1)r^{n-2}))] \sin(n\theta) \\
 & + \sum_{n=2}^{\infty} [(B_{n1}(-n(n + 1)r^n) + B_{n3}(-n(n - 1)r^{n-2}))] \cos(n\theta)
 \end{aligned} \tag{C.2}$$

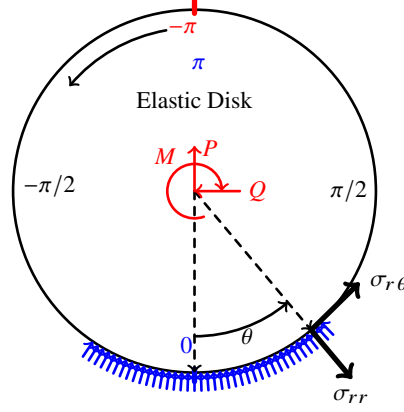


Figure C.1: Stress distribution on the solid disk is equilibrated with forces and moment near the center.

Stresses distributed on the surface of the disk due to contact should be equilibrated by applying the forces on the disk away from the contact or by applying the forces and moment near the center of the disk as shown in Fig. C.1.

A normal force per unit length (P) is equilibrated with components of radial (σ_{rr}) and tangential ($\sigma_{r\theta}$) stress as shown in Eq. C.3. Expressions of stresses from Eq. C.2 are substituted in Eq. C.3 and solved. The expression results with only Michell coefficient (A_{12}) to equilibrate the normal force (P).

$$\begin{aligned}
 P &= \int_{-\pi}^{\pi} (\sigma_{rr} \cos \theta - \sigma_{r\theta} \sin \theta) R d\theta \\
 P &= \left[2R^2 A_{11} + A_{12} \left(1 - \frac{(\kappa + 1)2}{(\kappa - 1)} \right) \right] \pi - [2R^2 A_{11} + A_{12}] \pi \\
 P &= -2A_{12}\pi \left(\frac{(\kappa + 1)}{(\kappa - 1)} \right)
 \end{aligned} \tag{C.3}$$

Similarly, lateral force per unit length (Q) is equilibrated with components of radial and tangential stress as shown in C.4. The expression results with only Michell coefficient (B_{12}) to equilibrate the lateral force (Q).

$$\begin{aligned}
 Q &= \int_{-\pi}^{\pi} (\sigma_{rr} \sin \theta + \sigma_{r\theta} \cos \theta) R d\theta \\
 Q &= \left[2R^2 B_{11} + B_{12} \left(1 - \frac{(\kappa + 1)2}{(\kappa - 1)} \right) \right] \pi + [2R^2 B_{11} + B_{12}] \pi \\
 Q &= -2B_{12}\pi \left(\frac{(\kappa + 1)}{(\kappa - 1)} \right)
 \end{aligned} \tag{C.4}$$

A moment at the center of disk results because of the tangential stress ($\sigma_{r\theta}$) at the contact surface which is equilibrated using Eq. C.5. The moment expression results with Michell coefficient (A_{04}).

$$M = \int_{-\pi}^{\pi} (\sigma_{r\theta})R^2 d\theta \quad (C.5)$$
$$M = 2\pi A_{04}$$

Three Michell coefficients A_{12}, B_{12} , and A_{04} are sufficient to equilibrate the forces and moment applied on an elastic circular disk.

To calculate displacement at the surface, first strains at the contact surface are calculated using Hook's law and stresses shown in Eq. C.2. Later, strains are integrated over the length of the contact surface that results in displacements and some constant of integration. The procedure is explained in Chapter 9 (especially section 9.2) of Elasticity book [6]. As pointed out in the procedure, three constants of integration result from derivation. Two constants represent the rigid body translation and one constant represents rigid body rotation. Displacements expressions (Eq. C.6) are without these rigid body constants. One would need to consider the rigid body displacements during the calculation as shown in the section 4.3.

$$\begin{aligned}
2\mu U_r &= A_{01}(\kappa - 1)r \\
&+ \left[A_{11}(\kappa - 2)r^2 + A_{12}\frac{1}{2} \left(((\kappa - 1)\ln(r) - 1) - \frac{(\kappa + 1)}{(\kappa - 1)}((\kappa + 1)\ln(r) - 1) \right) \right] \cos(\theta) \\
&+ \left[B_{11}(\kappa - 2)r^2 + B_{12}\frac{1}{2} \left(((\kappa - 1)\ln(r) - 1) + \frac{(\kappa + 1)}{(\kappa - 1)}(1 - (\kappa + 1)\ln(r)) \right) \right] \sin(\theta) \\
&+ \sum_{n=2}^{\infty} \left[(A_{n1}((\kappa - n - 1)r^{n+1}) + A_{n3}((-n)r^{n-1})) \right] \cos(n\theta) \\
&+ \sum_{n=2}^{\infty} \left[(B_{n1}((\kappa - n - 1)r^{n+1}) + B_{n3}((-n)r^{n-1})) \right] \sin(n\theta) \\
2\mu U_\theta &= -A_{04}\frac{1}{r} \\
&+ \left[A_{11}(\kappa + 2)r^2 + A_{12}\frac{1}{2} \left((-1 + (\kappa + 1)\ln(r)) - \frac{(\kappa + 1)}{(\kappa - 1)}(-1 - (\kappa + 1)\ln(r)) \right) \right] \sin(\theta) \\
&+ \left[-B_{11}(\kappa + 2)r^2 + B_{12}\frac{1}{2} \left((1 + (\kappa - 1)\ln(r)) + \frac{(\kappa + 1)}{(\kappa - 1)}(-1 - (\kappa + 1)\ln(r)) \right) \right] \cos(\theta) \\
&+ \sum_{n=2}^{\infty} \left[(A_{n1}((\kappa + n + 1)r^{n+1}) + A_{n3}(nr^{n-1})) \right] \sin(n\theta) \\
&+ \sum_{n=2}^{\infty} \left[(B_{n1}(-(\kappa + n + 1)r^{n+1}) + B_{n3}(-nr^{n-1})) \right] \cos(n\theta)
\end{aligned} \tag{C.6}$$

C.2 Michell Terms for Unit Radial/Tangential Load

The unit pressure ϕ_0 is applied radially in the interval centered at node $\theta = 0$ generating a non-zero radial stress and a zero tangential stress. Trigonometric terms from the Eqs.C.2 and 4.10 are equated and result in the linear equations in A's and B's shown in C.7.

$\sigma_{rr} = \phi_0(\theta)$	$\sigma_{r\theta} = 0$
$2A_{01} = \frac{\Delta\theta}{2\pi}$	$A_{04}/r^2 = 0$
$2rA_{11} + A_{12}\left(\frac{1}{r} - \frac{(\kappa+1)2}{(\kappa-1)r}\right) = \frac{2}{\pi} \sin\left(\frac{\Delta\theta}{2}\right)$	$2rA_{11} + A_{12}\frac{1}{r} = 0$
$2rB_{11} + B_{12}\left(\frac{1}{r} - \frac{(\kappa+1)2}{(\kappa-1)r}\right) = 0$	$2rB_{11} + B_{12}\frac{1}{r} = 0$
$(A_{n1}(-(n+1)(n-2)r^n) - A_{n3}(n(n-1)r^{n-2})) = \frac{2}{n\pi} \sin\left(\frac{n\Delta\theta}{2}\right)$	$(A_{n1}(n(n+1)r^n) + A_{n3}(n(n-1)r^{n-2})) = 0$
$(B_{n1}(-(n+1)(n-2)r^n) - B_{n3}(n(n-1)r^{n-2})) = 0$	$(B_{n1}(-n(n+1)r^n) - B_{n3}(n(n-1)r^{n-2})) = 0$

(C.7)

Similarly, the unit traction ϕ_0 is applied tangentially at same interval creating a non-zero tangential stress and a zero radial stress. This results in the linear equations shown in C.8.

$\sigma_{rr} = 0$	$\sigma_{r\theta} = \phi_0(\theta)$
$2A_{01} = 0$	$A_{04}/r^2 = \frac{\Delta\theta}{2\pi}$
$2rA_{11} + A_{12}\left(\frac{1}{r} - \frac{(\kappa+1)2}{(\kappa-1)r}\right) = 0$	$2rA_{11} + A_{12}\frac{1}{r} = 0$
$2rB_{11} + B_{12}\left(\frac{1}{r} - \frac{(\kappa+1)2}{(\kappa-1)r}\right) = 0$	$2rB_{11} + B_{12}\frac{1}{r} = \frac{2}{\pi} \sin\left(\frac{\Delta\theta}{2}\right)$
$(A_{n1}(-(n+1)(n-2)r^n) - A_{n3}(n(n-1)r^{n-2})) = 0$	$(A_{n1}(n(n+1)r^n) + A_{n3}(n(n-1)r^{n-2})) = 0$
$(B_{n1}(-(n+1)(n-2)r^n) - B_{n3}(n(n-1)r^{n-2})) = 0$	$(B_{n1}(-n(n+1)r^n) - B_{n3}(n(n-1)r^{n-2})) = \frac{2}{n\pi} \sin\left(\frac{n\Delta\theta}{2}\right)$

(C.8)

These linear Eqs. C.7 and C.8 are solved separately for A 's and B 's terms of radial and tangential load respectively (at the surface $r = R$), and the resulting values of A 's and B 's are shown in the Tab. 4.2.

C.2.1 Stresses and Displacements inside the Circular Disk

For a unit radial stress on the interval about $\theta = 0$, stresses and displacement inside the disk are the following:

$$\begin{aligned}
\sigma_{rr}(r, \theta) &= \frac{\Delta\theta}{2\pi} + \frac{(\kappa - 1)r^2 + (\kappa + 3)R^2}{\pi(\kappa + 1)Rr} \sin(\Delta\theta/2) \cos(\theta) \\
&\quad + \sum_{n=1}^{Harm} \frac{r^{n-2}(nR^2 + 2r^2 - nr^2)}{\pi nR^n} \sin(n\Delta\theta/2) \cos(n\theta) \\
\sigma_{\theta\theta}(r, \theta) &= \frac{\Delta\theta}{2\pi} + \frac{(\kappa - 1)(3r^2 - R^2)}{\pi(\kappa + 1)Rr} \sin(\Delta\theta/2) \cos(\theta) \\
&\quad + \sum_{n=1}^{Harm} \frac{r^{n-2}((n + 2)r^2 - nR^2)}{\pi nR^n} \sin(n\Delta\theta/2) \cos(n\theta) \\
\sigma_{r\theta}(r, \theta) &= \frac{(\kappa - 1)(r^2 - R^2)}{\pi(\kappa + 1)Rr} \sin(\Delta\theta/2) \sin(\theta) \\
&\quad + \sum_{n=1}^{Harm} \frac{r^{n-2}(r^2 - R^2)}{\pi R^n} \sin(n\Delta\theta/2) \sin(n\theta) \\
2\mu U_r(r, \theta) &= \frac{r(\kappa - 1)\Delta\theta}{4\pi} + \frac{((\kappa^2 - 3\kappa + 2)r^2 + 4\kappa R^2 \ln(r))}{2\pi(\kappa + 1)R} \sin\left(\frac{\Delta\theta}{2}\right) \cos(\theta) \\
&\quad + \sum_{n=1}^{Harm} \frac{r^{n-1}((\kappa - n - 1)(n - 1)r^2 + (n^2 + n)R^2)}{n(n^2 - 1)\pi R^n} \sin\left(\frac{n\Delta\theta}{2}\right) \cos(n\theta) \\
2\mu U_\theta(r, \theta) &= \frac{(\kappa^2 + \kappa - 2)r^2 - 4(1 + \kappa \ln(R))R^2}{2\pi(\kappa + 1)R} \sin\left(\frac{\Delta\theta}{2}\right) \sin(\theta) \\
&\quad + \sum_{n=1}^{Harm} \frac{r^{n-1}((\kappa + n + 1)(n - 1)r^2 - (n^2 + n)R^2)}{n(n^2 - 1)\pi R^n} \sin\left(\frac{n\Delta\theta}{2}\right) \sin(n\theta)
\end{aligned} \tag{C.9}$$

For unit tangential stress at $\theta = 0$, stresses and displacements inside the disk are the following:

$$\begin{aligned}
\sigma_{rr}(r, \theta) &= -\frac{(\kappa + 3)(r^2 - R^2)}{\pi(\kappa + 1)Rr} \sin(\Delta\theta/2) \sin(\theta) \\
&\quad + \sum_{n=1}^{Harm} \frac{r^{n-2}(n-2)(r^2 - R^2)}{\pi n R^n} \sin(n\Delta\theta/2) \sin(n\theta) \\
\sigma_{\theta\theta}(r, \theta) &= -\frac{(3(\kappa + 3)r^2 + (\kappa - 1)R^2)}{\pi(\kappa + 1)Rr} \sin(\Delta\theta/2) \sin(\theta) \\
&\quad + \sum_{n=1}^{Harm} \frac{r^{n-2}((n-2)R^2 - (n+2)r^2)}{\pi n R^n} \sin(n\Delta\theta/2) \sin(n\theta) \\
\sigma_{r\theta}(r, \theta) &= \frac{\Delta\theta}{2\pi} + \frac{(\kappa + 3)r^2 + (\kappa - 1)R^2}{\pi(\kappa + 1)Rr} \sin(\Delta\theta/2) \cos(\theta) \\
&\quad + \sum_{n=1}^{Harm} \frac{r^{n-2}(nr^2 + 2R^2 - nR^2)}{\pi n R^n} \sin(n\Delta\theta/2) \cos(n\theta) \\
2\mu U_r(r, \theta) &= \frac{((\kappa^2 - \kappa + 6)r^2 + 4\kappa R^2 \ln(r))}{2\pi(\kappa + 1)R} \sin\left(\frac{\Delta\theta}{2}\right) \sin(\theta) \\
&\quad + \sum_{n=1}^{Harm} \frac{r^{n-1}((n^2 + \kappa - n\kappa - 1)r^2 + (2 + n - n^2)R^2)}{n(n^2 - 1)\pi R^n} \sin\left(\frac{n\Delta\theta}{2}\right) \sin(n\theta) \\
2\mu U_\theta(r, \theta) &= \frac{r\Delta\theta}{2\pi} + \frac{(\kappa^2 + 5\kappa + 6)r^2 + 4(1 + \kappa \ln(R))R^2}{2\pi(\kappa + 1)R} \sin\left(\frac{\Delta\theta}{2}\right) \cos(\theta) \\
&\quad + \sum_{n=1}^{Harm} \frac{r^{n-1}((\kappa + n + 1)(n - 1)r^2 + (2 - n^2 + n)R^2)}{n(n^2 - 1)\pi R^n} \sin\left(\frac{n\Delta\theta}{2}\right) \cos(n\theta)
\end{aligned} \tag{C.10}$$

Due to the elastic nature of the problem, the stress calculated using each contacting node can be summed to get the final stresses or displacements.

APPENDIX D

MICHELL COEFFICIENTS FOR AN INFINITE ELASTIC PLANE WITH A CIRCULAR HOLE

The Michell Airy stress function for a hole in an infinite elastic plane after discarding the secular and multi-value terms is following:

$$\begin{aligned}
 \Phi_0(r, \theta) = & A_{01}r^2 + A_{03} \ln(r) + A_{04}\theta + A_{23}r^2 \cos(\theta) + B_{23}r^2 \sin(\theta) \\
 & + A_{12} \left[r \log(r) \cos(\theta) - \frac{\kappa + 1}{\kappa - 1} r\theta \sin(\theta) \right] + A_{13}r\theta \cos(\theta) \\
 & + B_{12} \left[r \log(r) \sin(\theta) + \frac{\kappa + 1}{\kappa - 1} r\theta \cos(\theta) \right] + B_{13}r\theta \sin(\theta) \\
 & + \sum_{n=2}^{\infty} \left[(A_{n2}r^{2-n} + A_{n4}r^{-n}) \cos(n\theta) + (B_{n2}r^{2-n} + B_{n4}r^{-n}) \sin(n\theta) \right]
 \end{aligned} \tag{D.1}$$

D.1 Stresses and Displacements

The stresses and displacements are calculated for the stress function Eq. D.1 using Table ??.

$$\begin{aligned}
 \sigma_{rr} = & 2A_{01} + \frac{A_{03}}{R^2} + \left[A_{12} \left(\frac{1}{r} - \frac{(\kappa + 1) 2}{(\kappa - 1) r} \right) + A_{14} \frac{-2}{r^3} \right] \cos(\theta) + \left[B_{12} \left(\frac{1}{r} + \frac{(\kappa + 1) -2}{(\kappa - 1) r} \right) + B_{14} \frac{-2}{r^3} \right] \sin(\theta) \\
 & + A_{23}(-2) \cos(2\theta) + \sum_{n=2}^{\infty} \left[(A_{n2}(-(n-1)(n+2)r^{-n}) + A_{n4}(-n(n+1)r^{-n-2})) \right] \cos(n\theta) \\
 & + B_{23}(-2) \sin(2\theta) + \sum_{n=2}^{\infty} \left[(B_{n2}(-(n-1)(n+2)r^{-n}) + B_{n4}(-n(n+1)r^{-n-2})) \right] \sin(n\theta) \\
 \sigma_{r\theta} = & \frac{A_{04}}{r^2} + \left[A_{12} \frac{1}{r} + A_{14} \frac{-2}{r^3} \right] \sin(\theta) + \left[B_{12} \frac{1}{r} + B_{14} \frac{-2}{r^3} \right] \cos(\theta) \\
 & + A_{23}2 \sin(2\theta) + \sum_{n=2}^{\infty} \left[(A_{n2}(-n(n-1)r^{-n}) + A_{n4}(-n(n+1)r^{-n-2})) \right] \sin(n\theta) \\
 & + B_{23}(-2) \cos(2\theta) + \sum_{n=2}^{\infty} \left[(B_{n2}(n(n-1)r^{-n}) + B_{n3}(n(n+1)r^{-n-2})) \right] \cos(n\theta)
 \end{aligned} \tag{D.2}$$

From the above Eq. D.2, stresses can be non-zero at $r = \infty$ and can have some initial stresses in the elastic infinite plane (see Eq. D.3). For the known values of initial stress at $r = \infty$, A_{01}, A_{23} and B_{23} can be calculated through Eq. D.3 and used for further calculation. For this case, no initial stress in infinite plane is assumed which results in ($\{A_{01}, A_{23}, B_{23}\} = 0$). There is no loss of generality in setting stress to zero at infinity. As any displacements and stresses in the infinite plane can be superposed with the solution due to the elastic nature of the infinite plane.

$$\begin{aligned}\sigma_{rr}(\infty, \theta) &= 2A_{01} - 2A_{23} \cos(\theta) - 2B_{23} \sin(\theta) \\ \sigma_{r\theta}(\infty, \theta) &= 2A_{23} \sin(\theta) - 2B_{23} \cos(\theta) \\ \sigma_{\theta\theta}(\infty, \theta) &= 2A_{01} + 2A_{23} \cos(\theta) + 2B_{23} \sin(\theta)\end{aligned}\tag{D.3}$$

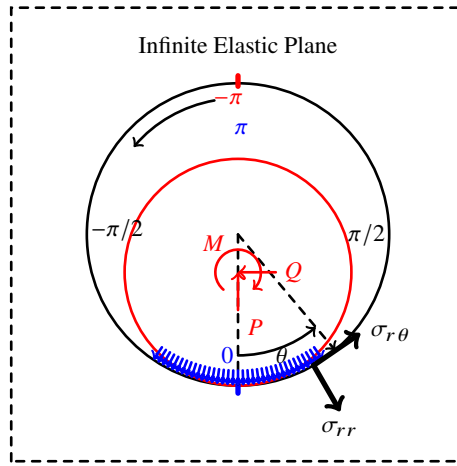


Figure D.1: Stress distribution on the hole should be equilibrated with forces and moment applied on the indenter.

Stresses distributed on the surface of the hole due to contact (shown in Fig. D.1) should be equilibrated by the forces and moment applied on the indenter that is pressing inside the hole.

A normal force per unit length (P) is equilibrated with components of radial (σ_{rr}) and tangential ($\sigma_{r\theta}$) stress as shown in Eq. D.4. The expression results with only Michell coefficient (A_{12}) to equilibrate the normal force (P).

$$\begin{aligned}
P &= \int_{-\pi}^{\pi} (\sigma_{rr} \cos \theta - \sigma_{r\theta} \sin \theta) R d\theta \\
P &= \left[-2A_{14} \frac{1}{R^2} + A_{12} \left(1 - \frac{(\kappa+1)2}{(\kappa-1)} \right) \right] \pi - \left[-2A_{14} \frac{1}{R^2} + A_{12} \right] \pi \\
P &= -2A_{12} \pi \left(\frac{(\kappa+1)}{(\kappa-1)} \right)
\end{aligned} \tag{D.4}$$

Similarly, lateral force per unit length (Q) is equilibrated with components of radial and tangential stress as shown in D.5. The expression results with only Michell coefficient (B_{12}) to equilibrate the lateral force (Q).

$$\begin{aligned}
Q &= \int_{-\pi}^{\pi} (\sigma_{rr} \sin \theta + \sigma_{r\theta} \cos \theta) R d\theta \\
Q &= \left[2B_{14} \frac{1}{R^2} + B_{12} \left(1 - \frac{(\kappa+1)2}{(\kappa-1)} \right) \right] \pi + \left[2B_{14} \frac{1}{R^2} + B_{12} \right] \pi \\
Q &= -2B_{12} \pi \left(\frac{(\kappa+1)}{(\kappa-1)} \right)
\end{aligned} \tag{D.5}$$

A moment at the center of the indenter results due to the tangential stress ($\sigma_{r\theta}$) at the contact surface which is equilibrated using Eq. D.6. The moment expression results with Michell coefficient (A_{04}).

$$\begin{aligned}
M &= \int_{-\pi}^{\pi} (\sigma_{r\theta}) R^2 d\theta \\
M &= 2\pi A_{04}
\end{aligned} \tag{D.6}$$

Three Michell coefficients A_{12}, B_{12} , and A_{04} are sufficient to equilibrate the contact stresses on the circular hole similar to the case of solid elastic disk. Note that these Michell coefficients are common coefficients both for a solid elastic disk and for a circular hole in an infinite elastic plane. Other Michell coefficients do not affect the forces and moment applied on the rigid or elastic indenter body.

Similar to the previous appendix C.1, the displacements are calculated by first calculating strains from stresses and later integrating strains over the length of the contact surface that result in displacements expression shown in Eq. D.7 and three constant of integration. The procedure is explained in Chapter 9 (especially section 9.2) of Elasticity [6]. Two constants represent the rigid body translation and one constant represents rigid body rotation. One should consider these rigid body displacements during the calculations.

$$\begin{aligned}
2\mu U_r &= A_{03} \frac{-1}{r} + \sum_{n=2}^{\infty} [(A_{n2}((\kappa + n - 1)r^{-n+1}) + A_{n4}((n)r^{-n-1}))] \cos(n\theta) \\
&+ \sum_{n=2}^{\infty} [(B_{n2}((\kappa + n - 1)r^{-n+1}) + B_{n4}((n)r^{-n-1}))] \sin(n\theta) \\
&+ \left[A_{14}(1/r^2) + A_{12} \frac{1}{2} \left(((\kappa - 1) \ln(r) - 1) - \frac{(\kappa + 1)}{(\kappa - 1)} ((\kappa + 1) \ln(r) - 1) \right) \right] \cos(\theta) \\
&+ \left[B_{14}(1/r^2) + B_{12} \frac{1}{2} \left(((\kappa - 1) \ln(r) - 1) + \frac{(\kappa + 1)}{(\kappa - 1)} (1 - (\kappa + 1) \ln(r)) \right) \right] \sin(\theta) \\
2\mu U_\theta &= -A_{04} \frac{1}{r} + \sum_{n=2}^{\infty} [(A_{n2}(-(\kappa - n - 1)r^{-n+1}) + A_{n4}(nr^{-n-1}))] \sin(n\theta) \\
&+ \sum_{n=2}^{\infty} [(B_{n2}((\kappa - n + 1)r^{n+1}) + B_{n4}(-nr^{-n-1}))] \cos(n\theta) \\
&+ \left[A_{14}(1/r^2) + A_{12} \frac{1}{2} \left((-1 + (\kappa + 1) \ln(r)) - \frac{(\kappa + 1)}{(\kappa - 1)} (-1 - (\kappa + 1) \ln(r)) \right) \right] \sin(\theta) \\
&+ \left[-B_{14}(1/r^2) + B_{12} \frac{1}{2} \left((1 + (\kappa - 1) \ln(r)) + \frac{(\kappa + 1)}{(\kappa - 1)} (-1 - (\kappa + 1) \ln(r)) \right) \right] \cos(\theta)
\end{aligned} \tag{D.7}$$

D.2 Michell Terms for Unit Radial/Tangential load

The unit pressure ϕ_0 is applied radially on the interval centered at node $\theta = 0$ generating non-zero radial stress and zero tangential stress. Trigonometric terms from the Eqs.D.2 and 4.10 are equated and result in the linear equations in A's and B's shown in D.8.

$\sigma_{rr} = \phi_0(\theta)$	$\sigma_{r\theta} = 0$
$A_{03} \frac{1}{r^2} = \Delta\theta/(2\pi)$	$A_{04} \frac{1}{r^2} = 0$
$A_{12} \left(\frac{1}{r} - \frac{(\kappa + 1)}{(\kappa - 1)} \frac{2}{r} \right) - A_{14} \frac{2}{r^3} = \frac{2}{\pi} \sin\left(\frac{\Delta\theta}{2}\right)$	$A_{12} \frac{1}{r} - A_{14} \frac{2}{r^3} = 0$
$B_{12} \left(\frac{1}{r} - \frac{(\kappa + 1)}{(\kappa - 1)} \frac{2}{r} \right) + B_{14} \frac{-2}{r^3} = 0$	$B_{12} \frac{1}{r} - B_{14} \frac{2}{r^3} = 0$
$A_{n2}(-(n-1)(n+2)r^{-n}) + A_{n4}(-n(n+1)r^{-n-2}) = \frac{2}{n\pi} \sin(n\Delta\theta/2)$	$(A_{n2}(-n(n-1)r^{-n}) + A_{n4}(-n(n+1)r^{-n-2})) = 0$
$B_{n2}(-(n-1)(n+2)r^{-n}) + B_{n4}(-n(n+1)r^{-n-2}) = 0$	$(B_{n2}(n(n-1)r^{-n}) + B_{n4}(n(n+1)r^{-n-2})) = 0$

(D.8)

Similarly, the unit traction ϕ_0 is applied tangentially on the interval about node $\theta = 0$ creating non-zero tangential stress and zero radial stress. This results in the linear equations shown in D.9.

$\sigma_{rr} = 0$	$\sigma_{r\theta} = \phi_0(\theta)$
$A_{03} \frac{1}{r^2} = 0$	$A_{04} \frac{1}{r^2} = \Delta\theta/(2\pi)$
$A_{12} \left(\frac{1}{r} - \frac{(\kappa+1)}{(\kappa-1)} \frac{2}{r} \right) + A_{14} \frac{-2}{r^3} = 0$	$A_{12} \frac{1}{r} + A_{14} \frac{-2}{r^3} = 0$
$B_{12} \left(\frac{1}{r} + \frac{(\kappa+1)}{(\kappa-1)} \frac{-2}{r} \right) + B_{14} \frac{-2}{r^3} = 0$	$B_{12} \frac{1}{r} + B_{14} \frac{-2}{r^3} = \frac{2}{\pi} \sin(\Delta\theta/2)$
$A_{n2}(-n(n-1)(n+2)r^{-n}) + A_{n4}(-n(n+1)r^{-n-2}) = 0$	$(A_{n2}(-n(n-1)r^{-n}) + A_{n4}(-n(n+1)r^{-n-2})) = 0$
$B_{n2}(-n(n-1)(n+2)r^{-n}) + B_{n4}(-n(n+1)r^{-n-2}) = 0$	$(B_{n2}(n(n-1)r^{-n}) + B_{n4}(n(n+1)r^{-n-2})) = \frac{2}{n\pi} \sin(n\Delta\theta/2)$

(D.9)

These linear Eqs. D.8 and D.9 are solved separately for A 's and B 's terms of radial and tangential load respectively (at the inner surface $r = R$), and the resulting values of A 's and B 's are shown in the Tab. 4.3.

D.2.1 Stresses and Displacements inside the Circular Hole

For a unit radial stress on $\theta = 0$, stresses and displacement inside the infinite plane of the hole are following:

$$\begin{aligned}
\sigma_{rr}(r, \theta) &= \frac{\Delta\theta}{2\pi} + \frac{R((\kappa + 3)r^2 + (\kappa - 1)R^2)}{\pi(\kappa + 1)r^3} \sin(\Delta\theta/2) \cos(\theta) \\
&\quad + \sum_{n=1}^{Harm} \frac{R^n(nr^2 + 2r^2 - nR^2)}{\pi nr^{n+2}} \sin(n\Delta\theta/2) \cos(n\theta) \\
\sigma_{\theta\theta}(r, \theta) &= -\frac{\Delta\theta}{2\pi} - \frac{(\kappa - 1)(r^2 + R^2)R}{\pi(\kappa + 1)r^3} \sin(\Delta\theta/2) \cos(\theta) \\
&\quad - \sum_{n=1}^{Harm} \frac{R^n((n - 2)r^2 - nR^2)}{\pi nr^{n+2}} \sin(n\Delta\theta/2) \cos(n\theta) \\
\sigma_{r\theta}(r, \theta) &= -\frac{(\kappa - 1)(r^2 - R^2)R}{\pi(\kappa + 1)r^3} \sin(\Delta\theta/2) \sin(\theta) \\
&\quad + \sum_{n=1}^{Harm} \frac{R^n(r^2 - R^2)}{\pi r^{n+2}} \sin(n\Delta\theta/2) \sin(n\theta) \\
2\mu U_r(r, \theta) &= -\frac{r\Delta\theta}{2\pi} - \frac{R(2r^2 + (\kappa - 1)R^2 - 4\kappa R^2 \ln(r))}{2\pi(\kappa + 1)r^2} \sin\left(\frac{\Delta\theta}{2}\right) \cos(\theta) \\
&\quad - \sum_{n=1}^{Harm} \frac{R^n((\kappa + n - 1)(n + 1)r^2 - (n^2 - n)R^2)}{n(n^2 - 1)\pi r^{n+1}} \sin\left(\frac{n\Delta\theta}{2}\right) \cos(n\theta) \\
2\mu U_\theta(r, \theta) &= -\frac{(\kappa - 1)R^3 + 2(1 + 2\kappa \ln(R))Rr^2}{2\pi(\kappa + 1)r^2} \sin\left(\frac{\Delta\theta}{2}\right) \sin(\theta) \\
&\quad + \sum_{n=1}^{Harm} \frac{R^n((\kappa - n + 1)(n + 1)r^2 + (n^2 - n)R^2)}{n(n^2 - 1)\pi r^{n+1}} \sin\left(\frac{n\Delta\theta}{2}\right) \sin(n\theta)
\end{aligned} \tag{D.10}$$

For unit tangential stress at $\theta = 0$, stresses and displacements inside the infinite plane of the

hole are following:

$$\begin{aligned}
\sigma_{rr}(r, \theta) &= \frac{(\kappa + 3)(r^2 - R^2)R}{\pi(\kappa + 1)r^3} \sin(\Delta\theta/2) \sin(\theta) \\
&+ \sum_{n=1}^{Harm} \frac{R^n(n+2)(r^2 - R^2)}{\pi nr^{n+2}} \sin(n\Delta\theta/2) \sin(n\theta) \\
\sigma_{\theta\theta}(r, \theta) &= -\frac{R((\kappa - 1)r^2 + (\kappa + 3)R^2)}{\pi(\kappa + 1)r^3} \sin(\Delta\theta/2) \sin(\theta) \\
&- \sum_{n=1}^{Harm} \frac{R^n((n-2)r^2 - (n+2)R^2)}{\pi nr^{n+2}} \sin(n\Delta\theta/2) \sin(n\theta) \\
\sigma_{r\theta}(r, \theta) &= \frac{\Delta\theta}{2\pi} + \frac{R((\kappa - 1)r^2 + (\kappa + 3)R^2)}{\pi(\kappa + 1)r^3} \sin(\Delta\theta/2) \cos(\theta) \\
&+ \sum_{n=1}^{Harm} \frac{R^n(nR^2 + 2R^2 - nr^2)}{\pi r^{n+2}} \sin(n\Delta\theta/2) \cos(n\theta) \\
2\mu U_r(r, \theta) &= \frac{R((\kappa + 3)R^2 - 2(1 - 2\kappa \ln(r))r^2)}{2\pi(\kappa + 1)r^2} \sin\left(\frac{\Delta\theta}{2}\right) \sin(\theta) \\
&- \sum_{n=1}^{Harm} \frac{R^n((\kappa + n - 1)(n + 1)r^2 - (n^2 + n - 2)R^2)}{n(n^2 - 1)\pi r^{n+1}} \sin\left(\frac{n\Delta\theta}{2}\right) \sin(n\theta) \\
2\mu U_\theta(r, \theta) &= -\frac{r\Delta\theta}{2\pi} - \frac{R(2r^2 - (3 + \kappa)R^2 4\kappa r^2 \ln(r))}{2\pi(\kappa + 1)r^2} \sin\left(\frac{\Delta\theta}{2}\right) \cos(\theta) \\
&- \sum_{n=1}^{Harm} \frac{R^n((\kappa - n + 1)(n + 1)r^2 + (n^2 + n - 2)R^2)}{n(n^2 - 1)\pi r^{n+1}} \sin\left(\frac{n\Delta\theta}{2}\right) \cos(n\theta)
\end{aligned} \tag{D.11}$$

APPENDIX E

THE MICHELL SOLUTION- STRESS AND DISPLACEMENT COMPONENTS

κ is a Kolosov's constant, can be defined as following:

$$\kappa = \begin{cases} 3 - 4\nu & \text{for plane strain} \\ \frac{3 - \nu}{1 + \nu} & \text{for plane stress} \end{cases} \quad (\text{E.1})$$

Coef.	ϕ	σ_{rr}	$\sigma_{r\theta}$	$\sigma_{\theta\theta}$	$2\mu u_r$	$2\mu u_\theta$
A_{01}	r^2	2	0	2	$(\kappa - 1)r$	0
A_{02}	$r^2 \ln(r)$	$2 \ln(r) + 1$	0	$2 \ln(r) + 3$	$(\kappa - 1)r \ln(r) - r$	$(\kappa + 1)r\theta$
A_{03}	$\ln(r)$	$1/r^2$	0	$-1/r^2$	$-1/r$	0
A_{04}	θ	0	$1/r^2$	0	0	$-1/r$
A_{11}	$r^3 \cos \theta$	$2r \cos \theta$	$2r \sin \theta$	$6r \cos \theta$	$(\kappa - 2)r^2 \cos \theta$	$(\kappa + 2)r^2 \sin \theta$
A_{12}	$r \ln(r) \cos \theta$	$\cos \theta / r$	$\sin \theta / r$	$\cos \theta / r$	$\frac{1}{2} \left((\kappa + 1)\theta \sin \theta - \cos \theta + (\kappa - 1) \ln(r) \cos \theta \right)$	$\frac{1}{2} \left((\kappa + 1)\theta \cos \theta - \sin \theta - (\kappa - 1) \ln(r) \sin \theta \right)$
A_{13}	$r\theta \sin \theta$	$2 \cos \theta / r$	0	0	$\frac{1}{2} \left((\kappa - 1)\theta \sin \theta - \cos \theta + (\kappa + 1) \ln(r) \cos \theta \right)$	$\frac{1}{2} \left((\kappa - 1)\theta \cos \theta - \sin \theta - (\kappa + 1) \ln(r) \sin \theta \right)$
A_{14}	$\cos \theta / r$	$-2 \cos \theta / r^3$	$-2 \sin \theta / r^3$	$2 \cos \theta / r^3$	$\cos \theta / r^2$	$\sin \theta / r^2$
B_{11}	$r^3 \sin \theta$	$2r \sin \theta$	$-2r \cos \theta$	$6r \sin \theta$	$(\kappa - 2)r^2 \sin \theta$	$-(\kappa + 2)r^2 \cos \theta$
B_{12}	$r \ln(r) \sin \theta$	$\sin \theta / r$	$-\cos \theta / r$	$\sin \theta / r$	$\frac{1}{2} \left(-(\kappa + 1)\theta \cos \theta - \sin \theta + (\kappa - 1) \ln(r) \sin \theta \right)$	$\frac{1}{2} \left((\kappa + 1)\theta \sin \theta + \cos \theta + (\kappa - 1) \ln(r) \cos \theta \right)$
B_{13}	$r\theta \cos \theta$	$-2 \sin \theta / r$	0	0	$\frac{1}{2} \left((\kappa - 1)\theta \cos \theta + \sin \theta - (\kappa + 1) \ln(r) \sin \theta \right)$	$\frac{1}{2} \left(-(\kappa - 1)\theta \sin \theta - \cos \theta - (\kappa + 1) \ln(r) \cos \theta \right)$
B_{14}	$\sin \theta / r$	$-2 \sin \theta / r^3$	$2 \cos \theta / r^3$	$2 \sin \theta / r^3$	$\sin \theta / r^2$	$-\cos \theta / r^2$

Table E.1: The terms of Michell Solution (Airy Stress Function) and their corresponding stresses and displacements. Terms shown in the cyan are the self-equilibrating part of the solid disk stress function, terms shown in white are the self-equilibrating part of the Hole in a elastic plane, and terms shown in gray are modified secular terms removing their multi-value through linear combinations.

	ϕ	σ_{rr}	$\sigma_{r\theta}$	$\sigma_{\theta\theta}$	$2\mu u_r$	$2\mu u_\theta$
A_{n1}	$r^{n+2} \cos n\theta$	$-(n+1)(n-2)$ $\times r^n \cos n\theta$	$n(n+1)$ $\times r^n \sin n\theta$	$(n+1)(n+2)$ $\times r^n \cos n\theta$	$(\kappa - n - 1)$ $\times r^{n+1} \cos n\theta$	$(\kappa + n + 1)$ $\times r^{n+1} \sin n\theta$
A_{n2}	$r^{-n+2} \cos n\theta$	$-(n+2)(n-1)$ $\times r^{-n} \cos n\theta$	$-n(n-1)$ $\times r^{-n} \sin n\theta$	$(n-1)(n-2)$ $\times r^{-n} \cos n\theta$	$(\kappa + n - 1)$ $\times r^{-n+1} \cos n\theta$	$-(\kappa - n + 1)$ $\times r^{-n+1} \sin n\theta$
A_{n3}	$r^n \cos n\theta$	$-n(n-1)$ $\times r^{n-2} \cos n\theta$	$n(n-1)$ $\times r^{n-2} \sin n\theta$	$n(n-1)$ $\times r^{n-2} \cos n\theta$	$-nr^{n-1} \cos n\theta$	$nr^{n-1} \sin n\theta$
A_{n4}	$r^{-n} \cos n\theta$	$-n(n+1)$ $\times r^{-n-2} \cos n\theta$	$-n(n+1)$ $\times r^{-n-2} \sin n\theta$	$n(n+1)$ $\times r^{-n-2} \cos n\theta$	$nr^{-n-1} \cos n\theta$	$nr^{-n-1} \sin n\theta$
B_{n1}	$r^{n+2} \sin n\theta$	$-(n+1)(n-2)$ $\times r^n \sin n\theta$	$-n(n+1)$ $\times r^n \cos n\theta$	$(n+1)(n+2)$ $\times r^n \sin n\theta$	$(\kappa - n - 1)$ $\times r^{n+1} \sin n\theta$	$-(\kappa + n + 1)$ $\times r^{n+1} \cos n\theta$
B_{n2}	$r^{-n+2} \sin n\theta$	$-(n+2)(n-1)$ $\times r^{-n} \sin n\theta$	$n(n-1)$ $\times r^{-n} \cos n\theta$	$(n-1)(n-2)$ $\times r^{-n} \sin n\theta$	$(\kappa + n - 1)$ $\times r^{-n+1} \sin n\theta$	$(\kappa - n + 1)$ $\times r^{-n+1} \cos n\theta$
B_{n3}	$r^n \sin n\theta$	$-n(n-1)$ $\times r^{n-2} \sin n\theta$	$-n(n-1)$ $\times r^{n-2} \cos n\theta$	$n(n-1)$ $\times r^{n-2} \sin n\theta$	$-nr^{n-1} \sin n\theta$	$-nr^{n-1} \cos n\theta$
B_{n4}	$r^{-n} \sin n\theta$	$-n(n+1)$ $\times r^{-n-2} \sin n\theta$	$n(n+1)$ $\times r^{-n-2} \cos n\theta$	$n(n+1)$ $\times r^{-n-2} \sin n\theta$	$nr^{-n-1} \sin n\theta$	$-nr^{-n-1} \cos n\theta$

Table E.2: The terms of Michell Solution (Airy Stress Function) and their corresponding stresses and displacements. Terms shown in the cyan are the self-equilibrating part of the solid disk stress function and terms shown in white are the self-equilibrating part of the Hole in a elastic plane.

BIBLIOGRAPHY

BIBLIOGRAPHY

- [1] Young Ju Ahn and J. R. Barber. Response of frictional receding contact problems to cyclic loading. *International Journal of Mechanical Sciences*, 50(10-11):1519–1525, 2008.
- [2] Matthew S Allen, Brandon J Deaner, and Daniel J Segalman. Modal iwan models for structures with bolted joints. In *The Mechanics of Jointed Structures*, pages 255–278. Springer, 2018.
- [3] Julian Allwood. Survey and performance assessment of solution methods for elastic rough contact problems. *Journal of Tribology*, 127(1):10, 2005.
- [4] Julian Allwood and Hasan Ciftci. An incremental solution method for rough contact problems. *Wear*, 258(11-12):1601–1615, 2005.
- [5] L. E. Andersson, J. R. Barber, and A. R S Ponter. Existence and uniqueness of attractors in frictional systems with uncoupled tangential displacements and normal tractions. *International Journal of Solids and Structures*, 51(21-22):3710–3714, 2014.
- [6] James R Barber. *Elasticity*. Springer, 3rd edition, 2009.
- [7] James R Barber, Anders Klarbring, and Michele Ciavarella. Shakedown in frictional contact problems for the continuum. *Comptes Rendus Mécanique*, 336(1-2):34–41, 2008.
- [8] JR Barber, M Davies, and DA Hills. Frictional elastic contact with periodic loading. *International Journal of Solids and Structures*, 48(13):2041–2047, 2011.
- [9] Gernot Beer, Ian Smith, and Christian Duenser. *The boundary element method with programming: for engineers and scientists*. Springer Science & Business Media, 2008.
- [10] RH Bentall and KL Johnson. Slip in the rolling contact of two dissimilar elastic rollers. *International Journal of Mechanical Sciences*, 9(6):389–404, 1967.
- [11] E J Berger. Friction modeling for dynamic system simulation. *Applied Mechanics Reviews*, 55(6):535–577, 2002.
- [12] Enrico Bertocchi. Selected topics on the plane elastic contact with friction elastic contact with friction. *Dissertation*, 2009.
- [13] N. G. Bourago and V. N. Kukudzhanov. A review of contact algorithms. *Izv. RAN*, 1(1):45–87, 2005.
- [14] Matthew RW Brake. Constitutive modeling of contact for elastic-plastic materials engaged in micro/macroslip. In *The Mechanics of Jointed Structures*, pages 279–329. Springer, 2018.
- [15] Adam R Brink and D Dane Quinn. Shear effects on energy dissipation from an elastic beam on a rigid foundation. *Journal of Applied Mechanics*, 83(1), 2016.

- [16] Gaurav Chauda and Daniel J Segalman. Some exploration of the path-dependence in the contact analysis. In *ASME 2020 International Design Engineering Technical Conferences and Computers and Information in Engineering Conference*. American Society of Mechanical Engineers Digital Collection, 2020.
- [17] Gaurav Chauda and Daniel J Segalman. A Strategy for fine mesh resolution in contact mechanics. In *ASME 2021 International Design Engineering Technical Conferences and Computers and Information in Engineering Conference*, pages —. American Society of Mechanical Engineers, 2021.
- [18] Gaurav Chauda and Daniel J Segalman. A first violation contact algorithm that correctly captures history dependence. *International Journal of Mechanical Sciences*, page 106375, 2021.
- [19] W. Wayne Chen and Q. Jane Wang. A numerical model for the point contact of dissimilar materials considering tangential tractions. *Mechanics of Materials*, 40(11):936–948, 2008.
- [20] H. Cho and J. R. Barber. Dynamic behavior and stability of simple frictional systems. *Mathematical and Computer Modelling*, 28(4-8):37–53, 1998.
- [21] Hanbum Cho and J. R. Barber. Stability of the three-dimensional Coulomb friction law. *Proceedings of the Royal Society A: Mathematical, Physical and Engineering Sciences*, 455(1983):839–861, 1998.
- [22] T. F. Conry and A. Seireg. A mathematical programming method for design of elastic bodies in contact. *Journal of Applied Mechanics*, 38(2):387, 1971.
- [23] Robert D. Cook, David S. Malkus, Michael E. Plesha, and Robert J. Witt. *Concepts and Applications of Finite Element Analysis*. John Wiley & Sons Pvt., 2001.
- [24] Philip R Dahl. Solid friction damping of mechanical vibrations. *AIAA Journal*, 14(12):1675–1682, 1976.
- [25] W.J. Duncan. Some devices for the solution of large sets of simultaneous linear equations. *The London, Edinburgh, and Dublin Philosophical Magazine and Journal of Science*, 35(249):660–670, 1944.
- [26] J. Dundurs. Edge-bonded dissimilar orthogonal elastic wedges under normal and shear loading. *Journal of Applied Mechanics*, 36(3):650–652, 09 1969.
- [27] RMN Fleury and D Nowell. Evaluating the influence of residual stresses and surface damage on fatigue life of nickel superalloys. *International Journal of Fatigue*, 105:27–33, 2017.
- [28] Rodolfo Miguel Nogueira Fleury. *Investigation of fretting fatigue in turbine fir tree blade to disc joints at high temperature*. PhD thesis, University of Oxford, 2015.
- [29] RC Flicek, DA Hills, JR Barber, and D Dini. Determination of the shakedown limit for large, discrete frictional systems. *European Journal of Mechanics-A/Solids*, 49:242–250, 2015.

- [30] Robert C Flicek, M R W Brake, and D A Hills. Predicting a contact's sensitivity to initial conditions using metrics of frictional coupling. *Tribology International*, 108:95–110, 2017.
- [31] L E Goodman. Contact stress analysis of normally loaded rough spheres. *Journal of Applied Mechanics*, 29(3):515–522, 1962.
- [32] LE Goodman. *A review of progress in analysis of interfacial slip damping*. 1959.
- [33] Hugh GD Goyder. Damping due to joints in built-up structures. In *The Mechanics of Jointed Structures*, pages 135–147. Springer, 2018.
- [34] Joachim Gwinner and Ernst Peter Stephan. *Advanced boundary element methods*. Springer International Publishing AG,.
- [35] DA Hills, D Nowell, and A Sackfield. *Mechanics of elastic contacts*. Butterworth, 1993.
- [36] Thomas J.R. Hughes. *The finite element method: linear static and dynamic finite element analysis*. Courier Corporation, 2012.
- [37] Adnan Ibrahimbegovic and Edward L Wilson. Unified computational model for static and dynamic frictional contact analysis. *International journal for numerical methods in engineering*, 34(1):233–247, 1992.
- [38] Kenneth Langstreth Johnson. *Contact mechanics*. Cambridge University Press, 1987.
- [39] Y. Ju and T. N. Farris. Spectral analysis of two-dimensional contact problems. *Journal of Tribology*, 118(2):320–328, 1996.
- [40] J. J. Kalker. A minimum principle for the law of dry friction part 2 : application to nonsteadily rolling elastic cylinders. *Journal of Applied Mechanics*, pages 881–887, 1971.
- [41] J. J. Kalker. A minimum principle for the law of dry friction with application to elastic cylinders in rolling contact part 1 : fundamentals application to steady rolling. *Journal of Applied Mechanics*, pages 875–880, 1971.
- [42] J. J. Kalker. Contact mechanical algorithms. *Communication in Applied Numerical Methods*, 32:25–32, 1988.
- [43] J. J. Kalker and Y. Van Randen. A minimum principle for frictionless elastic contact with application to non-Hertzian half-space contact problems. *Journal of Engineering Mathematics*, 6(2):193–206, 1972.
- [44] Noboru Kikuchi and John Tinsley Oden. *Contact problems in elasticity: a study of variational inequalities and finite element methods*. SIAM, 1988.
- [45] A Klarbring. Examples of non-uniqueness and non-existence of solutions to quasistatic contact problems with friction. *Ingenieur-Archiv*, 60, 1990.
- [46] A Klarbring, A Mikelić, and M Shillor. Frictional contact problems with normal compliance. *International Journal of Engineering Science*, 26(8):811–832, 1988.

- [47] Anders Klarbring and Gunnar Björkman. A mathematical programming approach to contact problems with friction and varying contact surface. *Computers and Structures*, 30(5):1185–1198, 1988.
- [48] Tara Laforce. Boundary element method course notes. 2006.
- [49] J Li and EJ Berger. A semi-analytical approach to three-dimensional normal contact problems with friction. *Computational Mechanics*, 30(4):310–322, 2003.
- [50] S. Liu, Q. Wang, and G. Liu. A versatile method of discrete convolution and FFT (DC-FFT) for contact analyses. *Wear*, 243(1-2):101–111, 2000.
- [51] TW McDevitt and TA Laursen. A mortar-finite element formulation for frictional contact problems. *International Journal for Numerical Methods in Engineering*, 48(10):1525–1547, 2000.
- [52] R D Mindlin. Compliance of elastic bodies in contact. *Journal of Applied Mechanics*, 16(3):259–268., 1949.
- [53] D. Nowell, D.A. Hills, and A. Sackfield. Contact of dissimilar elastic cylinders under normal and tangential loading. *Journal of the Mechanics and Physics of Solids*, 36(1):59–75, jan 1988.
- [54] I. A. Polonsky and L. M. Keer. A numerical method for solving rough contact problems based on the multi-level multi-summation and conjugate gradient techniques. *Wear*, 231(2):206–219, 1999.
- [55] Walter Rudin. *Real and complex analysis, 3rd Ed.* McGraw-Hill, Inc., USA, 1987.
- [56] A Sackfield, D A Hills, and D Nowell. *Mechanics of elastic contacts.* Elsevier, 2013.
- [57] A Sackfield and DA Hills. Some useful results in the classical hertz contact problem. *The Journal of Strain Analysis for Engineering Design*, 18(2):101–105, 1983.
- [58] A Sackfield and DA Hills. Some useful results in the tangentially loaded hertzian contact problem. *The Journal of Strain Analysis for Engineering Design*, 18(2):107–110, 1983.
- [59] Maryam Saeedvafa and J Dundurs. An example for load-path dependence in elasticity with friction. *Journal de mécanique théorique et appliquée*, 7(2):211–226, 1988.
- [60] RS Sayles. Basic principles of rough surface contact analysis using numerical methods. *Tribology International*, 29(8):639–650, 1996.
- [61] Daniel J. Segalman. A Four-parameter Iwan model for lap-type joints. *Journal of Applied Mechanics*, 72(5):752–760, 02 2005.
- [62] Robert William Soutas-Little. *Elasticity.* Courier Corporation, 2012.
- [63] D A Spence. An eigenvalue problem for elastic contact with finite friction. In *Mathematical Proceedings of the Cambridge Philosophical Society*, volume 73, pages 249–268. Cambridge University Press, 1973.

- [64] D. A. Spence. The hertz contact problem with finite friction. *Journal of Elasticity*, 5(3-4):297–319, 1975.
- [65] Sergiu Spinu and Amarandei Dumitru. Numerical simulation of slip-stick elastic contact. *Numerical Simulation-From Theory to Industry*, 2012.
- [66] H. M. Stanley and T. Kato. An FFT-based method for rough surface contact. *Journal of Tribology*, 119(3):481, 2008.
- [67] Michael J Starr and Daniel J Segalman. Assessment of Coulomb friction in modeling joint mechanics via a parameter study of dissipation. In *The Mechanics of Jointed Structures*, pages 223–230. Springer, 2018.
- [68] W Sun and NG Zamani. Adaptive mesh redistribution for the boundary element in elastostatics. *Computers & structures*, 36(6):1081–1088, 1990.
- [69] A. Thaitirarot, R. C. Flicek, D. A. Hills, and J. R. Barber. The use of static reduction in the finite element solution of two-dimensional frictional contact problems. *Proceedings of the Institution of Mechanical Engineers, Part C: Journal of Mechanical Engineering Science*, 228(9):1474–1487, 2014.
- [70] Sandeep Vijayakar. A combined surface integral and finite element solution for a three-dimensional contact problem. *International journal for numerical methods in engineering*, 31(3):525–545, 1991.
- [71] MN Webster and RS Sayles. A numerical model for the elastic frictionless contact of real rough surfaces. *Journal of Tribology*, 108(3):314–320, 1986.
- [72] John A Williams and Rob S Dwyer-Joyce. Contact between solid surfaces. *Modern Tribology Handbook*, 1:121–162, 2001.
- [73] Iman Zare and Matt Allen. Adapting a contact-mechanics algorithm to predict damping in bolted joints using quasi-static modal analysis. *International Journal of Mechanical Sciences*, page 105982, 2020.